UNIVERSITY OF SOUTHAMPTON
FACULTY OF PHYSICAL SCIENCES AND ENGINEERING
PHYSICS AND ASTRONOMY

High Mass X-ray Binaries in the Milky Way and Beyond: A Multiwavelength Temporal and Spectroscopic Study

by

Elizabeth Shirley Bartlett

Thesis for the degree of Doctor of Philosophy
June 14, 2013

UNIVERSITY OF SOUTHAMPTON

ABSTRACT

FACULTY OF PHYSICAL SCIENCES AND ENGINEERING

PHYSICS AND ASTRONOMY

Doctor of Philosophy

HIGH MASS X-RAY BINARIES IN THE MILKY WAY AND BEYOND: A MULTIWAVELENGTH TEMPORAL AND SPECTROSCOPIC STUDY

by Elizabeth Shirley Bartlett

High Mass X-ray Binaries (HMXBs) represent an important stage in the evolution of massive stars and are some of the brightest sources in the X-ray sky. In the first half of this thesis a detailed analysis of X-ray observations of two HMXBs, the Be/X-ray Binary (BeXRB) Swift J045106.8-694803 and the supergiant/X-ray Binary XTE J0421+560/CI Camelopardalis, is presented. Simulations of the X-ray spectrum of Swift J045106.8-694803 show that both the spectral and timing properties can be reproduced by a blackbody and power law pulsating $\sim \pi$ out of phase with each other. The pulse profile of the blackbody is used to determine the angle between the rotation and magnetic axes of the neutron star and the angle between the rotation axis and line of sight. The apparently broad iron line of XTE J0421+560 is decomposed into three intrinsically narrow lines, FeI-Kα, FeI-Kβ and FeXXIV-XXVKα. The light curve extracted in the energy range defined as the Fe-Kα line from the spectral fits shows marginal evidence for a lag when cross correlated with that of the continuum. The lag is interpreted as the light crossing time of the circumbinary torus and implies a radius of 10 AU. The second part of this thesis considers HMXBs as a population. I describe the search for XRBs in the Phoenix dwarf galaxy, a Local Group dwarf irregular galaxy which share many similarities with the Small Magellanic Cloud (SMC), which has an apparent over-abundance of HMXBs. Finally, I discuss why the BeXRB population in the SMC is ideal for population studies and outline the work done to search for evidence for two different neutron star formation channels in their physical parameters.

CONTENTS

LIST OF TABLES

LIST OF FIGURES

DECLARATION

I, Elizabeth Shirley Bartlett, declare that the thesis entitled *High Mass X-ray Binaries in the Milky Way and Beyond: A Multiwavelength Temporal and Spectroscopic Study* and the work presented in the thesis are both my own, and have been generated by me as a result of my own original research. I confirm that:

- this work was done wholly or mainly while in candidature for a research degree at this University;
- where any part of this thesis has previously been submitted for a degree or any other qualification at this University or any other institution, this has been clearly stated;
- where I have consulted the published work of others, this is always clearly attributed;
- where I have quoted from the work of others, the source is always given. With the exception of such quotations, this thesis is entirely my own work;
- I have acknowledged all main sources of help;
- where the thesis is based on work done by myself jointly with others, I have made clear exactly what was done by others and what I have contributed myself;
- parts of this work have been published as:
  - The Search for High Mass X-ray Binaries in the Phoenix Dwarf galaxy, 2012, MNRAS, 422, pp. 2302-2313
  - Swift J045106.8-694803: a highly magnetized neutron star in the Large Magellanic Cloud, 2013, MNRAS, 428, p. 3607-3617
  - Timing and Spectral Analysis of the Unusual X-ray Transient XTE J0421+560/CI Camelopardalis, 2013, MNRAS, 429, p. 1213-1220

Elizabeth Shirley Bartlett, June 14, 2013

ACKNOWLEDGEMENTS

Just under 10 weeks ago, I started the hellish task of writing this thesis. Yet sitting here at the end, it's the acknowledgements that seem to be the hardest thing I've had to write! Firstly, a massive thank you to my supervisor, Malcolm Coe. Not everyone could have put up with a student like me, you'd think after being my undergraduate tutor for 4 years he'd have learnt his lesson! Thank you for your encouragement, your patience (which was tested!) and the gentle reminders to get on with it when I was too bogged down to see the wood for the trees! Thank you for giving me a chance to explore every one of my wild speculations, even if a few lead to nowhere. Thanks for the opportunity to travel to far flung corners of the world courtesy of the Great British tax payer. Watching the sun rise over Machu Picchu and fireworks over Table Mountain were all the sweeter for it! Another thank you must go to Tony Bird for unlimited use of his coffee machine. This thesis would probably be several weeks overdue if it wasn't for that marvellous piece of machinery! An astronomy group PhD thesis would not be complete with out a thank you to Simon - the true backbone of the Physics department.

To my office mates past and present, Martin, Dan C, Dan P and Mark, the glory days may be over, but the memories will always remain.... or not! Thanks for all the distractions in the form of youtube videos (Martin), passive aggressive e-mails (Dan C and Dan P) and constant cups of tea (Mark)! I couldn't ask for a better bunch of people to share my personal space with! Thanks to Sadie, Tana, Grace (the benefactor of Chapter 5!) and Mari - if anyone ever needs proof that women in science exist it's you guys (or girls?)! Your constant encouragement via twitter and other social media has been a blessing I don't deserve. Tana - we wracked up 211 e-mails in these closing weeks, misery really does love company it seems! Grace, there are still not enough words to express my gratitude for the aid package you delivered me. Sadie and Mari, just following you on twitter has brought smiles to the darkest moments of these last few weeks. Never change!

A non-science, but still highly academic mention has to go to the wonderful Lucy Shipley. These past 6/7 years have had their fair share of ups and downs, but having you there for me has made anything and everything more bearable. I just hope the same is true vice versa. Our friendship has been the best thing that has come crawling out of one of the countries most notorious night clubs... Another special mention has to go out to Holly, Beka, Simmo, Darbs and Jonathan. Everyone always told me that university would be the best years of my life - well I must be very lucky because for me those days started with 6th form!

I am also indebted to my wonderful family, I really wouldn't be here if it weren't for you! Thanks for all the support - To Mum and Dad, for NEVER trying to make me be a "girly" girl: for sending me to karate, not ballet, and getting me Lego, not Barbies! Your aversion to "pink plastic" has helped make me who I am today. To

Alex and Charlotte, you're the best siblings I could ever ask for - you make me smile everyday and never fail to put things into perspective for me (in words that may not be repeatable here...). I can only hope I've set you both a good example at how to work and play! A mention has to go to my Aunt and Uncle, Angela and Jim for providing me with homecooked meals when they were sorely needed, unlimited use of their washing machine and most importantly access to their van! You've spent weekends moving myself and my nearest and dearest in and out of more houses in Southampton than you'd care to remember! I hope I've always let you know how much I appreciate it. To my Grandma, Poppa, Nan and Grandad, thank you for always being proud of me and worrying needlessly about my welfare. Am I eating enough? Sleeping enough? do I have enough money? am I happy? Thanks for always taking an interest (even if you didn't always understand the ins and outs) and the endless encouragement.

And finally - two massive thank yous to my boys: Seb and Lee. Seb, as I started this journey with you in 2005, it seems only fitting to finish it with you now. Writing up alongside you has made what could have been tragedy into more of a sitcom!

Lee - what can I say? There are no words to describe the depth of my gratitude or the height of my affections. You have put up with so much, for so little in return. Your unwaivering faith in me has got me through times when I didn't believe in myself. I love you, I love you, I love you and I am SO excited about our life together in Africa - and I promise it will be the first adventure of many!

Elizabeth Shirley Bartlett, June 14, 2013

> Time is an illusion. Lunchtime doubly so.
>
> THE HITCHHIKER'S GUIDE TO THE GALAXY (1979)

To Poppa,
who put me on this path.

In the beginning the Universe was created. This has made a lot of people very angry and has been widely regarded as a bad move.

THE RESTAURANT AT THE END OF THE UNIVERSE (1980)

DON'T PANIC

THE HITCHHIKER'S GUIDE TO THE GALAXY (1979)

Space is big. Really big. You just won't believe how vastly, hugely, mindbogglingly big it is. I mean, you may think it's a long way down the road to the chemist's, but that's just peanuts to space.

THE HITCHHIKER'S GUIDE TO THE GALAXY (1979)

1

Introduction

With over 70% of all massive stars being formed in binary systems, X-ray binaries (XRBs), particularly High Mass X-ray Binaries (HMXBs), represent an important step in the evolution of massive stars (Sana *et al.*, 2012). XRBs are defined as as a neutron star or black hole primary accreting matter from a secondary star (e.g. Lewin *et al.* 1997). Whilst the definition is often extended to include white dwarf accretors, this thesis adheres to the conventional definition of XRBs outlined above. XRBs are classified according to the mass of the companion star, High Mass X-ray Binaries (HMXBs) typically have donor stars with $M \gtrsim 10 M_{\odot}$ and spectral type OB whilst Low Mass X-ray Binaries (LMXBs) have donor stars with $M \lesssim 1 M_{\odot}$ and later than type A (Lewin *et al.*, 1997; Lewin and van der Klis, 2006). In rare cases the secondary in an LMXB can even be a white dwarf (Rappaport *et al.*, 1987). Despite this apparently simple categorisation, HMXBs and LMXBs have very different X-ray and optical properties and accrete via different mechanisms. This thesis is focused on the optical and X-ray behaviour of HMXBs with neutron star counterparts, as such LMXBs are not discussed in any great depth but to contrast their general properties against those of HMXBs.

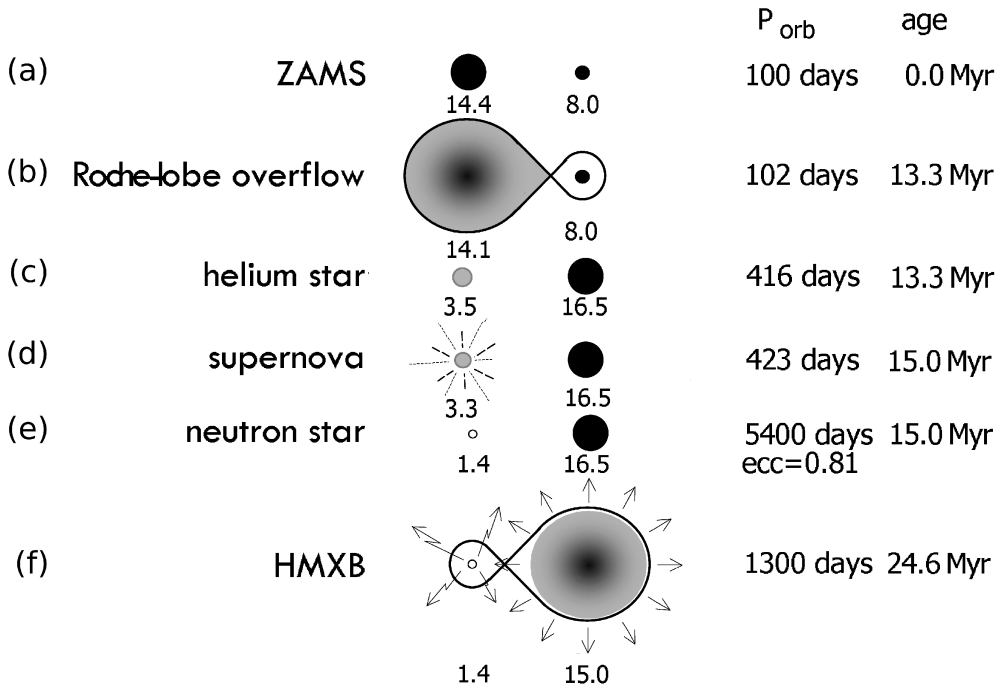

Figure 1.1: Schematic of binary evolution and HMXB formation. Editted from Lewin and van der Klis (2006)

1.1 X-ray Binary Formation

The type of XRB formed depends on the mass ratio of the primordial binary, q, as well as the masses of the individual stars. Figure 1.1 depicts the formation of an HMXB. Initially (**a** in Fig 1.1) the binary system consists of two massive ($\gtrsim 8M_{\odot}$) stars of roughly similar mass ($q \equiv M_1/M_2 \sim 1.8$, where M_1 is the mass of the initially more massive star throughout). More massive stars have to fuse hydrogen at a greater rate to remain in hydrostatic equilibrium and so both the luminosity, L, and lifetime, T, of a star are heavily dependent on its mass ($L \propto M^{3.5}$ and $T \propto M^{-2.5}$). As such the more massive star, S_1 evolves off the main sequence first. It expands as hydrogen fusion is ignited in layers around the helium core, filling its Roche-Lobe (step **b**).

The Roche-Lobe is the hypothetical "sphere" of gravitational influence around each of the binary components, and depends on the mass ratio and semi-major axis of the orbit. There are five points around the system (Lagrangian points) at which the effective potential is zero, three of which lie on the hypothetical line that runs through the two components and their centre of mass. The Roche-Lobes, equipotential contours and Lagrangian points for a binary with similar properties to that in Figure 1.1 are shown in Figure 1.2. The Roche-Lobes of the primary and sec-

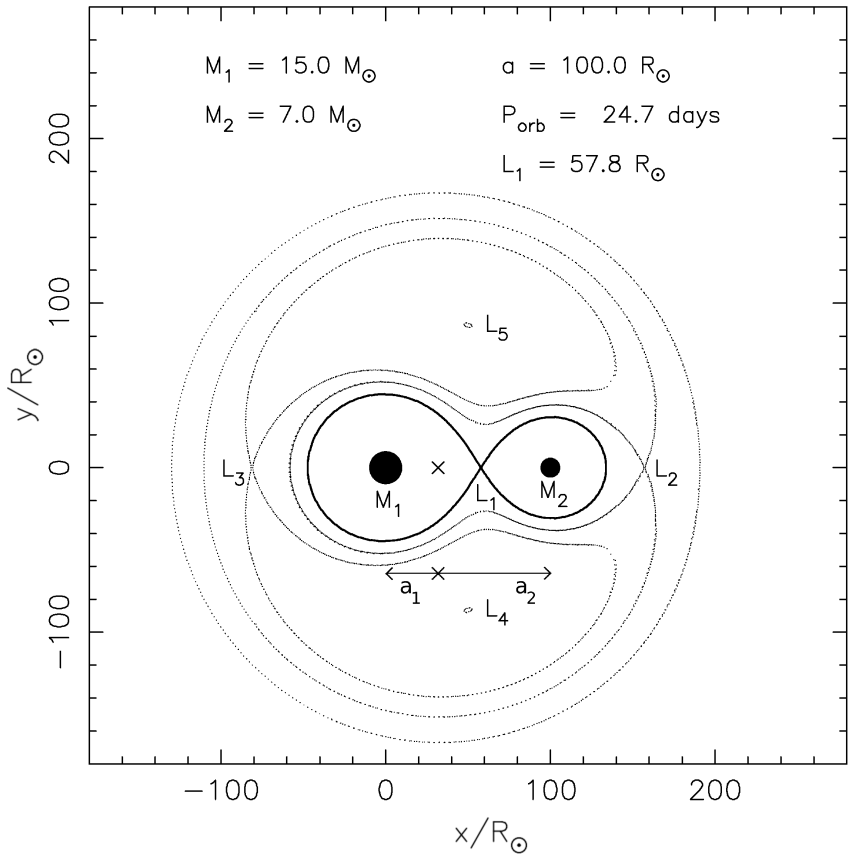

Figure 1.2: Cross-section in the equatorial plane of a HMXB progenitor. The five Lagrangian points are marked along with the Roche surfaces and equipotential contours. Editted from Lewin and van der Klis (2006)

ondary meet at the Lagrangian point between the two stars, L_1, and material from the companion star can flow through this point into the Roche-Lobe of the initially less massive star, S_2, and thus be accreted.

The transfer of material from one star to the other causes the semi-major axis, a, and hence the orbital period, P, to alter. The total angular momentum, J, of the system (ignoring the spin of the individual components) can be expressed as

$$J = I\Omega = (M_1 a_1^2 + M_2 a_2^2)\Omega \tag{1.1}$$

where I is the moment of inertia of the system and Ω is the angular velocity. From the definition of Centre of Mass, $M_1 a_1 = M_2 a_2$. Using this and Kepler's third law

$$\Omega^2 = \frac{GM}{a^3} \tag{1.2}$$

to substitute in for Ω and rearranging for a one obtains

$$a = \frac{MJ^2}{GM_1^2M_2^2} \tag{1.3}$$

where M is the total mass of the system and G is the gravitational constant. This can be logarithmically differentiated to get

$$\frac{\dot{a}}{a} = 2\frac{\dot{J}}{J} - 2\frac{\dot{M}_1}{M_1} - 2\frac{\dot{M}_2}{M_2} + \frac{\dot{M}}{M} \tag{1.4}$$

For conservative mass transfer, $\dot{M}$ and $\dot{J}$ are zero and $\dot{M}_2 = -\dot{M}_1$. This leads to

$$\frac{\dot{a}}{a} = 2\frac{\dot{M}_2}{M_2}\left(\frac{M_2}{M_1} - 1\right) \tag{1.5}$$

Equation 1.5 shows how the semi-major axis changes with the direction of mass transfer and the evolution of the mass ratio. If the accretor (M_2) is less massive than the donor star ($\dot{M}_2 > 0$, $M_2/M_1 < 1$) the semi major orbit decreases. If the accretor is more massive than the donor ($\dot{M}_2 > 0$, $M_2/M_1 > 1$) the semi-major orbit increases. This means that initially the orbit of the binary shrinks before expanding as the mass ratio inverts (step **c**) leaving only the helium core of S_1. Eventually the helium core goes supernova (step **d**) disrupting the binary system considerably. This leaves a compact object, in this case a neutron star, which can then accrete matter off the now more massive star (step **e**), either via Roche Love overflow or from the stellar wind.

The formation of an LMXB requires a much greater difference in mass between the two stars. As with the HMXBs, the massive star evolves off the main sequence first and expands. However almost immediately after mass transfer begins the donor star engulfs S_2 and the system undergoes common envelope evolution. The semi-major axis of the orbit is greatly reduced as frictional forces reduce the velocity of S_2, causing S_2 to spiral in towards the donor star. If enough energy is released as the orbit shrinks the envelope is expelled leaving the helium core of the donor star and S_2 in a tight orbit ($P_{orb} < 1$ day). The helium core then goes supernova, resulting in a compact object in a tight orbit around a star with mass comparable to that of the sun.

1.2 The Neutron Star

By definition, HMXBs are a strong source of X-ray radiation. These photons are emitted by the accreted material at or close to the neutron star surface. The luminosity of the system, L, is synonymous with the mass accretion rate $\dot{M}$.

$$L = \frac{dE}{dt} = \frac{GM_{NS}\dot{M}}{R_{NS}} \tag{1.6}$$

where M_{NS} and R_{NS} are the mass and radius of the neutron star respectively. The Eddington luminosity, L_{Edd}, is the luminosity at which the radiation pressure on the infalling material is equal to the gravitational pull of the star. The radiative flux of the neutron star at a distance, r is:

$$\frac{dE}{dtdA} = \frac{L}{4\pi r^2} \tag{1.7}$$

For photons, $E = pc$ where p is the momentum of the photon. The force exerted on a electron is:

$$\frac{dp}{dt} = \frac{\sigma_T}{c}\frac{dE}{dtdA} \tag{1.8}$$

$$= \frac{L\sigma_T}{4\pi cr^2} \tag{1.9}$$

where σ_T is the Thomson cross section for the electron. Equating this with the gravitational force gives:

$$\frac{GM_{NS}m_p}{r^2} = \frac{L_{Edd}\sigma_T}{4\pi cr^2} \tag{1.10}$$

$$L_{Edd} = \frac{4\pi cGm_p}{\sigma_T}M_{NS} \tag{1.11}$$

$$\simeq 1.2\times 10^{38}\frac{M_{NS}}{M_\odot}\ \text{erg s}^{-1} \tag{1.12}$$

where m_p is the mass of a proton. A typical neutron star mass, $M_{NS} = 1.4M_\odot$, leads to an $L_{Edd} \sim 2\times 10^{38}$ erg s^{-1}. In theory, stable accretion cannot exceed this luminosity, as the radiation pressure will blow away the infalling material, cutting off the source of the X-rays.

The neutron stars in HMXBs have some of the strongest magnetic fields seen in the observable universe, with magnetic fields $B \geq 10^{10}$ G (Cheng and Dai, 1997).

This magnetic field interacts with the infalling material at the Alfvén radius, r_A. This is the radius at which the ram pressure of the infalling material is equalled by the magnetic pressure outwards.

$$\frac{B^2}{8\pi} = \rho v^2 \tag{1.13}$$

$$\frac{1}{8\pi}\left(\frac{\mu}{r_A^3}\right)^2 = \rho v^2 \tag{1.14}$$

B is the magnetic field, ρ and v are the density and velocity of the infalling material respectively and μ is the magnetic moment. The material is assumed to be free falling radially and so $v = v_{ff} = \sqrt{2GM_{NS}/r}$

$$\frac{\mu^2}{8\pi r_A^6} = \frac{2\rho G M_{NS}}{r_A} \tag{1.15}$$

which can be rearranged to give:

$$r_A = \left(\frac{\mu^2}{16\pi\rho G M_{NS}}\right)^{\frac{1}{5}} \tag{1.16}$$

Substituting in for $\rho = \dot{M}/(4\pi v_{ff} r^2)$ and v_{ff} leads to:

$$r_A = \left(\frac{\mu^4}{8GM_{NS}\dot{M}^2}\right)^{\frac{1}{7}} \tag{1.17}$$

At $r \leq r_A$ material follows the field lines, is funnelled into an accretion column and onto the magnetic poles (Basko and Sunyaev, 1976). This leads to X-rays being emitted from very localised areas on or close to the neutron star surface. If the magnetic and spin axes of the neutron star are misaligned then a "lighthouse effect" is observed: the X-rays are modulated as the neutron star rotates. These neutron stars are called "pulsars". To observe a pulsar the X-ray beam must sweep across our line of sight, as such there will be several highly magnetised, accretion powered neutron stars that are not observed as pulsars due to orientation effects.

Figure 1.3 shows the two possible accretion geometries for X-ray pulsars, the "fan" beam and the "pencil" beam. The geometry observed depends on the mass accretion rate (and so luminosity). For small to moderate $\dot{M}$, most of the photons emerging from the accretion mound are emitted parallel to the magnetic field, as the photon scattering cross-section is reduced along the magnetic field lines. This

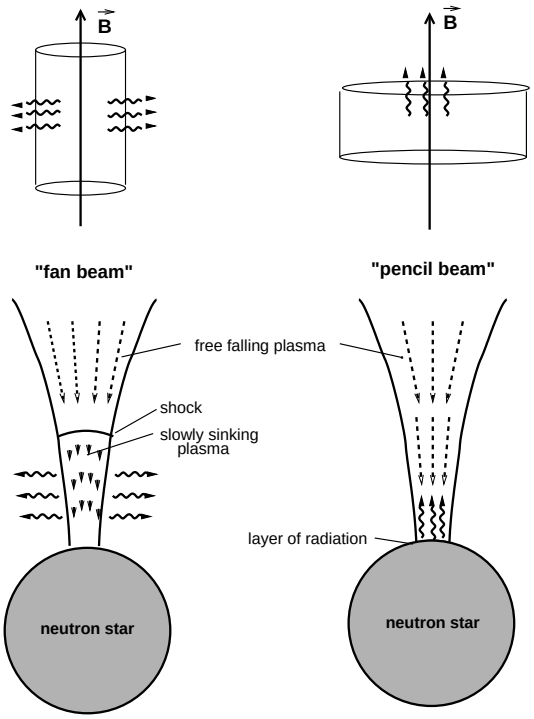

Figure 1.3: Accretion Geometries proposed by Basko and Sunyaev (1975, 1976). Fan beam (left) and pencil beam (right). Figure taken from Schönherr *et al.* (2007)

results in a pencil beam (Basko and Sunyaev, 1975). For larger values of $\dot{M}$ the infalling material forms a radiative shock. The accretion flow is decelerated and the material sinks towards the neutron star surface. The optical depth of the accretion column is much greater than 1 and so photons cannot escape vertically, parallel to the magnetic field. Instead the sinking gas emits these photons sideways, perpendicular to the magnetic field, forming a fan beam (Basko and Sunyaev, 1976). The pulse profiles of these two geometries are expected to have different shapes, a simple sinusoid for a pencil beam and a more complex double peak structure for a fan beam. The observational properties of the two different geometries are discussed in Section 1.4.3

Another crucial radius for neutron stars in HMXBs is the corotation radius. This is the radius at which the angular velocity of the Keplerian disc, $\Omega_K(r)$, equals that of the neutron star, Ω_{NS}. This depends only on the spin period of neutron star, P_{spin}. From Kepler's third law we have:

$$\Omega_{NS}^2 = \left(\frac{2\pi}{P_{spin}}\right)^2 = \frac{GM_{NS}}{r_{co}^3} \tag{1.18}$$

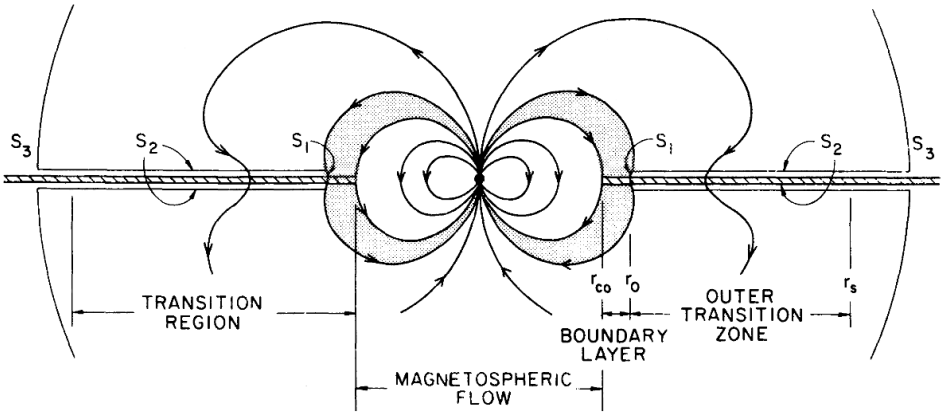

Figure 1.4: Diagram of the accretion flows onto the neutron star (from Ghosh and Lamb 1979). The boundary layer spans from r_0 to r_{co}

which can be rearranged to give:

$$r_{co} = \left(\frac{GM_{NS}}{4\pi^2} P_{spin}^2 \right)^{1/3} \tag{1.19}$$

The ratio of Ω_{NS} to the angular velocity of the disc at the Alfvén radius, $\Omega_K(r_A)$, is the fastness parameter, ω (Illarionov and Sunyaev, 1975). The value of ω has important implications for the spin period of the neutron star. If $\omega < 1$ (i.e. $r_A < r_{co}$) then the Keplerian disc is rotating faster than the magnetosphere of the neutron star at r_A. The material then effectively drags the magnetosphere (and hence the neutron star) round, transferring angular momentum from the disc onto the star, reducing P_{spin}. If $\omega > 1$ ($r_A > r_{co}$) then the Keplerian disc is rotating at a slower rate than the magnetosphere of the neutron star at r_A and angular momentum is transferred from the neutron star to the disc. This causes the spin period to increase.

In practise, the change in $\Omega_K(r)$ to Ω_{NS} does not occur at r_A but over a short distance, called the boundary layer (see Fig. 1.4). In this layer both of the situations described above can occur simultaneously and it is the net effect of these torques that determines whether the pulsar is spun up or down. The accretion torque depends on $M_\odot$ and B, and so for a given magnetic field and mass accretion rate, there will be a spin period for which the net torque on the star is zero. This is the equilibrium period of the pulsar and the neutron star evolves towards this value through out its lifetime. Substituting $\mu = BR_{NS}^3$ and Equation 1.6 into Equation 1.17 and

equating with Equation 1.19 leads to

$$P_{eq} = C\left(\frac{R_{NS}^{15}B^6}{M^2L^3}\right)^{\frac{1}{7}} \tag{1.20}$$

where C is a constant. This leads to

$$P_{eq} \sim 2\left(\frac{R_6^{15}B_{12}^6}{M_1^2L_{37}^3}\right)^{\frac{1}{7}} \tag{1.21}$$

where R_6 is the neutron star radius expressed in units of 10^6 cm, B_{12} is the magnetic field in units 10^{12} G, L_{37} is the X-ray luminosity in units of 10^{37} erg s^{-1} and M_1 is the mass of the neutron star in solar masses. The equilibrium period is discussed in Section 1.5.5

If $r_A >> r_{co}$ then material is unable to follow the field lines. The centrifugal force inhibits the accretion onto the neutron star and material is ejected from the system. This is known as the propeller effect. The value of ω at which the system enters the propeller regime is not known, however the linear velocity, v_K of the Keplerian disc at r_A, should exceed the escape velocity, v_{esc}. Again, Kepler's third law gives:

$$\Omega_K^2 = \left(\frac{v_K}{r_A}\right)^2 = \frac{GM}{r_A^3} \tag{1.22}$$

$$v_K^2 = \frac{GM}{r_A} \tag{1.23}$$

The right hand side of Equation 1.23 is recognisable as half v_{esc}^2, obtained by equating the kinetic energy and gravitational potential energy of a particle. This leads to $v_{esc} = \sqrt{2}v_K$ and $\omega > \sqrt{2}$.

Neutron stars with magnetic fields greater than the quantum critical value B_{crit} are termed "magnetars". As B tends towards B_{crit}, the cyclotron energy of the plasma electrons approaches their rest mass energy. Equating the Lorentz force with the centripetal force

$$evB_{crit} = \frac{m_e v^2}{r} \tag{1.24}$$

$$\omega_{cyc} = \frac{v}{r} = \frac{eB_{crit}}{m_e} \tag{1.25}$$

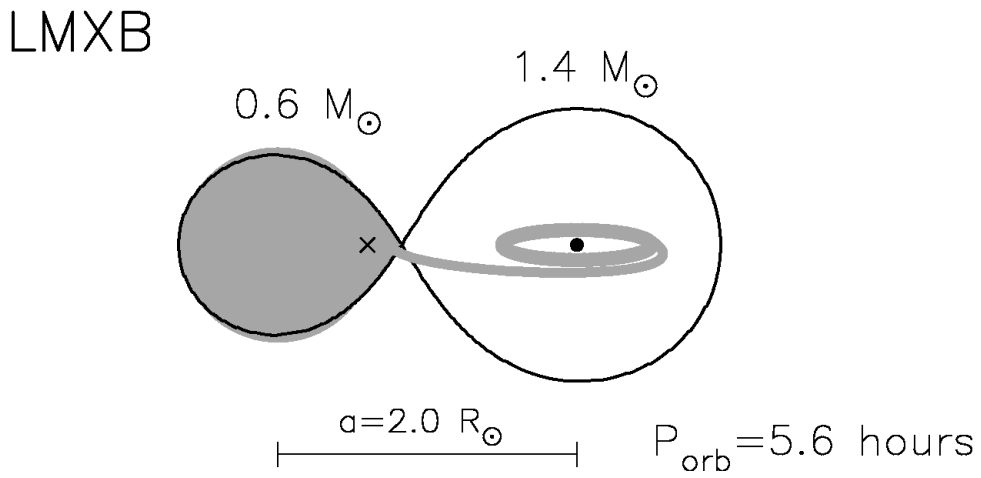

Figure 1.5: Schematic of an LMXB taken from Lewin and van der Klis (2006).

where ω_{cyc} is the cyclotron frequency, e is the charge on the electron and m_e is the rest mass of the electron in kg. Multiplying this by $\hbar$ and equating with the rest mass energy of the electron gives

$$\frac{\hbar e B_{crit}}{m_e} = m_e c^2 \tag{1.26}$$

$$B_{crit} = \frac{m_e^2 c^2}{e\hbar} = 4.4 \times 10^{13}\text{G} \tag{1.27}$$

where equations 1.26 and 1.27 are in SI units. Expressed in the centimetre-gram-second unit system more commonly used by theoretical physicists, the formula becomes the more familiar $B_{crit} = (m_e^2 c^3)/(e\hbar)$. At values of $B > B_{crit}$ classical physics can no longer be used to describe the motion of the electrons.

1.3 LMXBs

Figure 1.6 shows a schematic of an LMXB. LMXBs are classified according to their compact object and the fraction the X-ray luminosity is of the Eddington luminosity, amongst other things. The X-ray luminosities of LMXBs can range from $10^{30.5}$ – 10^{39} ergs s^{-1} depending on the compact object and the source "state", determined via spectral and timing analysis.

The small semi-major axes of LMXBs means that the Roche radius (The radius of the Roche-Lobe) is always less than the stellar radius and hence the companion star always fills its Roche-Lobe. As detailed in Section 1.1, the material flows from the companion star via L_1, transferring angular momentum from the secondary to the primary. The specific angular momentum of the infalling material (i.e. the

angular momentum per unit mass), h, can be expressed as

$$h = \frac{J}{m} = R_{circ}^2 \Omega \tag{1.28}$$

where R_{circ} is the radius at which the material would orbit if it retained angular momentum but not energy (Lewin and van der Klis, 2006). Kepler's third law gives

$$\Omega^2 = \frac{GM_{acc}}{R_{circ}^3} \tag{1.29}$$

where M_{acc} is the mass of the accretor. Substituting Equation 1.29 into 1.28 and rearranging for R_{circ} gives

$$R_{circ} = \frac{h^2}{GM_{acc}} \tag{1.30}$$

If R_{circ} is greater than the effective radius of the compact object (i.e. the radius of the magnetosphere if the object has a significant magnetic field, or the physical radius of the object if not) then the material cannot be transferred directly onto the compact object, instead it forms a ring orbits the accretor at radius R_{circ}. The material in this ring slowly spirals both into and away from the compact object as its energy is dissipated and its angular momentum transferred outward. The ring of material is then transformed into a disc, known as an accretion disc. These are present in all LMXBs.

The energy in the accretion disc is lost in the form of heat causing the accretion disc to emit electromagnetic radiation. It is the accretion disc that dominates the spectral energy distribution of LMXBs with direct emission in the X-rays and re-processed X-ray emission at optical wavelengths. It is rarely possible to see optical emission from the companion star itself, instead what is seen is a hot continuum, with Doppler broadened H and He emission lines from the inner accretion disc.

Unlike HMXBs, LMXBs rarely harbour an X-ray pulsar. This is because the magnetic fields of the neutron stars in LMXBs are $10^{-1} - 10^{-4}$ times lower than those in HMXBs, and so the accreted material is not funneled onto the polar caps. Instead the material builds up as a layer on the neutron star surface. When the material at the bottom of the layer reaches a critical density and temperature nuclear fusion takes place, raising the temperature and leading to runaway thermonuclear burning on the surface of the neutron star. These are observed as X-ray bursts and are characterised by a rapid increase in flux (on second timescales) followed by an approximately exponential decay. A handful of LMXBs have been discovered with pulsations during these thermonuclear burst, all with millisecond spin periods.

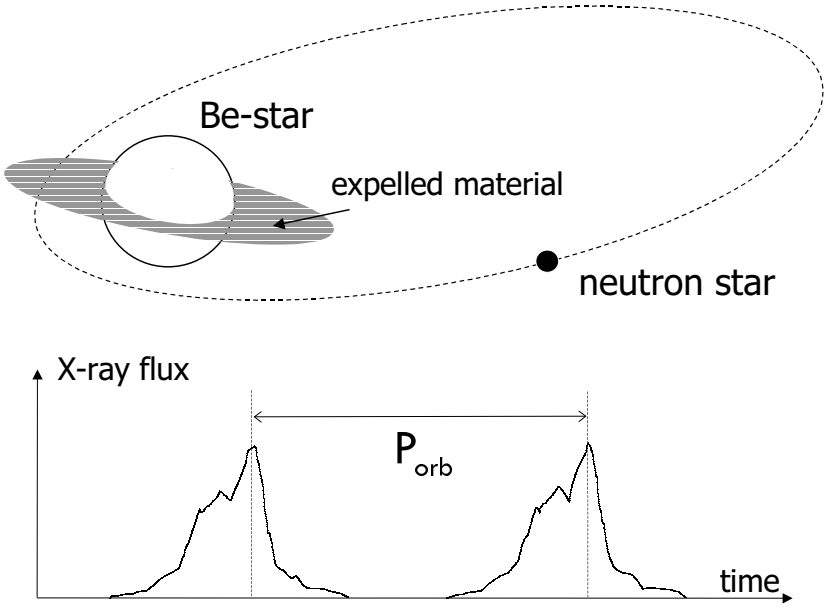

Figure 1.6: Schematic of a BeXRB taken from Lewin and van der Klis (2006).

These are thought to be "recycled" pulsars, i.e. slow rotating pulsars which have been spun up due to long periods of high mass accretion. For a full discussion on the X-ray and optical properties of LMXBs and accretion disc formation see Lewin and van der Klis (2006) and Frank *et al.* (2002).

1.4 HMXBs

1.4.1 BeXRBs: Overview

Figure 1.6 shows a schematic of a BeXRB. BeXRBs were first recognised as separate class of HMXB by Maraschi *et al.* (1976) and are now the most numerous subclass of HMXB (Liu *et al.*, 2006). The compact objects in these systems are exclusively neutron stars in an eccentric orbit around a main sequence Be star. There appears to be an emerging class of Be binary with white dwarf counterparts (e.g. Kahabka *et al.* 2006; Sturm *et al.* 2012a; Li *et al.* 2012) suggesting that the HMXB criteria could be, and indeed regularly is, extended to include white dwarfs. Thus far, not a single BeXRB binary has been found to host a black hole. Belczynski and Ziolkowski (2009) use binary population synthesis models to show that the expected ratio of BeXRBs with neutron stars to black holes in the Galaxy is relatively high ($\sim 30-50$), and so broadly in line with observations. Interestingly, the popu-

lation synthesis of Be/white dwarf binaries by Raguzova (2001) predicts that these sources should outnumber the "classic" BeXRBs ∼7:1. They note a large number of selection effects which could drastically restrict the number of sources observed.

Be stars are rotating rapidly at close to the the critical breakup velocity (Townsend *et al.*, 2004), causing an enhancement in the equatorial material which replenishes a circumstellar disc around the star (Lamers and Waters, 1987). Whether the rotation of the star is sufficient to create this disc is a subject of much debate and is an area of active research (Porter and Rivinius, 2003). The presence of a disc leads to hydrogen emission lines in the spectrum (and hence the 'e' designation, Collins II 1987). This is a transient phenomenon and thus any B star that has exhibited hydrogen emission lines in its spectrum at some time is classed as a Be star. The transient nature of these discs could be linked to the hypothesised secondary production mechanism (Porter and Rivinius, 2003).

There are two types of X-ray outburst associated with the X-ray emission of BeXRBs: Type I outbursts have L_X in the range $10^{36} - 10^{37}$ ergs s^{-1} and occur periodically around the time of the periastron passage of the neutron star (see Fig 1.6). Type II outbursts reach higher luminosities, $L_X \geq 10^{37}$ ergs s^{-1}, last much longer and show no correlation with orbital phase (Stella *et al.*, 1986). These are thought to be caused by an enhancement of the circumstellar disc allowing accretion to occur at any phase of the orbit at a much higher rate. Laycock *et al.* (2010) detected quiescent luminosity in some of these systems down to $L_X = 10^{33} - 10^{34}$ ergs s^{-1}.

Temporary accretion discs are thought to be formed at or around the periastron passage of the neutron star, facilitating mass transfer (Okazaki and Negueruela, 2001). Figure 1.7 shows the two scenarios for the disc formation. In scenario A. the disc of the Be star exceeds its Roche-Lobe as the neutron approaches periastron ($\frac{da}{dt} < 0$). Material is then lost from the disc and is accreted by the neutron star, via an accretion disc. As the separation of the bodies increases ($\frac{da}{dt} > 0$), the Be star no longer exceeds its Roche-Lobe, the overflow halts and the accretion disc disappears. The other scenario requires a precessing density wave in the Be star's circumstellar disc. If the neutron star and disc precession period are in phase, overflow occurs and an accretion disc is formed. Once again, as the separation increases and the Roche-Lobe is no longer exceeded, the disc fades. This repeats for each orbit until the precession and orbital periods are no longer in phase. The observational properties of density waves are discussed in Section 1.4.4.

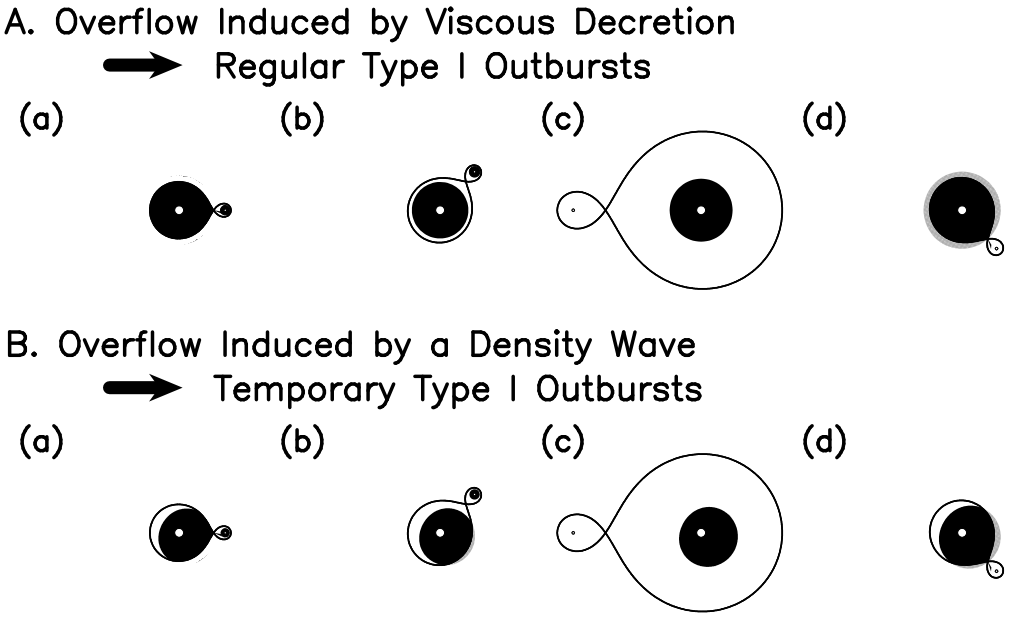

Figure 1.7: Two possible scenarios for disc formation in BeXRBs, taken from Okazaki and Negueruela (2001)

1.4.2 sgXRBs: Overview

The orbits of sgXRBs tend to have shorter periods than those of BeXRBs (tens of days vs. hundreds of days, see section 1.5.5) and lower eccentricities. This is no coincidence as tidal interactions circularise the orbits of close binaries on astronomically short timescales (North and Zahn, 2003). Consequently, the compact objects in sgXRBs are constantly embedded in the dense, approximate uniform stellar wind of the companion star. Accretion occurs via the Bondi–Hoyle–Lyttleton mechanism (Bondi and Hoyle 1944; Bondi 1952 for a recent review see Edgar 2004), the mass transfer of which can be approximated by:

$$\dot{M} = \frac{4\pi\rho G^2 M_{NS}^2}{v_{rel}^3} \tag{1.31}$$

where G is the gravitational constant, M_{NS} is the mass of the neutron star, v_{rel} is the velocity of the neutron star relative to the circumstellar material and ρ is the density of the material.

The winds of these massive stars are driven by the radiation pressure on the atoms in the stellar atmosphere by photons with energies equal to absorption line transitions (so called “Line driven” winds, Lucy and Solomon 1970). In addition to the strong stellar winds, a number of these stars have atmospheres which extend out passed their Roche-Lobe, allowing a substantial amount of material to be transferred

via “atmospheric Roche-Lobe overflow”. The environments of sgXRBs make them persistent sources of X-rays with luminosities, L_X, 10^{36}–10^{38} ergs s^{-1}.

1.4.2.1 sgB[e]-XRBs

Supergiant B[e]-XRBs (sgB[e]-XRBs) are a subset of sgXRBs with sgB[e] counterparts. These are post main sequence stars characterised by a two component stellar wind - a hot, fast polar wind and a slow, cool equatorial wind. The equatorial winds of these stars are cool and dense enough for dust to form which, in turn, leads to the formation of a torus around the star (Zickgraf *et al.*, 1985, 1986; Zickgraf, 2006). A more in depth discussion of the optical properties of these sources is included in Section 1.4.4 and Chapter 3. These are rare systems with only two known to date: CI Camelopardalis/XTE J0421+560 (CI Cam) and IGR J16318-4848 (see Courvoisier *et al.* 2003, Smith *et al.* 1998, Chapter 3).

The X-ray spectra of CI Cam and IGR J16318-4848 have extremely high levels of absorption (10^{23-24} cm^{-2}). This is consistent with the current model for CI Cam: that of a compact object (probably a neutron star) orbitting close to the stellar surface, well within the dusty torus. Both systems appear to have similar quiescent X-ray luminosities (to within a factor of 3), $\sim 10^{33}$ erg s^{-1}. However, the distances to both CI Cam and IGR J16318-4848 are uncertain and so this is not secure. Furthermore, both sources have displayed aperiodic “flaring” behaviour, albeit with very different peak luminosities. Two flares have been associated with IGR J16318-4848, separated by ~ 9 yrs (1994 and 2003; Courvoisier *et al.* 2003; Murakami *et al.* 2003) and with peak luminosities $\sim 10^{36}$erg s^{-1} (Filliatre and Chaty, 2004). CI Cam had one giant outburst in 1998 which reached a peak luminosity of $\sim 3 \times 10^{38}$erg s^{-1} (e.g. Hynes *et al.* 2002). These systems are discussed in detail in Chapter 3. A summary of their optical properties is included in Section 1.4.4.

1.4.3 X-ray Properties

The X-ray spectra of NS-HMXBs are characterised by intrinsically absorbed power laws with photon indices, Γ, in the range 0.6-1.4 (Haberl *et al.*, 2008a), accompanied by high energy cut-offs (Lutovinov *et al.*, 2005). A soft excess has been reported in some of these sources with blackbody temperatures $kT_{BB}<0.5$ keV (e.g. Sturm *et al.* 2012b) and are attributed to the inner edge of an accretion disc surrounding the neutron star. Hickox *et al.* (2004) suggest that a soft excess is present in most, if not all, BeXRB spectra but is not always detected due to the high levels of intrinsic absorption or low source flux. Recent observations with *XMM-Newton*

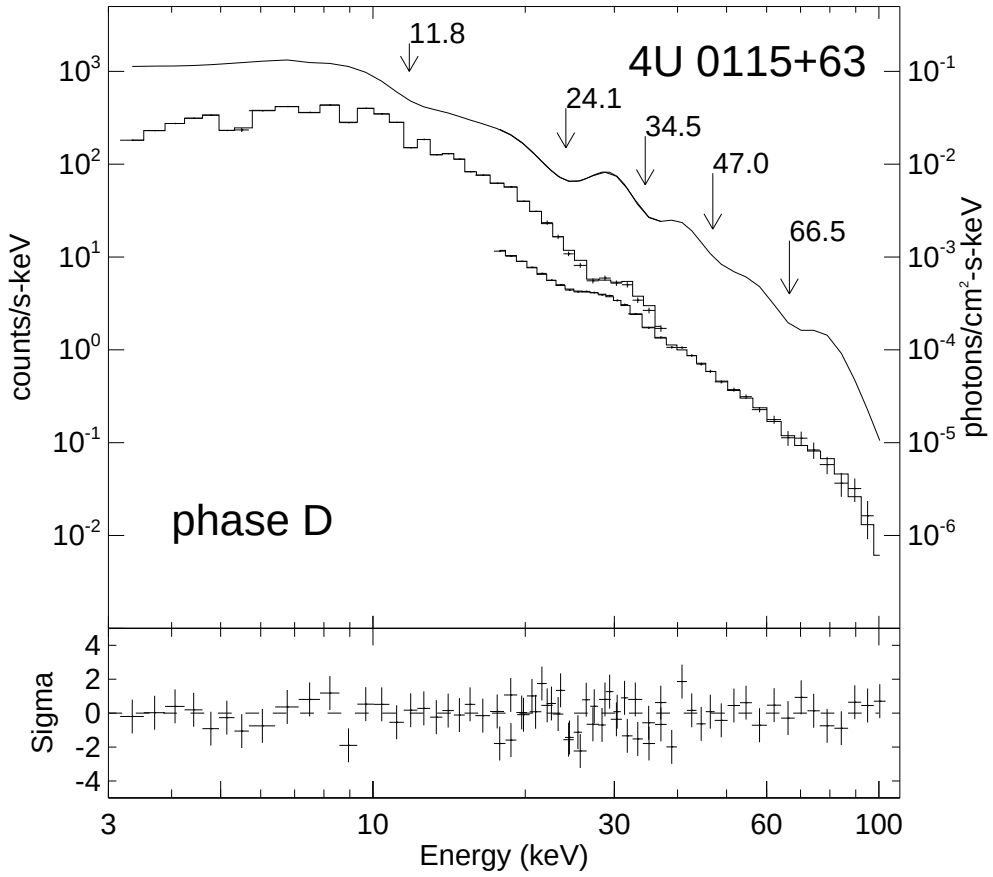

Figure 1.8: X-ray spectrum of 4U 0115+63 taken from Heindl *et al.* (1999), along with best fit model (solid line). This pulsar possesses as many as five CRSF features, the most ever seen in an HMXB.

has revealed that a handful of BeXRBs have blackbody components with kT_{BB} in excess of 1 keV and a derived emitting region $R < R_{NS}$. Such a small radius indicates emission from a hot spot on the neutron star, possibly from the magnetic polar cap. These sources all have low level X-ray emission ($L_X \sim 10^{34-35}$ ergs s^{-1}) and long pulse periods (P>100 s).

A number of HMXB spectra have Cyclotron Resonance Scattering Features (referred to as CRSFs or cyclotron lines). First observed in Her X-1 (Trümper *et al.*, 1978), these appear as broad absorption lines in the spectrum and are currently the only feature of HMXBs that allow for direct measurement of the magnetic field of a neutron star. They arise from electrons close to the neutron star surface. Their motion perpendicular to the magnetic field is quantised in Landau orbits, corresponding to the discrete energy levels of the electrons. Photons with these energies are absorbed and scattered isotropically. The cyclotron line energies, E_{cyc} can be

obtained by substituting Equation 1.25 into $E = \hbar\omega$:

$$E_{cyc} = n\frac{\hbar eB}{m_e} = 11.57nB_{12}\text{keV} \tag{1.32}$$

Where n is the line number (i.e. $n = 1$ is the fundamental, $n > 1$ is the nth harmonic).

Emission lines are also occasionally present in the X-ray spectra of HMXBs and are indicative of X-ray reprocessing by material out of the direct line of sight. Fürst *et al.* (2011) identify eight fluorescence lines in the spectrum of GX 301-2, the strongest of which is the Fe Kα line due to the high fluorescence yield (0.34, Bambynek *et al.* 1972) and abundance of iron. When the data are split into several time intervals, the equivalent width (EW) of the Fe Kα is clearly correlated with the absorbing column density, which confirms that the absorbing and emitting medium are in fact the same thing.Torrejón *et al.* (2010) report narrow, time variable Fe Kα lines in the 10 HMXBs in their survey. This could be due to the motion of the neutron star (the source of the X-rays) relative to the absorbing/fluorescing material. In contrast the Fe-Kα lines in LMXBs are generally broad as they originate from a different region: the accretion disc. The rotation of the disc, the thermal motion of the atoms and the temperature gradient all act to smear out the emission line. The ratio of elemental Kα and Kβ (if observed) yields valuable information about the elemental abundance of the fluorescing material.

An extreme example of an X-ray spectrum of an HMXB is shown in Figure 1.8 along with the best fit model spectrum. The spectrum is fit with an absorbed cutoff powerlaw, a blackbody with temperature $KT_{BB} \sim 0.4$ keV and multiple cyclotron lines. This particular source (4U 0115+63, Heindl *et al.* 1999) has the highest number of CRSF features ever observed: the fundamental and four harmonics ($n = 1-5$, see Equation 1.32). No Fe-Kα line is apparent in the data.

The pulse periods of HMXB pulsars range between 1 and 1000 s, slower than the accretion powered pulsars in LMXBs. This is thought to be because, as these systems are older, they have had prolong periods of accretion in the past which have spun them up to millisecond periods. The HMXBs have complex spin up and spin down histories, with short term variations as well as long term trends (see Bildsten *et al.* 1997 for several examples).

The pulse profiles of HMXBs come in a variety of shapes, from simple sinusoidal to triple peaked, asymmetric structures (e.g. Galache *et al.* 2008). This can be due to the accretion geometry with a sinusoid shape for a pencil beam and a more complex double peak, flat top structure for a fan beam. The critical luminosity for a shock formation, derived by Basko and Sunyaev (1976), is $L_{crit} \gtrsim 10^{37}$ erg s^{-1}

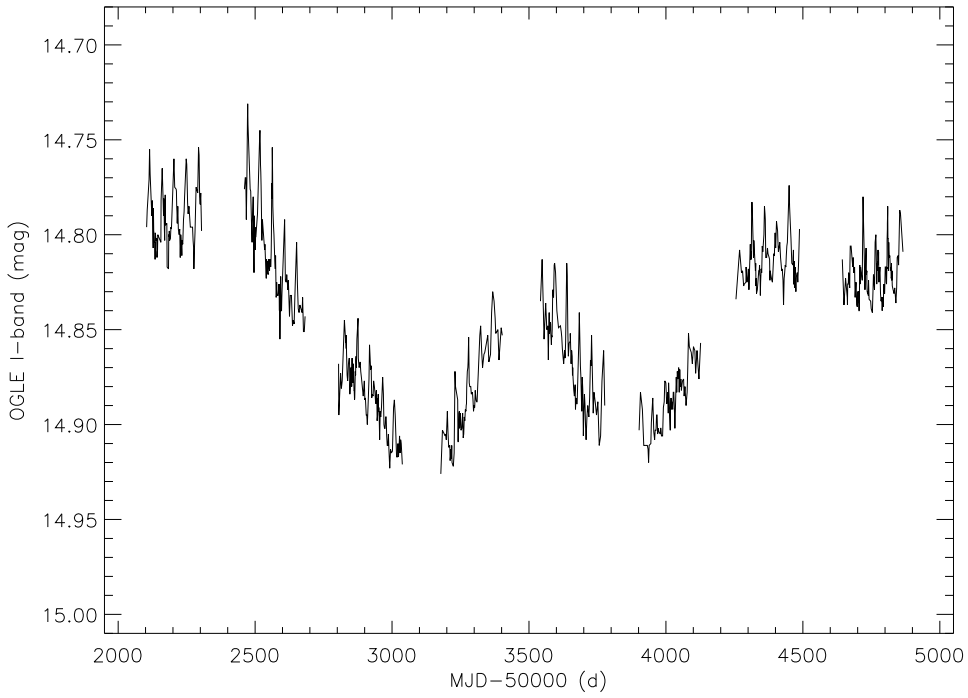

Figure 1.9: An example I-band lightcurve of a BeXRB (taken from Townsend 2012). The regular periodic decrease in magnitude (increase in flux) is attributed to the periastron passage of the neutron star whilst the underlying aperiodic variation is explained by changes in the size of the circumstellar disc

and as such sources have been seen to switch between accretion geometries as their luminosities changes (e.g. EXO 2030+375 Parmar *et al.* 1989; Sasaki *et al.* 2010). The pulse profile shape observed is also dependent on the inclination of the system, the angle between the magnetic and rotation axis and energy, as the regions emitting the X-rays become more compact (Lutovinov and Tsygankov, 2008).

1.4.4 Optical Properties

Figure 1.9, taken from Townsend (2012), shows the *I*-band light curve of SXP7.78 and is an example of a typical BeXRB light curve. The optical light curves of BeXRBs and sgXRBs are often complex with many different periodic components. Each of these components has with distinctive timescales of variation, superimposed on seemingly random fluctuations, linked to changes in the circumstellar disc size. Bird *et al.* (2012) discuss the optical lightcurves of BeXRBs and the detection of orbital periods in detail and identify three periodic components:

- Radial and non radial pulsations with variations on timescales of 0.1-2.0 days.
- Disturbances in the circumstellar disc caused by the periastron passage of the

neutron star. These correctly identify the binary period and range from tens to hundreds of days.

- "Superorbital" periods from warped and/or precessing circumstellar discs with timescales from hundreds to thousands of days.

For an in depth discussion of the superorbital periods in BeXRBs see Rajoelimanana *et al.* (2011).

The optical spectra of HMXBs are very similar to those of isolated Be and supergiant stars. The spectra are dominated by the Doppler broadened Hydrogen Balmer series (due to the rotation of the star) and exhibit the ionised helium and metal lines typical of hot OB stars, such as HeII, SiIV and MgII (Walborn and Fitzpatrick, 1990; Lennon, 1997; Evans *et al.*, 2004). The circumstellar environment gives rise to the Balmer emission lines of hydrogen, most notably Hα, as ionised hydrogen recombines in the disc. A strong infrared (IR) excess is also associated with the disc due to free-free emission - i.e. emission from the acceleration of free electrons as they are deflected by the ionised hydrogen in the disc. A strong correlation exists between these two features, supporting the hypothesis of a common origin.

The Hα profiles of several binary and isolated Be stars have shown time variable, asymmetric double peaks. This is quantified by the ratio of the strengths of the two peaks and is referred to as V/R (McLaughlin, 1961) variability, where V is the peak towards the violet end of the spectrum and R the peak towards the red end. V/R variability has timescales of years to decades - much longer than the orbital periods of these systems. The double peak can be explained by blue and red shifted sides of the disc and requires the system to be inclined to the line of sight. The asymmetry requires the disc density to be non-uniform. Okazaki (1991) (and subsequently Okazaki 1996; Papaloizou *et al.* 1992) successfully describe this behaviour with a one armed density wave in the disc, a model first suggested by Kato (1983). These are termed global one-armed oscillations. Figure 1.10 shows the V/R behaviour of LS I $+61^\circ$ 235, monitored by Reig *et al.* (2000) over the course of $\sim$5 years. They derive a *V/R* quasi-period of $\sim 1240 \pm 30$ days.

The emission lines in the supergiant systems often exhibit P Cygni profiles. These are the result of a blue shifted absorption feature, originating in the strong stellar wind directly in the line of sight, superimposed on the emission feature, seen at the expected wavelength (e.g. Balan *et al.* 2010). There are too few confirmed sgB[e]-XRBs to reach a concensus on the "typical" optical spectrum of these systems. However, these sources appear to be unaffected by the presence of a binary counterpart (Hynes *et al.*, 2002). The two component winds of isolated sgB[e] stars

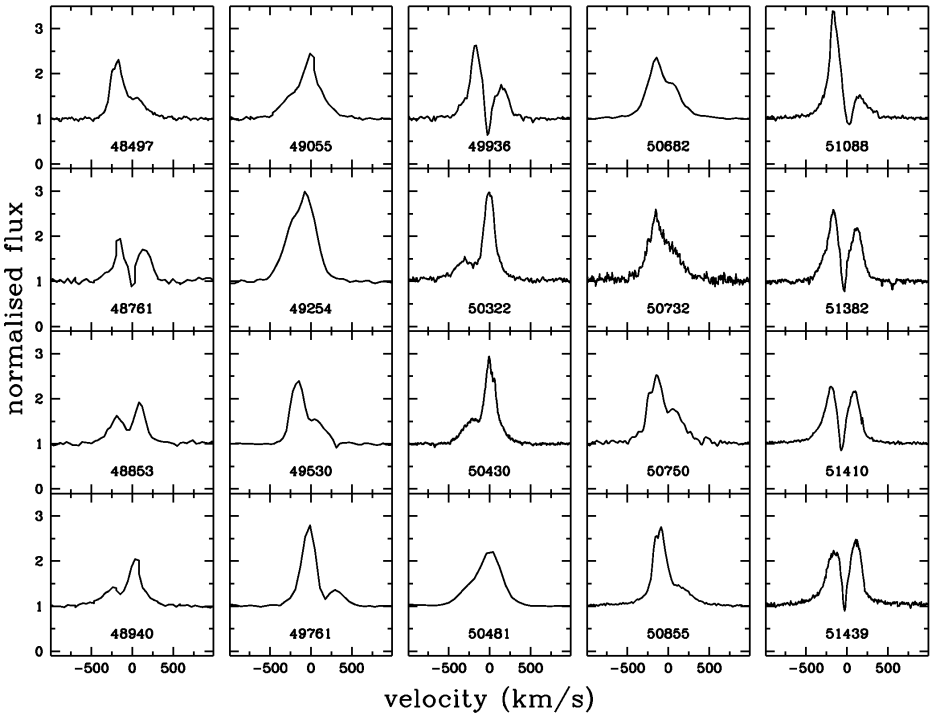

Figure 1.10: V/R variability observed in the Hα line profile of LS I $+61^\circ$ 235. Taken from Reig *et al.* (2000)

lead to complex optical spectra, rich in emission lines. Both narrow, low excitation metal lines and broad, high excitation species are present, originating in the equatorial and polar winds respectively (see Section 1.4.2.1). Forbidden emission lines of heavier elements such as iron, sulphur, oxygen and nitrogen also feature prominently in the spectra and again originate in the disc. For a full discussion of the optical properties of sgB[e] stars, see Zickgraf *et al.* (1985); Zickgraf (2003, 2006).

1.5 HMXBs as a Population

1.5.1 XRB Environments and the Magellanic Clouds

The lifetimes of XRBs are predominantly determined by the lifetime of the secondary star. As this is strongly dependent on the stellar mass (see Section 1.1) there is a large disparity in the lifetimes of LMXBs and HMXBs and where they are located in our Galaxy. HMXBs are short lived ($\sim 10^5 - 10^7$ yr) and are found in star forming regions and younger stellar populations. In contrast, LMXBs are found in older stellar populations such as globular clusters and have lifetimes of order ($10^7 - 10^9$ yr). The short lifetimes of HMXBs make them strong tracers of recent

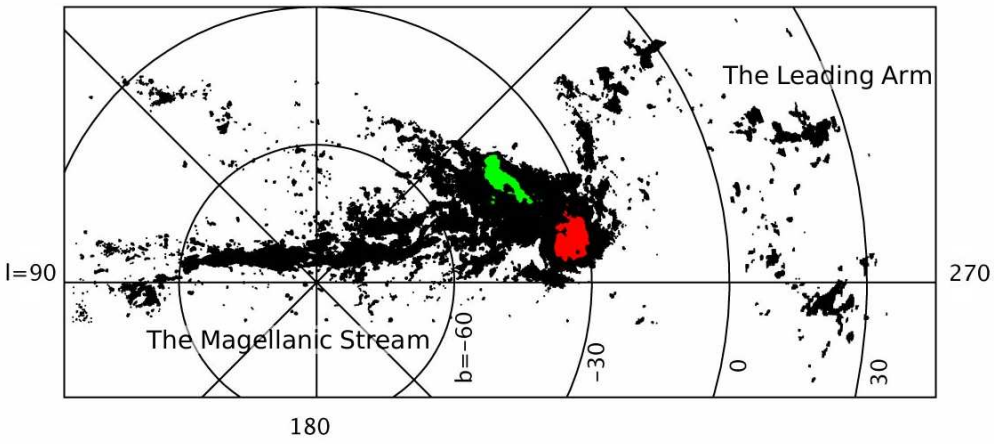

Figure 1.11: HI observations of the Magellanic Clouds. The LMC is shown in red, the SMC in green. Figure taken and modified from Diaz and Bekki (2011)

star formation episodes in a galaxy. One galaxy with an apparent over abundance of HMXBs is the Small Magellanic Cloud.

The Large and Small Magellanic Clouds (LMC and SMC respectively) are satellite galaxies of the Milky Way (MW), located at a distance of ~ 60 kpc. The two galaxies have been heavily disrupted due to past interactions with each other and the MW. When viewed at radio wavelengths (see Fig. 1.11), the SMC and LMC appear to be embedded in an extended neutral hydrogen cloud, connected by the Magellanic Bridge (Irwin *et al.*, 1990) and trailed by the Magellanic Stream (Mathewson *et al.*, 1974). More recently another region of neutral hydrogen has been identified: the leading arm (Putman *et al.*, 1998). The leading arm is predicted by tidal models (e.g. Gardiner and Noguchi 1996) and its detection establishes tidal interactions as the agent of disruption in the Magellanic Clouds.

As the less massive of the Magellanic Clouds, the SMC has experienced greater disruption due to these tidal interactions. Figure 1.12 shows the force experienced by the SMC due to these interactions, modelled by Diaz and Bekki (2011). Harris and Zaritsky (2004; 2009) report that the SMC and LMC had "bursts" of star formation at 2.5 and 0.4 Gyr ago (with the SMC experiencing an additional burst at 0.06 Gyr), approximately coincident with minima in the SMC-LMC separation. This suggests that the episodes of star formation were induced by these tidal interactions, giving rise to the present number of HMXBs in the SMC.

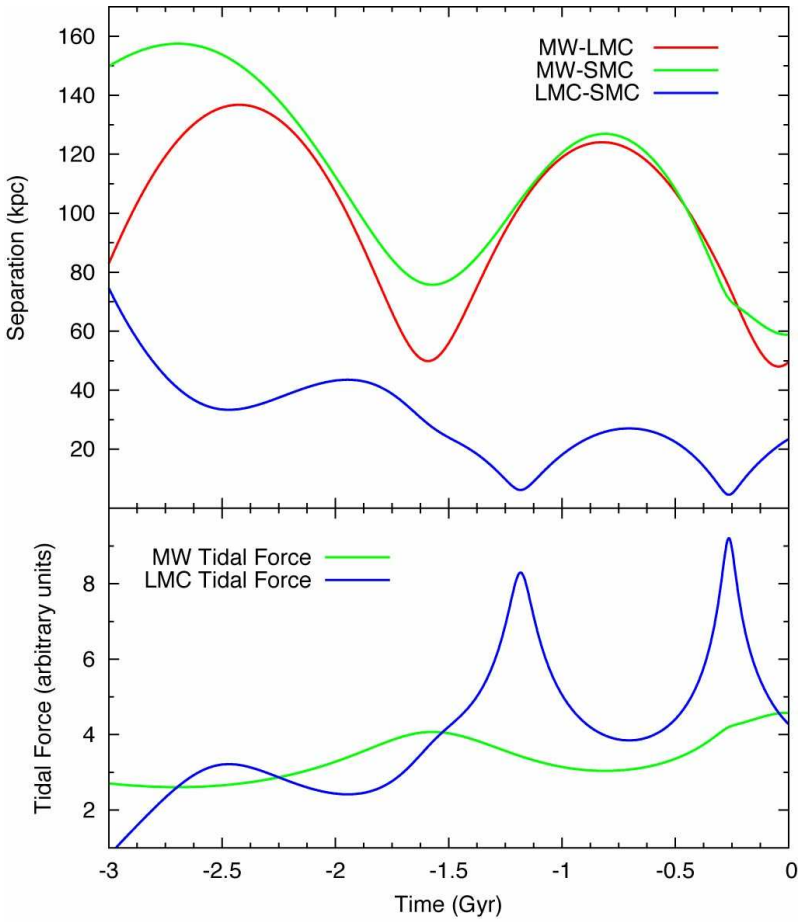

Figure 1.12: Figure taken from Diaz and Bekki (2011). Top panel shows the Separations between the LMC, SMC and MW over the last 3 Gyr. Bottom panel shows the tidal for experienced by the SMC exerted by the MW and LMC.

1.5.2 The L_X-Star Formation Rate Relation

Grimm *et al.* (2003) have quantified the relationship between the star formation rate (SFR) and the number of sources with X-ray luminosities in excess of 10^{38} ergs s^{-1} in a galaxy.

$$\text{SFR } (\text{M}_\odot \text{ yr}^{-1}) = \frac{N(L > 2 \times 10^{38} \text{erg s}^{-1})}{2.9} \tag{1.33}$$

However BeXRBs do not reach these luminosities. One of the reasons for choosing such a high threshold luminosity was to avoid contamination from any LMXBs present in any of the galaxies studied (which have been shown to scale linearly with the mass of the host galaxy, Gilfanov 2004).

The left panel of Figure 1.13, taken from Grimm *et al.* (2003), shows the X-ray luminosity functions of several galaxies, including the SMC. The right panel shows the same functions normalised to the SFR of the Antennae galaxy. Whilst the relationship is evident, the individual luminosity functions are “snapshots” of a galaxy

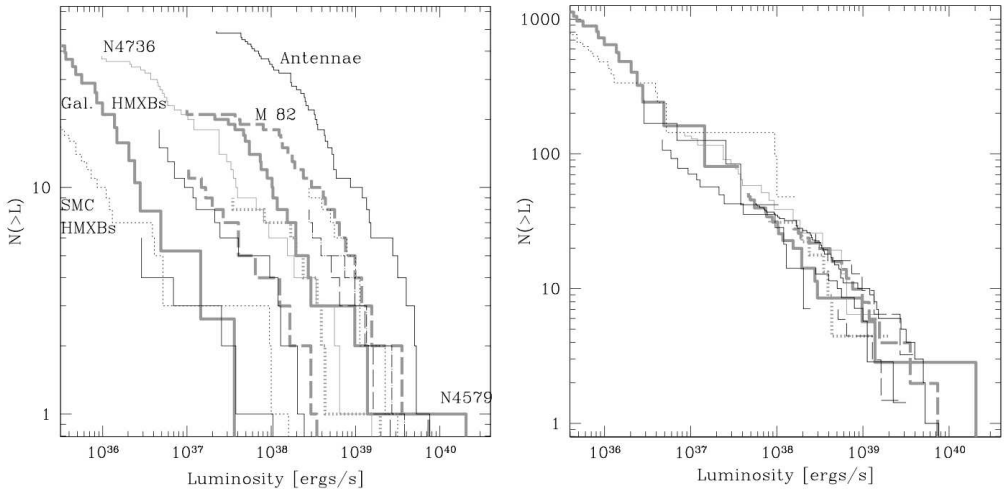

Figure 1.13: The normalised (right) and unnormalised (left) luminosity functions of compact X-ray sources in nearby galaxies. The luminosity functions in the normalised panel have been scaled to that of Antennae. Figure taken from Grimm *et al.* (2003)

and may not be representative of the underlying population (though the authors note that by using the luminosity functions of several galaxies, their conclusions should be unaffected by this). Thus predicting the number of HMXBs in a galaxy cannot be done with great accuracy.

A general formula for the number HMXBs given by equation (7) of Grimm *et al.* (2003)

$$N(>L) = 5.4\ \mathrm{SFR}(L_{38}^{-0.61} - 210^{-0.61}) \tag{1.34}$$

This predicts ~ 1 HMXB with a luminosity in excess of 1×10^{38} erg s^{-1} in the SMC, which agrees with observations: Only the sgXRB SMC X-1, consistently reaches these luminosities (Inam *et al.*, 2010). If we assume that the relationship remains valid down to X-ray luminosities of 5×10^{35} ergs s^{-1} (the typical luminosity of the lower Type I outbursts seen in the SMC, Haberl *et al.* 2008b) then equation 1.34 predicts 20 HMXBs with $L_X > 5\times10^{35}$ ergs s^{-1} (adopting the same value for the SFR as Grimm *et al.* 2003, 0.15 M$_\odot$ yr^{-1}, taken from Yokogawa *et al.* 2000; Harris and Zaritsky 2004). Using the same SFR and a X-ray luminosity of 1×10^{34} ergs s^{-1} (the quiescent level of BeXRBs, Laycock *et al.* 2010) predicts 223 HMXBs. Neither of these values accurately reflects the HMXB population in the SMC: there are currently $\sim$60 known HMXBs in the SMC (Liu *et al.*, 2005), of which $\sim$55 are X-ray pulsars). In contrast, the HMXB population of the LMC is similar to that of the MW. There are currently 36 known HMXBs in the LMC, including $\sim$ 13 pulsars and several supergiant systems and black hole candidates.

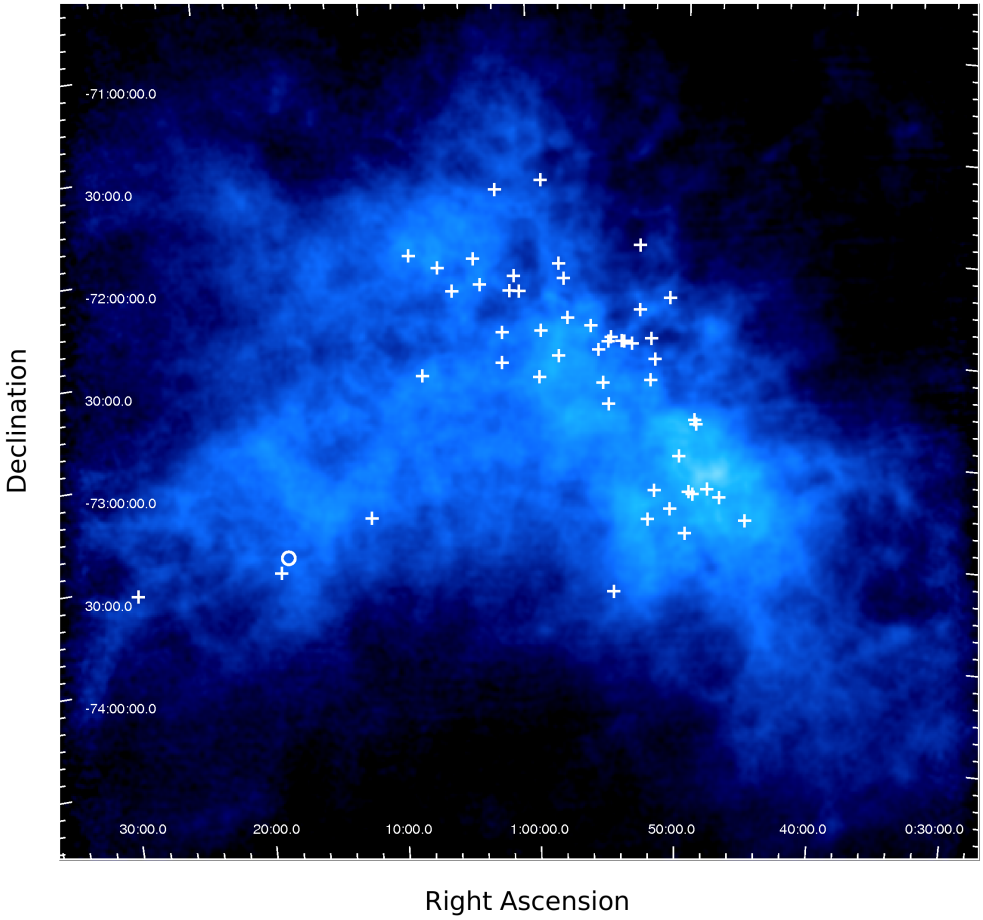

Figure 1.14: HI image of the SMC (taken from Stanimirovic *et al.* 1999) with location of HMXBs with known positions marked. The circle marks SMC X-1, the only known sgXRB in the SMC.

A recent *INTEGRAL* monitoring campaign of the SMC and 47 Tuc by McBride *et al.* (2010) identified two BeXRBs in the Magellanic Bridge and proposed a further three HMXB candidates. Along with the previously known BeXRB in the Magellanic Bridge (RX J0209.6-7427, Kahabka and Hilker 2005), this increases the potential Magellanic Bridge HMXB population to six sources.

The stellar winds of massive stars are known to be line driven (see Section 1.4.2) and so a lower metallicity will lead to less mass being lost from the compact object progenitor. This in turn is expected to affect the number of systems that survive the initial supernova explosion and go on to form HMXBs. Dray (2006) use simulations to demonstrate that this is indeed the case but are unable to replicate the number and period distribution of the SMC HMXBs with a low metallicity environment alone. A possible reason for this discrepancy could be the activity cycles of BeXRBs.

Figure 1.14 shows an HI image of the SMC along with the locations of the 55

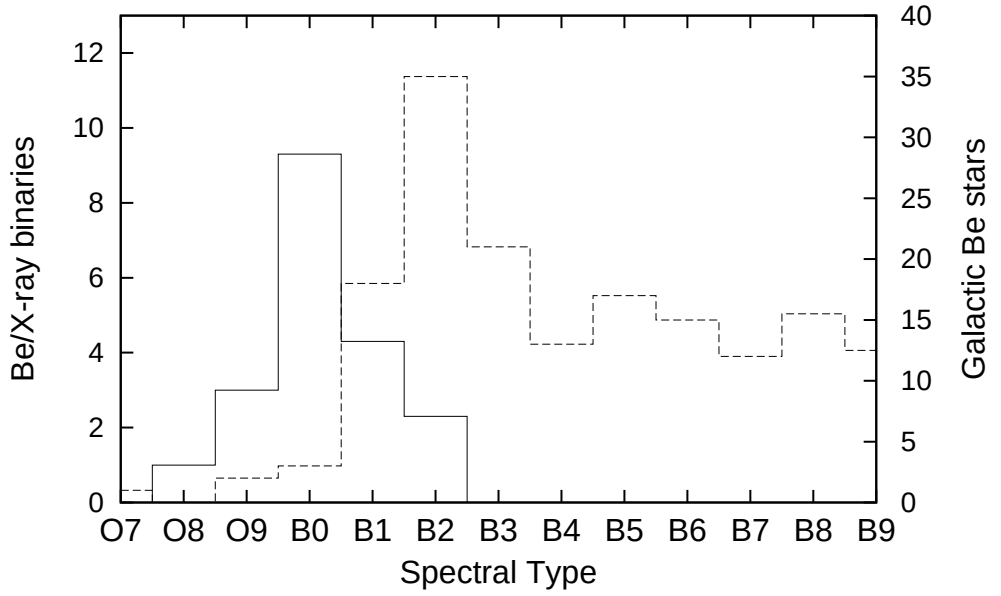

Figure 1.15: The spectral distribution of isolated Be stars (broken line) and BeXRB counterparts (solid line) in the Milky Way. Taken from McBride *et al.* (2008)

pulsars with known positions. The SMC is divided into two sections, the "Wing" and the "Bar". Most of the pulsars are located in the Bar of the SMC, whilst SMC X-1 is located in the sparsely populated Wing. Whilst this may be partly due to a selection effect (as most surveys have concentrated on the Bar of the SMC, Galache *et al.* 2008), McGowan *et al.* (2008) and Laycock *et al.* (2010) have imaged the Wing of the SMC with *the Chandra X-ray Observatory* down to a limiting luminosity $\sim 10^{32-33}$ erg s^{-1} and not discovered a large population. Thus we can conclude that the apparent difference in the SMC Wing and Bar HMXB population is genuine. Antoniou *et al.* (2010) argue that this could be due to the donor stars, as the Be phenomenon peaks at age $\sim$40 Myr (McSwain and Gies, 2005). This means that a HMXB population with main sequence companions $\sim$ 40 Myr old will have the largest ratio of Be/B stars. HMXBs with main sequence companions older or younger than this are less likely to display the Be phenomenon which is necessary for the production of X-rays.

1.5.3 Spectral distribution of BeXRBs

The Be phenomenon is difficult to quantify due to its transient nature. Zorec and Briot (1997) find that the frequency of Be stars among Galactic B stars is a function of spectral type, peaking at 34% for B1 stars and falling to 8% for B9 stars. However, the actual number of Be stars peaks at later spectral types. Figure 1.15,taken

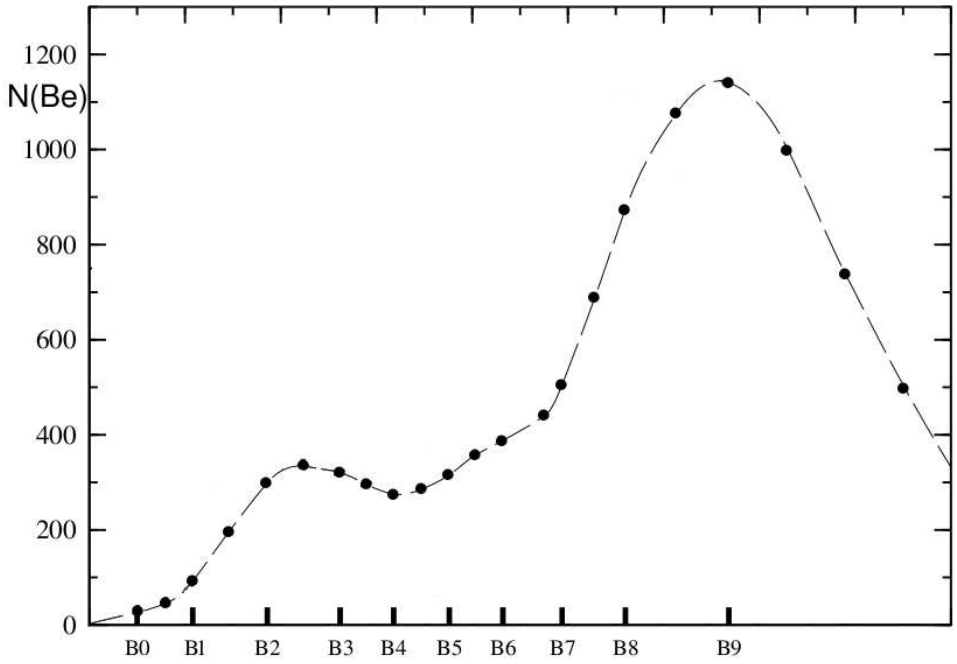

Figure 1.16: The number of Be stars in the Galaxy as a function of spectral type. (Edited from Zorec and Briot 1997)

from McBride *et al.* (2008), shows the spectral distribution of isolated Be stars in the Galaxy along with the spectral distribution of the optical counterparts in BeXRB. The isolated Be star data are taken from the work of Slettebak (1982) which has a limiting V-band magnitude of ~ 6.0 mag. McBride *et al.* (2008) note that this magnitude will favour the detection of early type Be stars and so the distribution of the isolated Be stars may not be complete at the later spectral types. Figure 1.16, edited from Zorec and Briot (1997), shows the number of observed Be stars as a function of spectral type for all luminosity classes. McBride *et al.* (2008) expand on the work of Negueruela (1998) who use a Kolmogorov-Smirnov (KS) test to confirm that the spectral distribution of the optical counterparts in BeXRBs is significantly different to that of isolated Be stars.

One would naively assume that, as the earlier type stars are more massive than the later types ($M_{B0V} = 17.5 M_{\odot}$, $M_{B8V} = 3.8 M_{\odot}$, Cox 2000), the binaries with counterparts later than B3 do not survive the supernova. However, Portegies Zwart (1995) demonstrated that the kick velocity imparted to the system by the supernova has very little effect on the spectral distribution of BeXRB counterparts. It is the angular momentum lost from the system which has the most pronounced effect on the mass distribution of secondaries, with a large loss per unit mass truncating the mass distribution at >8 M$_{\odot}$ or B2V spectral class.

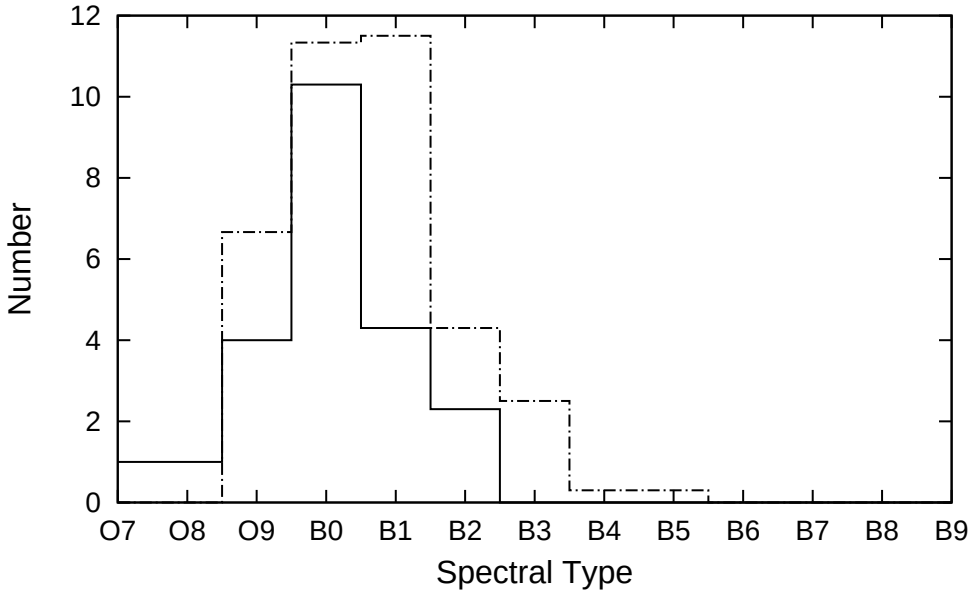

Figure 1.17: The spectral distribution BeXRB counterparts in the Galaxy (solid line) and the SMC (broken line). Taken from McBride *et al.* (2008)

Maeder *et al.* (1999) show that the number ratio of Be to B stars in the spectral range O9-B3 appears to be higher in the LMC and SMC (0.23 and 0.39 respectively, compared with 0.11 and 0.19 for the interior and exterior of the MW). McBride *et al.* (2008) use the same statistical test as Negueruela (1998) to compare the spectral distribution of the Galactic BeXRBs with that of the SMC, shown in Figure 1.17. Despite the very different environments, the KS test suggests that the two spectral distributions of optical counterparts are drawn from the same parent population. This, along with the results of Dray (2006), suggest that although the number of HMXBs may be effected by the metallicity, the spectral distribution of the counterparts is not.

1.5.4 The H$\alpha - P_{orb}$ Relation

The Hα emission of Be stars is linearly correlated with the effective surface area of the disc (e.g. Tycner *et al.* 2005). For many years it was thought that the circumstellar envelope of the Be star in BeXRBs was unaffected by the neutron star, however this was challenged by Reig *et al.* (1997) who reported a relationship between the orbital period of the BeXRB (P_{orb}) and the Hα equivalent width (EW). Figure 1.18 shows the most recent version of the P_{orb}-EW(Hα) diagram, taken from Reig (2011). A detailed comparison of the Hα emission of BeXRBs compared to that of isolated Be stars showed that the emission lines in BeXRBs are consistently weaker (i.e. have smaller EWs, Zamanov *et al.* 2001). Both of these effects

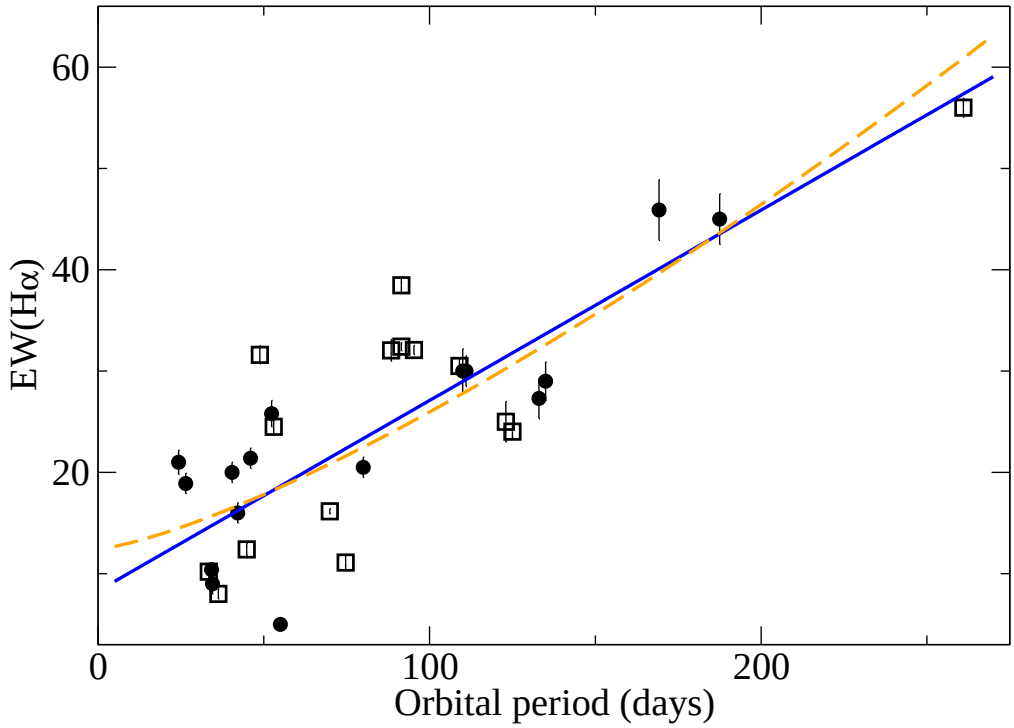

Figure 1.18: Diagram of P_{orb}-EW(Hα taken from Reig (2011). Solid line is best linear fit to the data, broken line represents a power-law fit with exponent n=4/3.

are attributed to the presence of the neutron star which truncates the circumstellar disc. The truncation radius depends on the orbital parameters of the system and the viscosity. Qualitatively, BeXRBs with longer orbital periods (i.e. larger semi major axes) have larger truncation radii. BeXRBs with lower eccentricities also have larger truncation radii. For a rigorous description of tidal truncation in BeXRBs, see Negueruela and Okazaki (2001) and Okazaki and Negueruela (2001).

1.5.5 The $P_{spin} - P_{orb}$ Relation

The different HMXBs occupy different areas on the $P_{spin} - P_{orb}$ diagram, shown in Figure 1.19. Corbet (1984, 1985, 1986) first identified a relationship between P_{orb} and P_{spin} values of BeXRBs. The spin period observed is assumed to be the equilibrium period mentioned in Section 1.2, at which $r_A = r_{co}$. Equations 1.19 and 1.16 show the relationship between r_{co} and P_{spin} and r_A and ρ respectively. The density is linked to the separation of the system, which in turn is linked to P_{orb}. Corbet (1985) showed that it is in fact the separation of the bodies at periastron rather than the semi-major axis, which adds an eccentricity dependence. Observationally, the relationship is quantified by $P_{spin} \propto P_{orb}^2$. The values of P_{spin} observed are generally greater than that implied by Equation 1.21, suggesting that there is a wide range

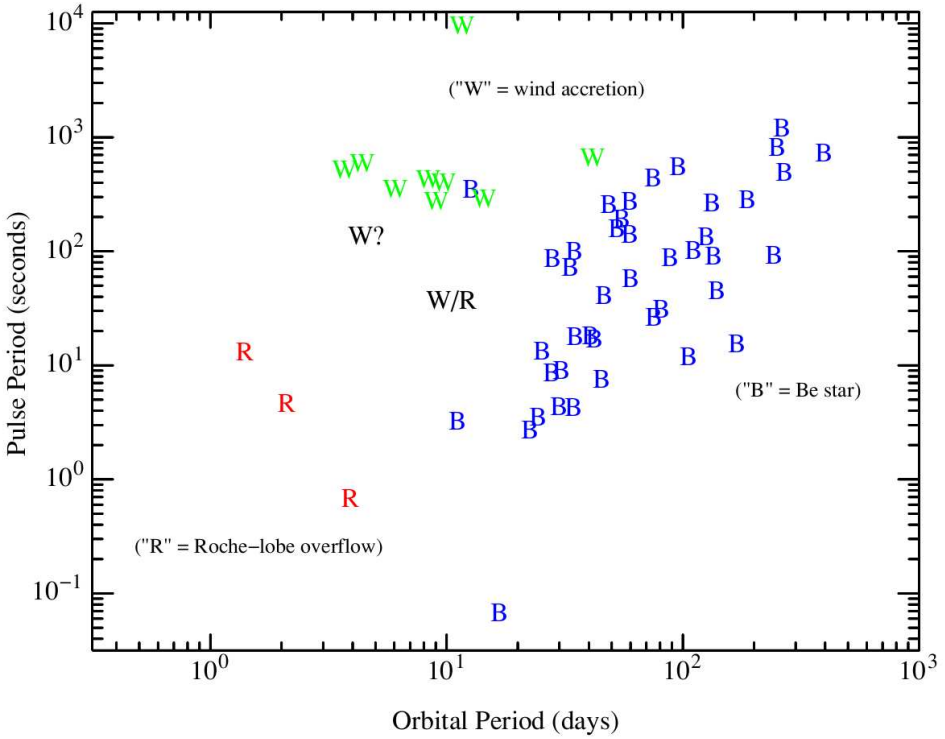

Figure 1.19: The $P_{spin} - P_{orb}$ diagram, better known as the "Corbet" diagram. Plot includes systems from the SMC, LMC and MW. Taken from Corbet *et al.* (2006)

of values for R_{NS}, M_{NS} and B. Corbet (1986) mention that there appears to be an anti-correlation in the P_{orb} and P_{spin} values of the Roche-Lobe overflow sgXRBs, however they note that it is difficult to draw any conclusions with only 3 sources.

More recently Knigge *et al.* (2011) demonstrated that the BeXRB pulsars in the SMC can be split into two sub populations based on their pulse periods. This is a statistically significant result with a KMM test giving a probability that the sources were drawn from a single Gaussian of 7×10^{-6} for the combined SMC, LMC and MW samples (Ashman *et al.* 1994, see Fig. 1.20). They go on to state that the result is still significant even when only the spectroscopically confirmed BeXRBs are considered. The authors interpret this bi-modality as evidence for two formation channels for BeXRBs. This will be discussed in more detail in the Chapter 5.

1.5.6 The $\dot{P} - PL^{\frac{3}{7}}$ Relation

Ghosh and Lamb (1979) consider the contribution of various stresses to the torque that acts on a neutron star accreting from a Keplerian disc. They derive a relationship between the spin up of the neutron star, $-\dot{P}$, and the quantity $PL_{37}^{3/7}$, where P is the spin period of the neutron star (referred to as P_{spin} thus far). Whilst this relationship is far from simple, it does imply that, when plotted logarithmically,

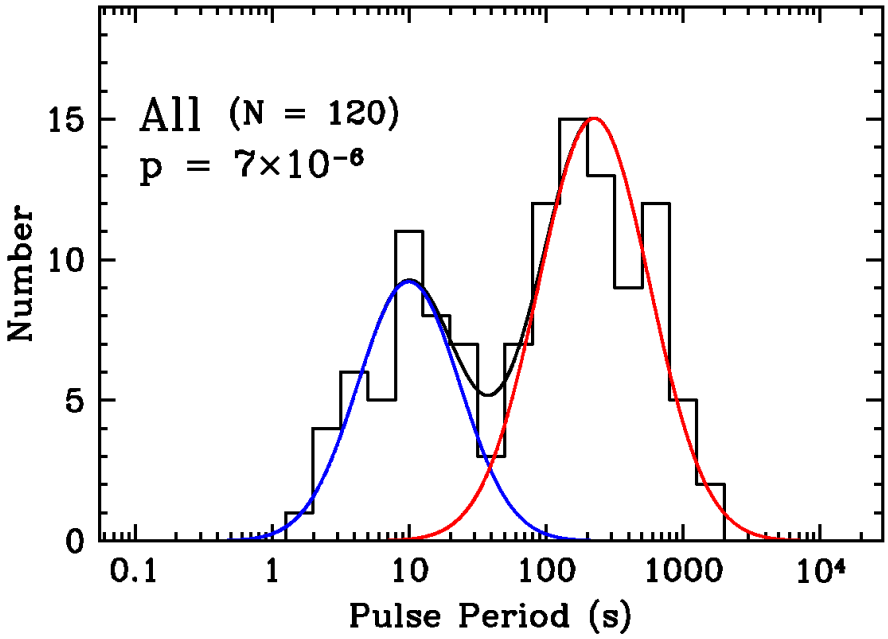

Figure 1.20: The double Gaussian decomposition of the $logP_{spin}$ values of Galactic, SMC and LMC BeXRBs, as suggested by the KMM algorithm implemented by Knigge *et al.* (2011). Figure modified from Knigge *et al.* (2011)

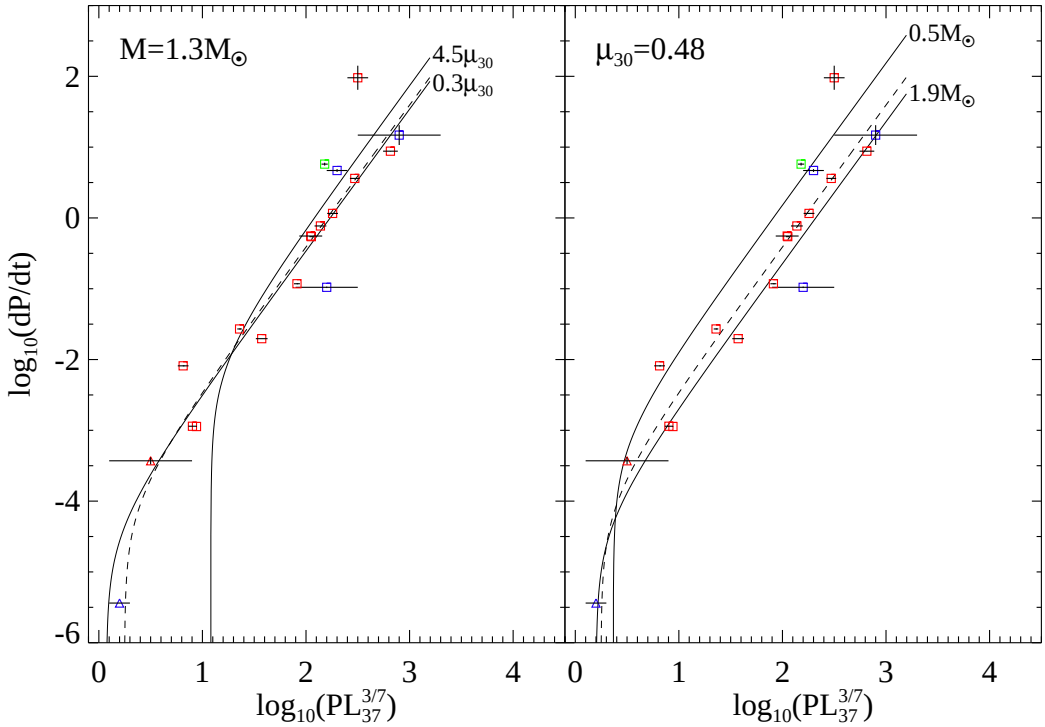

Figure 1.21: An updated $log_{10}(-\dot{P}) - log_{10}(PL^{\frac{3}{7}})$ diagram (where $P = P_{spin}$). The triangles represent the sgXRBs, squares the BeXRBs. Blue symbols are for the Galactic sources, red the SMC and Green the LMC.

there should be a rough correlation in these two values. Figure 1.21 shows the $-\dot{P} - PL_{37}^{3/7}$ plot with the original data set used by Ghosh and Lamb (1979) along with any SMC and LMC BeXRBs with known $-\dot{P}, L_X$ and P_{spin} (taken from Coe *et al.* 2010 and Klus *et al.* 2013). Theoretical curves for given values of μ_{30} and M_{NS} are overplotted and highlight the importance of this work: that fundamental properties of the pulsars can be inferred from observational measurements.

1.6 Thesis Overview

In this Chapter I have discussed the optical, infra red and X-ray properties of XRBs, with particular emphasis on the HMXB systems. I have outlined how these systems are formed and discussed the nature of the compact object and the donor star both individually and as a system. I have introduced the relevant accretion and emission mechanisms referred to throughout this thesis. Progress on understanding HMXBs can come from studies of individual sources, or of larger well-defined populations of **sources**. In the latter case, the Magellanic clouds are key targets as they provide populations at known distances and with (fairly) well-known formation histories. In the first half of this thesis, I discuss individual sources: Chapter 2 discusses the result of an *XMM-Newton* target of opportunity observation of a newly discovered BeXRB in the LMC as well as the optical follow up from the original detection. In Chapter 3 I present X-ray observations of XTE J0421+560/CI Camelopardalis, a Galactic sgXRB. In both of these Chapters I use simultaneous timing and spectral analysis to constrain the system geometry. Chapter 4 describes the work being done to expand the number of known HMXBs by observing the Phoenix dwarf galaxy, a Local Group dwarf irregular galaxy which shares many similarities with the SMC. In Chapter 5 I discuss why the BeXRB population of the SMC is ideal for population studies and outline the work done to search for evidence for two different neutron star formation channels.

”Ford!” he said, ”there’s an infinite number of monkeys outside who want to talk to us about this script for Hamlet they’ve worked out.”

THE HITCHHIKER’S GUIDE TO THE GALAXY (1979)

2

XMM-Newton observation of the highly magnetised accreting pulsar Swift J045106.8-694803: Evidence of a hot thermal excess

In this Chapter I present recent X-ray and optical observations of Swift J045106.8-694803, a newly discovered HMXB in the LMC. I classify the optical counterpart of Swift J045106.8-694803 as a B0-1III-V star, confirming it as a BeXRB. I determine the spin period to be 168.5±0.2 s as of MJD = 56125.0. The spectral analysis reveals for the first time the presence of a blackbody with temperature $kT_{BB} = 1.8^{+0.2}_{-0.3}$ keV and radius $R_{BB} = 0.5 \pm 0.2$ km. The pulsed fraction decreases with increasing energy and the ratio between the hard (>2 keV) and soft (<2 keV) lightcurves is anticorrelated with the pulse profile. Simulations of the spectrum suggest that this is caused by the pulsations of the blackbody being $\sim \pi$ out of phase with those of the power law component. Using a simple model for emission from hot spots on the neutron star surface, my collaborator, Dr. Wynn Ho, fit the pulse profile of the blackbody component and constrain the angle between the rotation

and magnetic axes α and the angle between the rotation axis and line-of-sight ζ to be $(\alpha,\zeta) \sim (53^\circ, 70^\circ)$ or $(70^\circ, 53^\circ)$ for $M = 1.4M_\odot$ and $R = 12$ km. The optical spectroscopy presented here was included in Klus *et al.* (2013).

2.1 Introduction

The number of known HMXBs (and by extension BeXRBs) has increased dramatically since the launch of satellites such as *ROSAT* and *RXTE* particularly in the Magellanic Clouds (see Chapter 1). Given the large sample size of objects now available, we are able to study the properties of these objects on a statistically significant scale. Many authors have reported the presence of a soft excess in spectra of some BeXRBs, with blackbody temperatures kT_{BB}<0.5 keV (e.g. Sturm *et al.* 2012b) attributed to the inner edge of an accretion disc surrounding the neutron star. Hickox *et al.* (2004) suggest that a soft excess is present in most, if not all, BeXRB spectra but is not always detected due to the high levels of intrinsic absorption or low source flux.

Recent observations with *XMM-Newton* have revealed that a handful of BeXRBs have blackbody components with kT_{BB} in excess of 1 keV and a derived emitting region $R < R_{NS}$ (see Table 2.1). Such a small radius indicates emission from a hot spot on the neutron star, possibly from the magnetic polar cap. These sources all have low level X-ray emission ($L_X \sim 10^{34-35}$ erg s^{-1}) and long pulse periods (P>100 s).

Here I report on X-ray and optical observations of another possible member of this group of BeXRBs: Swift J045106.8-694803. This source was detected in the LMC by the *Swift*/BAT hard X-ray survey (Beardmore *et al.*, 2009) and was followed by a 15.5 ks observation with the *Swift* XRT instrument. This confirmed the position of the source and revealed a periodic signal at 187 s. From the accretion model of Ghosh and Lamb (1979), Klus *et al.* (2013) derived a magnetic field $B \sim 1.2 \times 10^{14}$ G from the spin-up rate, indicating that Swift J045106.8-694803 is a highly magnetised accreting pulsar (i.e., neutron star with $B \gtrsim B_{crit}$; see equation 1.27).

Table 2.1: Summary of sources with $kT_{BB}>1.0$ keV. R_{BB} is the radius of the emitting region implied by L_X and kT_{BB}. D is the assumed distance to the source in kpc. All errors are 90% confidence level.

Source	Period	kT_{BB}	L_X	R_{BB}	D	Energy Range	Reference
	s	keV	erg s^{-1}	m	kpc	keV	
RX J0146.9+6121	1396.1 ± 0.3	$1.11^{+0.07}_{-0.06}$	$\sim 1.5 \times 10^{34}$	140^{+20}_{-10}	2.5	0.3–10.0	La Palombara and Mereghetti (2006)
X Persei	839.3 ± 0.3	1.35 ± 0.03	$\sim 1.4 \times 10^{35}$	361 ± 3	1	0.3–10.0	La Palombara and Mereghetti (2007)
	~ 837	1.45 ± 0.02	$\sim 4.2 \times 10^{34}$	130	0.95	3.0-10.0	Coburn *et al.* (2001)
RX J1037.5-5647	853.4 ± 0.2	$1.26^{+0.16}_{-0.09}$	$\sim 1.2 \times 10^{34}$	130^{+10}_{-20}	5	0.2–10.0	La Palombara *et al.* (2009)
RX J0440.9+4431	204.96 ± 0.02	1.34 ± 0.04	$\sim 8 \times 10^{34}$	270 ± 20	3.3	0.3–12.0	La Palombara *et al.* (2012)
SXP 1062	~ 1062	1.54 ± 0.16	$6.3^{+0.7}_{-0.8} \times 10^{35}$	900^{+300}_{-200}	6	0.2–12.0	Hénault-Brunet *et al.* (2012)
4U 2206+54	5593 ± 10	1.63 ± 0.03	$\sim 3 \times 10^{35}$	370 ± 40	2.6	0.2–12.0	Reig *et al.* (2012)
Swift J045106.8-694803	168.5 ± 0.2	$1.8^{+0.2}_{-0.3}$	$(9.8 \pm 0.9) \times 10^{35}$	500 ± 200	50.6 ± 2.1	0.2–10.0	this work

2.2 Observations and Data Reduction

2.2.1 Optical

Optical spectra of Swift J045106.8-694803 have been taken on three separate occasions. Blue and Red end spectra were taken with the ESO Faint Object Spectrograph (EFOSC2) mounted at the Nasmyth B focus of the 3.6m New Technology Telescope (NTT), La Silla, Chile on the nights of 2011 December 8 and 10 respectively. The EFOSC2 detector (CCD#40) is a Loral/Lesser, Thinned, AR coated, UV flooded, multi-pinned phase chip with 2048×2048 pixels corresponding to 4.1 arcmin×4.1 arcmin on the sky. The instrument was in longslit mode with a slit width of 1.5 arcsec. Grism 14 has a wavelength range of $\lambda\lambda$3095–5085 Å and a grating of 600 lines mm^{-1} and a dispersion of 1 Å pixel^{-1}. Grism 20 is one of the two new Volume-Phase Holographic grisms recently added to EFOSC2. It has a smaller wavelength range, from 6047–7147 Å, but a superior dispersion of 0.55 Å pixel^{-1} and 1070 lines pixel^{-1}. Filter OG530 was used to block second order effects. The resulting spectra have spectral resolutions $\sim$ 10 Å and $\sim$ 6 Å respectively. Red end spectra were also taken with the 1.9m Radcliffe telescope at the South African Astronomical Observatory (SAAO) on 2009 December 12 and 2011 September 26. The data were obtained using the unit spectrograph combined with a 1200 lines mm^{-1} grating and the SITe detector at the Cassegrain focus. The resulting spectra have a spectral resolution of $\sim$ 3 Å.

The data were reduced using the standard packages available in the Image Reduction and Analysis Facility (IRAF). Comparison copper neon spectra (SAAO) and helium argon spectra (ESO) were taken throughout the observing runs with the same instrument configuration and used for wavelength calibration. The spectra were normalised to remove the continuum and a redshift correction applied corresponding to a recession velocity of -280 km s^{-1} (Paturel *et al.*, 2002).

2.2.2 X-ray

A $\sim$7 ks *XMM-Newton* target of opportunity (ToO) observation was performed during satellite revolution #2308 on July 17, 2012. Data from the European Photon Imaging Cameras (EPIC) were processed using the *XMM-Newton* Science Analysis System v11.0 (SAS) along with software packages from FTOOLS v6.12. Table 2.2 summarises the details of the EPIC observations.

The MOS (Turner *et al.*, 2001) and pn (Strüder *et al.*, 2001) observational data files were processed with emproc and epproc respectively. The data were screened

Table 2.2: *XMM-Newton* EPIC observations of Swift J045106.8-694803 on 2012 July 17

Camera	Filter	Read out Mode	Observation			Exp. (ks)
			Date (MJD)	Start(UT)	End(UT)	
MOS1/2	Medium	Full Frame	56125.0	00:39	03:03	8.6
pn	Medium	Full Frame		01:01	02:59	7.0

for periods of high background flaring activity by examining the count rate of the high energy (>10 keV) single pixel pattern (PATTERN=0) events. The files were examined by eye to confirm that the source does not contribute significantly to this energy range. Flares in these events are indicative of soft proton flaring events caused by magnetic reconnection. The pn and MOS count rates were below the recommended filtering threshold for the duration of the observation and so no filter was applied.

The final cleaned pn image included "single" and "double" (PATTERN≤4) pixel event patterns in the 0.2–10.0 keV energy range. "Single" to "quadruple " (PATTERN≤12) pixel events were selected for the cleaned MOS images in the same energy range. These pixel patterns are isolated and compact with the pixel with the highest charge at the centre, as such they are considered good X-ray events (i.e. genuine X-rays rather than cosmic rays) and are fully calibrated. Larger patterns are thought to be due to cosmic rays. The default quality flags #XMMEA_EM (for the MOS) and #XMMEA_EP (for the pn) were employed. Photon arrival times were converted to barycentric dynamical time, centred at the solar system barycenter, using the SAS task barycen.

Images, background maps and exposure maps were created for all detectors in the 0.2–10.0 keV energy range. A box sliding detection was performed simultaneously on all 3 images twice (the first with a locally estimated background the second using the background map) with the task eboxdetect, followed by the maximum likelihood fitting using the task emldetect. This process resulted in a list of sources including their positions, errors and background subtracted counts. A much more in depth account of the steps involved in the detection of sources is given in Section 4.2.1.

Source counts were extracted from a circular region with radius 61 arcsec, as recommended by the SAS task eregionanalyse which calculates the optimal radius for the source extraction by maximising the signal to noise. Background counts were extracted from a region of identical size offset from the source, with a similar

"RAWY" co-ordinate (i.e. is a similar distance to the readout node as the source region, as recommended by the "EPIC status of calibration and data analysis" document[1]). The is because the detector background variation on both the MOS and pn charge coupled devices (CCDs) is larger in this direction. Annular background regions around the source were not used to avoid any "out-of-time" events (events registered during the readout of a CCD that are assigned the incorrect RAWY values). The background subtraction was performed using the epiclccorr task which also corrects for bad pixels, vignetting and quantum efficiency.

Source and background spectra were extracted from the same regions described above. Again, "single" and "double" pixel events (PATTERN$\leq$4) were accepted for the pn detector with all bad pixels and columns disregarded (FLAG=0). For the MOS spectra, "single" to "quadruple "(PATTERN$\leq$12) pixel events were selected with quality flag #XMMEA_EM. The area of source and background regions were calculated using the backscal task. Response matrix files were created for each source using the task rmfgen and arfgen.

2.3 Analysis and Results

2.3.1 Spectral Classification

OB stars in the Milky Way are classified using certain metal and helium line ratios (Walborn and Fitzpatrick, 1990) based on the Morgan-Keenan (MK; Morgan *et al.* 1943) system. However, this is unsuitable in lower metallicity environments as the metal lines are either much weaker or not present. As such, the optical spectrum of Swift J045106.8-694803 was classified using the method developed by Lennon (1997) for B-type stars in the SMC and implemented for the SMC, LMC and Galaxy by Evans *et al.* (2004, 2006).

Figure 2.1 shows the unsmoothed optical spectrum of Swift J045106.8-694803. The spectrum is dominated by the hydrogen Balmer series and neutral helium lines. There does appear to be evidence for the HeII λ4200Å line, but it is difficult to distinguish above the noise level along with the HeII $\lambda\lambda$4541, 4686Å lines. The HeI λ4143Å line is clearly stronger than the HeII λ4200Å line constraining the optical counterpart of Swift J045106.8-694803 to be later than type O9. There also appears to be evidence for the SiIV $\lambda\lambda$4088, 4116Å lines necessary for a B1 classification. This is supported by the relative strengths of the SiIII λ4553 and MgII λ4481Å suggesting a classification of B2 or earlier.

[1] http://xmm2.esac.esa.int/docs/documents/CAL-TN-0018.pdf

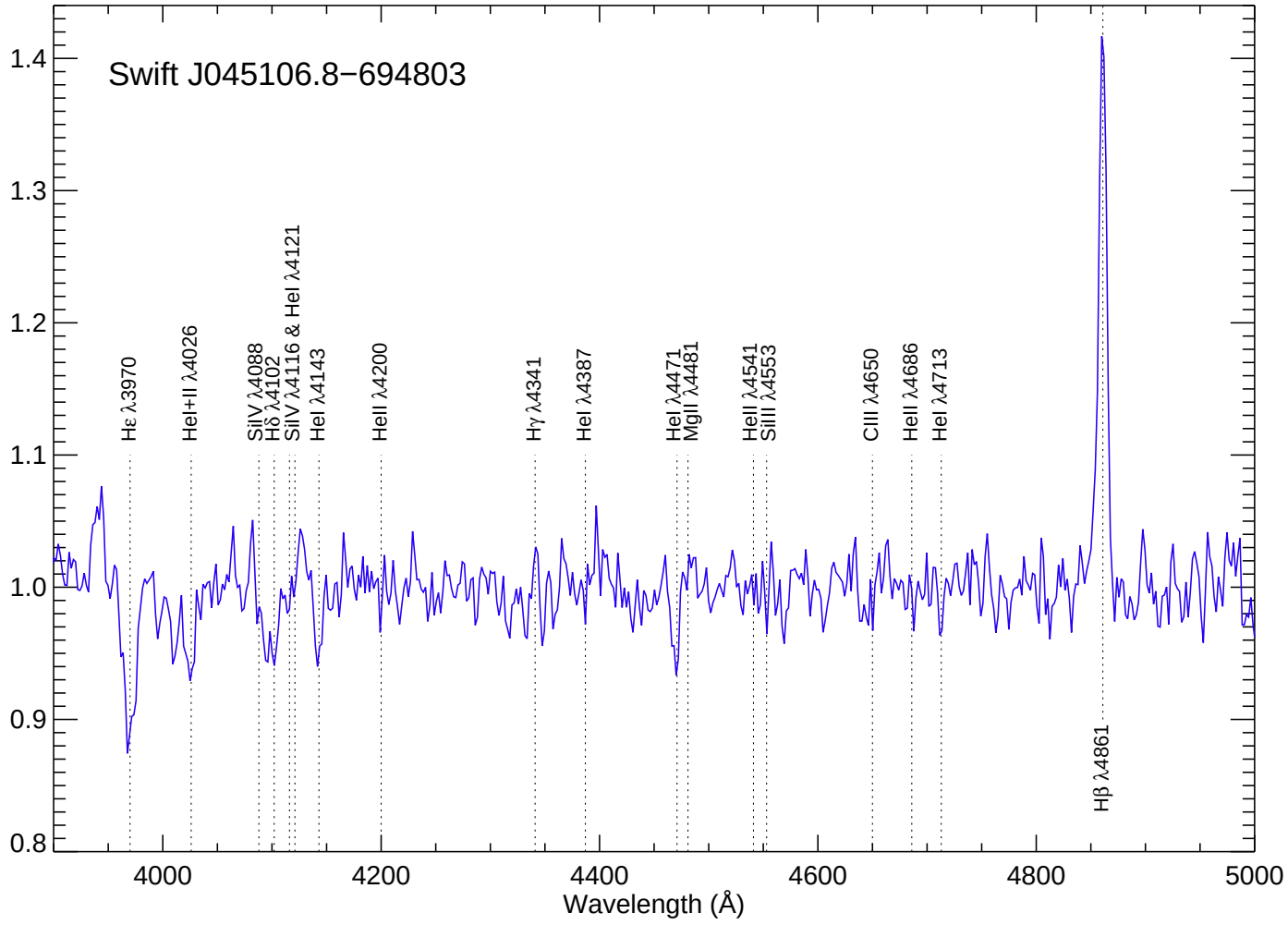

Figure 2.1: Spectrum of Swift J045106.8-694803 in the wavelength range $\lambda\lambda$3900–5000Å with the NTT on 2011-12-08. The spectrum has been normalised to set the continuum to unity and redshift corrected by -280 km s^{-1}. Atomic transitions relevant to spectral classification have been marked.

The luminosity class of the companion star was determined by the ratios of SiV λ4088/HeI $\lambda\lambda$4026 – 4121Å, SiV λ4116/HeI λ4121 and HeII λ4686/HeI λ4713. The first two ratios strengthen with decreasing luminosity class (i.e. with increasing luminosity) whereas the latter ratio decreases with increasing luminosity. The relative strengths of these lines are contradictory: The HeII λ4686/HeI λ4713 and SiV λ4116/HeI λ4121 suggest a luminosity class III, although the proximity of the rotationally broadened Hδ λ4102Å to the SiIV lines makes this more complex. The SiV λ4088/HeI λ4026 ratio is more consistent with a star of luminosity class V. The *V* band magnitude of this star is reported by several sources as between 14.6 and 14.7 (e.g. Massey 2002; Zaritsky *et al.* 2004). A distance to the LMC of 50.6$\pm$2.1 kpc along with an m_V of 14.65$\pm$0.05 and an extinction, A_V=0.45$\pm$0.5 (calculated using the column density towards the source, $8.42 \pm 1.03 \times 10^{20}$ cm^{-2} and the results of Güver and Özel 2009) would correspond to an M_V of -4.2$\pm$0.1. This is consistent with B0.5III (Wegner, 2006). Less information is available for the absolute magnitude of emission line stars, which will be dependent on the inclination and size of the disc. As such I classify the optical counterpart of Swift J045106.8-694803 as a B0-1 III-V star.

Figure 2.2 shows the three red end spectra of Swift J045106.8-694803 taken two years apart. The ESO (top) spectrum is offset by 6 flux units. The Hα equivalent width, considered an indicator for circumstellar disk size, is remarkably similar in all three spectra increasing from -29$\pm$2 Å for the SAAO spectrum taken in 2009 to -33$\pm$1 Å and -34.5$\pm$0.6 Å for the SAAO and ESO spectra taken in 2011. It is not uncommon to see large variations in the Hα equivalent width of these systems on timescales of months. This apparent consistency in the equivalent width (and hence the disk size) is almost certainly linked to the X-ray activity of the source - which has also been remarkably consistent since its detection.

2.3.2 X-rays

2.3.2.1 Position

The simultaneous source detection performed on the three EPIC cameras determined the position of Swift J045106.8-694803 as RA(J2000)=$04^h51^m06.7^s$ Dec(J2000)=$-69°48'04.2"$. The 1σ systematic uncertainty was assumed to be 1 arcsec in accordance with the findings of the *XMM-Newton* Serendipitous Source catalogue (Watson *et al.*, 2009). This is an order of magnitude larger than the statistical error derived in the source detection, and as such is the dominant error on the

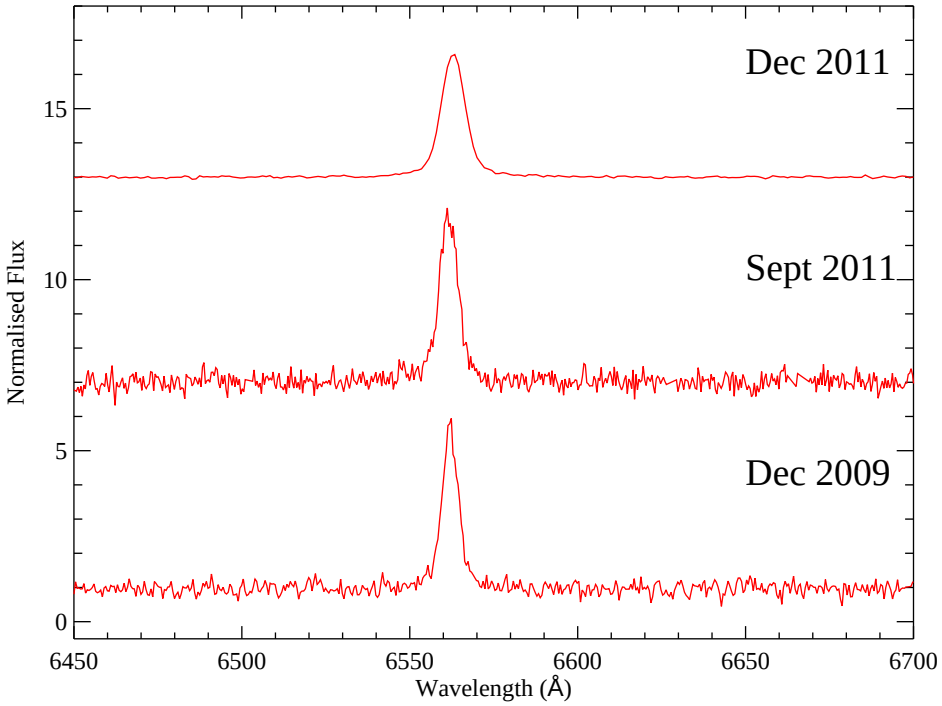

Figure 2.2: ESO and SAAO spectra of Swift J045106.8-694803 in the wavelength range $\lambda\lambda$6400–6700Å taken on 2011-12-10, 2011-09-26 and 2009-12-12 respectively. Spectra have been normalized to remove the continuum and shifted by -280 km s^{-1}

position. This position is consistent with the *Swift* positions reported by Beardmore *et al.* (2009) and Klus *et al.* (2013) confirming that these three detections are the same source. Figure 2.3 shows a *V*-band image with the location of the *Swift* and *XMM-Newton* positions with radii equal to the 1σ errors.

2.3.2.2 Timing Analysis

Figure 2.4 shows the light curve of Swift J045106.8-694803. The bottom panel shows the Lomb-Scargle periodogram of the 20 s bin light curve. A sine wave with the detected period was fit to the 20 s bin light curve and is overlaid for clarity. A period at 168.8 s with a power of 46.1 was detected, rising to 82.7 when the bin size of the light curve is reduced to 0.1 s. Monte Carlo simulations with both red and white noise light curves were performed to determine the significance of this detection. A bin time of 20 s was also employed for the simulations to reduce the processing time. One million white noise light curves were generated by "scrambling" the original light curve (i.e. reassigning the flux values to different time stamps) using

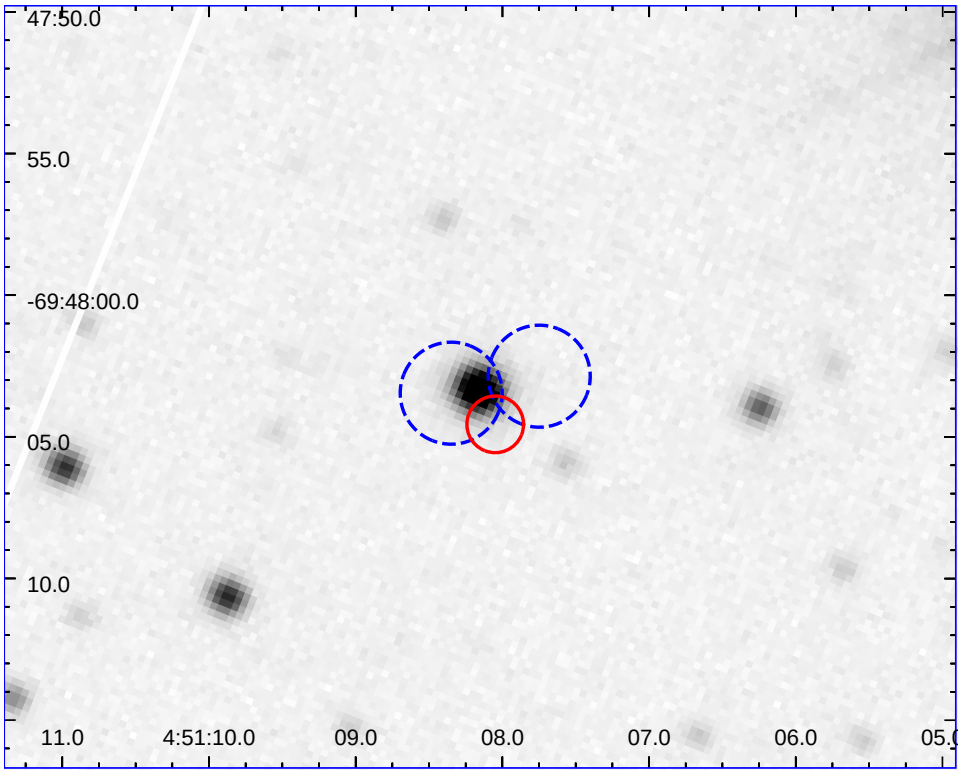

Figure 2.3: *XMM-Newton* (solid red) and *Swift* (broken blue) 1σ error circles for Swift J045106.8-694803.

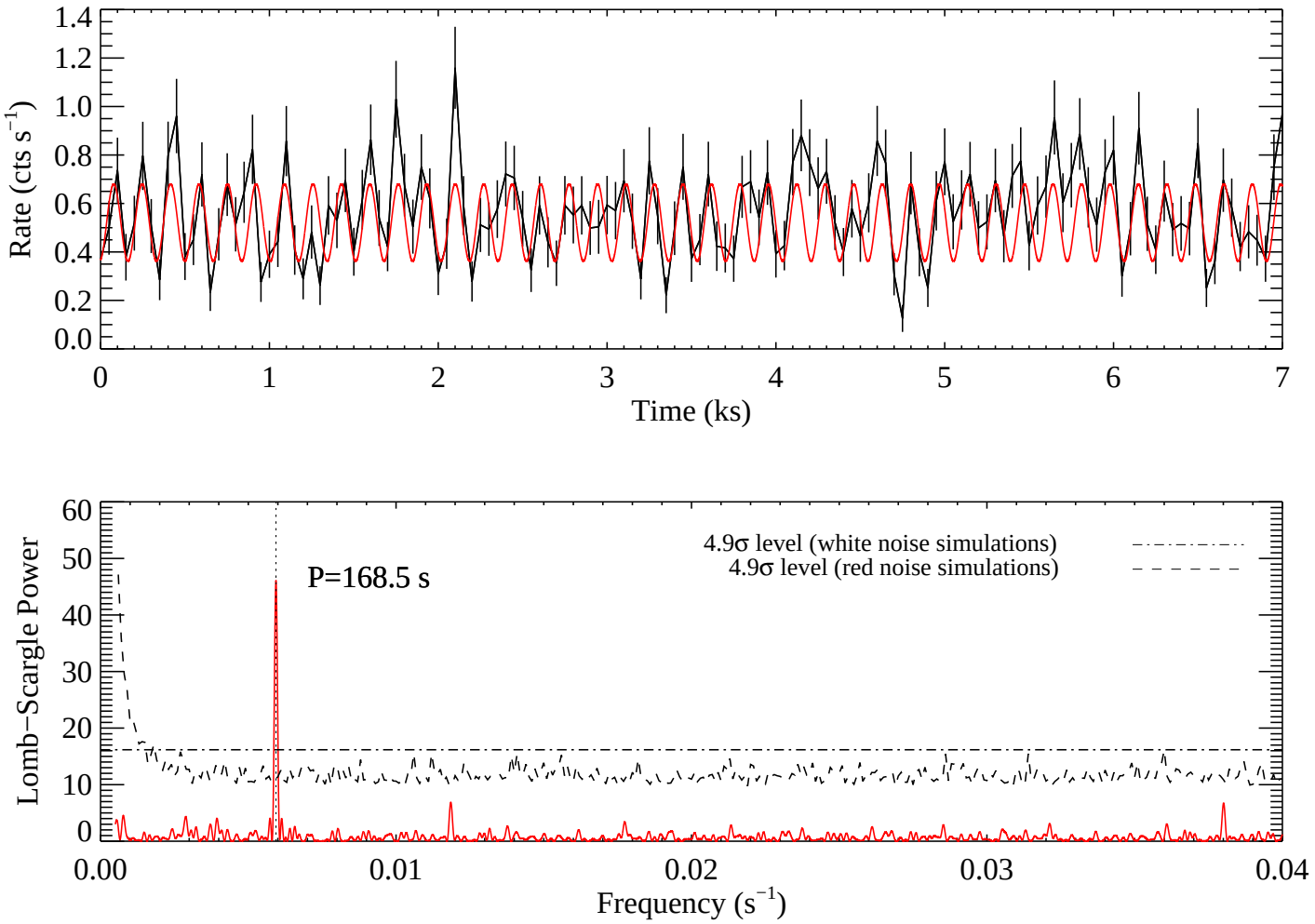

Figure 2.4: Top panel shows the EPIC pn light curve of Swift J045106.8-694803 with 50 s bins. Bottom panel shows the Lomb-Scargle periodogram with the detected period marked along with the 99.9999% significance levels determined by white and red noise simulations.

a random number generator. This method makes no assumption about the underlying distribution of the light curve. Lomb-Scargle analysis was performed on each of these light curves and the highest power recorded. None of the 1,000,000 light curves generated produced a peak in the periodogram greater than 17.0. This suggests that the period discovered in the light curve has a significance $>$99.9999% or 4.9σ.

One million light curves were generated with a power law slope of -2.0 and the same statistical properties (mean, standard deviation and bin time) as the EPIC-pn light curve, using the method of Timmer and Koenig (1995)[2]. The light curves were initially simulated with a duration ten times longer than that of the actual data and were then cut down to the observed duration to minimise the effect of red noise leakage. Gaussian noise was added to each point of this new light curve by drawing a random deviate from a Gaussian distribution with mean and variance equal to each data point following the method detailed by Uttley *et al.* (2003). Any bins with a negative count rate were set to zero. Lomb-Scargle analysis was performed on each of the simulated time series. Unlike the white noise simulations, the significance of a peak depends on the frequency. The broken line in Fig 2.4 shows the 99.9999% significance contour. Both the white and red noise simulations indicate that this period is significant.

The error in the period was estimated by varying the original light curve within the errors on each data point, using a Gaussian random number generator, 10,000 times. As with the simulations to determine the significance of the detection, Lomb-Scargle analysis was performed on each of these light curves. To speed up the processing time of the simulation, the light curve was only searched for periods between 50 s and 2000 s. The resulting histogram is well fit by a Gaussian with mean 168.5 s and a standard deviation of 0.16 s. As such I determine the period of Swift J045106.8-694803 to be 168.5 ± 0.2 as of MJD = 56125.0.

Light curves were generated for four energy ranges, 0.2-1.0 keV, 1.0-2.0 keV, 2.0-4.5 keV and 4.5-10.0 keV with approximately equal count rates (0.12, 0.18, 0.17 and 0.13 counts s^{-1} respectively). Figure 2.5 shows the pulse profiles for each of these light curves and the entire 0.2-10.0 keV light curve, each normalised to the average count rate in the energy range. The zero phase point was determined from the phase shift found from the sine wave fit to the 0.2-10.0 keV light curve (see above). Lomb-Scargle analysis was performed on each of the light curves.

The strongest detection of the period in a single band is in the 1.0-2.0 keV energy

[2] rndpwrlc.pro

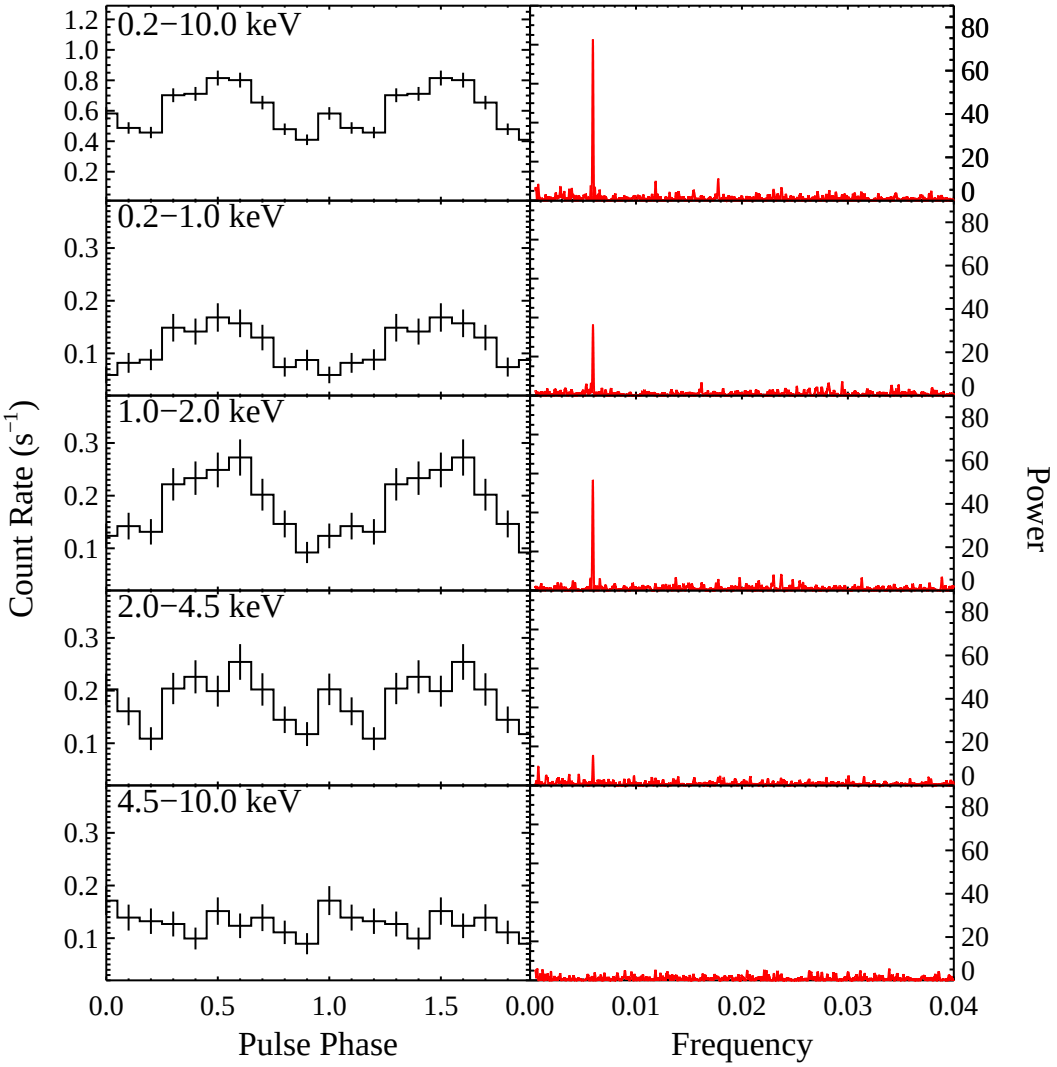

Figure 2.5: Left panels show the background subtracted pulse profiles from the EPIC-pn detector, folded on the 168.5 s period detected. Right panels show the Lomb-Scargle periodogram in the same energy range.

range, with a Lomb-Scargle power of 56.7. This does not appear to be an issue relating to photon counting statistics, as the period is barely detected in the 2.0-4.5 keV energy range (Lomb-Scargle power of 15.2) which has an almost identical average count rate. The strongest period identified in the 4.5-10.0 keV energy range was at 11.3 s with a Lomb-Scargle power of 7.8, this is likely to be noise rather than the detection of a second period.

I investigated whether the fall off in the detection strength could be due to a change in the shape of the pulse profile, as Lomb-Scargle analysis is more sensitive to sinusoidal variations. I checked for periods using the epoch folding methods of Leahy (1987). The lightcurve is folded on each trial period and tested to see if it is consistent with a constant count rate with a χ^2 test. This reinforces the results from

Table 2.3: Summary of timing results

Energy	Lomb-Scargle	Pulsed Fraction	
Range (keV)	Power	P=168.5 s	P=84.3 s
0.2-10.0	82.7	0.43±0.03	-
0.2-1.0	36.1	0.42±0.07	-
1.0-2.0	56.7	0.47±0.05	-
2.0-4.5	15.2	0.34±0.05	0.13±0.06
4.5-10.0	-	0.08±0.06	0.14±0.06

the Lomb-Scargle analysis, with the strongest detection in the 1.0-2.0 keV range and no detection in the 4.5-10.0 keV range. The first harmonic of the period was the strongest period identified in the 2.0-4.5 keV light curve, suggesting the pulsed profile may become double peaked at higher energies.

The pulsed fraction of each light curve was calculated by fitting a sine wave with the period fixed at the value found in the full 0.2-10.0 keV energy range. The phase, amplitude and the average value of the light curve were allowed to vary and the ratio of the amplitude and average value were taken. This is equivalent to taking the ratio of the difference of the maximum and minimum value of the sine wave with the sum of these values. This parameter can vary between 1 (completely pulsed) and 0 (constant rate). The values range from 0.47±0.05 for the 1.0-2.0 keV energy range down to 0.08±0.06 for the 4.5-10.0 keV range. As the epoch folding suggests that the profile becomes double peaked at higher energies, the fit was also performed with the period fixed at the second harmonic for the last two energy bands. The results are summarised in Table 2.3.

I split the light curves into two energy ranges, 0.2-2.0 keV and 2.0-10.0 keV, with equal count rates (0.293 ± 0.007 and 0.305 ± 0.007 respectively). The hardness ratio (HR) between the "soft" ($<$2 keV) and "hard" ($>$2 keV) light curves was calculated using the formula:

$$HR = \frac{C_{hard} - C_{soft}}{C_{hard} + C_{soft}} \tag{2.1}$$

where C_{hard} and C_{soft} are the count rates in the hard and soft bands respectively. The hardness ratio can vary between -1.0 (zero counts in the 2.0-10.0 keV band) and 1.0 (zero counts in the 0.2-2.0 keV band). Figure 2.6 shows how the hardness ratio varies with pulse phase. From a comparison with the left panels of Fig. 2.5, a clear anti-correlation between the hardness ratio and the pulse profile is evident, with the source getting harder with decreasing luminosity.

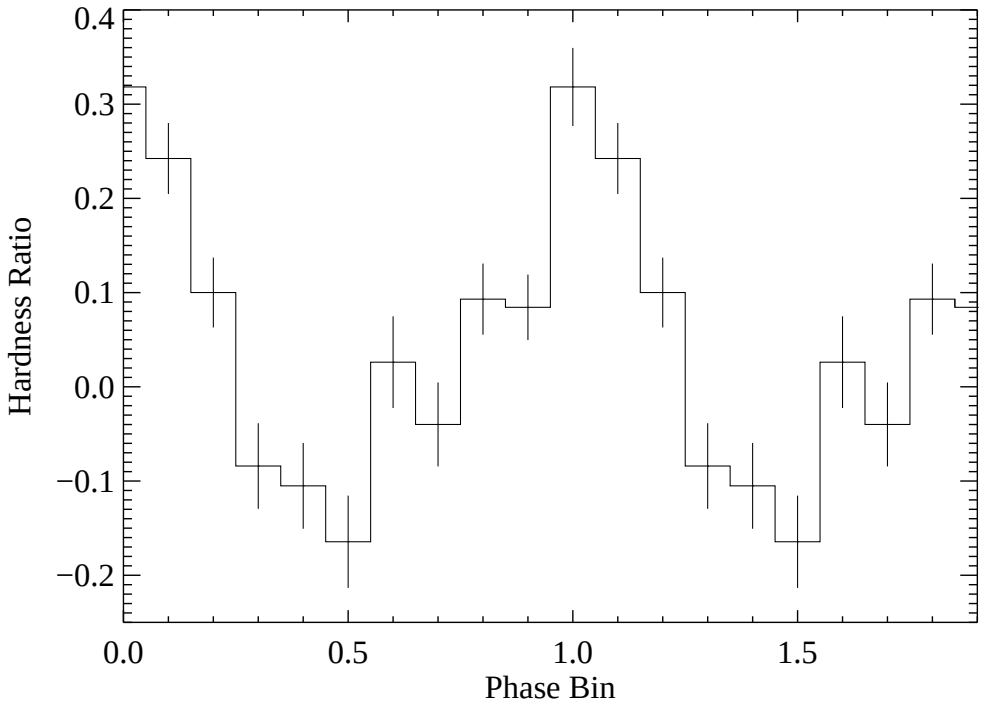

Figure 2.6: Hardness ratio, $\frac{C_{hard}-C_{soft}}{C_{hard}+C_{soft}}$, as a function of pulse phase. C_{soft} is the 0.2-2.0 keV count rate and C_{hard} is the 2.0-10.0 keV count rate. The phase shown is the same as that of the pulse profiles shown in Fig 2.5.

2.3.2.3 Spectral Analysis

The spectral analysis discussed here was performed using XSPEC (Arnaud, 1996) version 12.7.0. The three spectra from the different EPIC detectors were fit simultaneously with the models reported here plus an additional constant factor to account for the variations in the different detectors. The model parameters were constrained to be identical across the three instruments. The photoelectric absorption was split into two components. One, $N_{H,Gal}$, to account for the Galactic foreground extinction, fixed to 8.4×10^{20} cm^{-2} (Dickey and Lockman, 1990) with abundances from Wilms *et al.* (2000), and a separate column density, $N_{H,i}$, intrinsic to the LMC with abundances set to 0.5 for elements heavier than helium (Russell and Dopita, 1992) and allowed to vary. All errors stated in this section are the 90% confidence range.

The spectra obtained from the three instruments were initially fit with a simple absorbed power law model (*phabs*vphabs*powerlaw* in XSPEC, where *vphabs* is the photoelectric absorption with variable metal abundances, set by the user). This lead to an acceptable fit with a χ^2 of 270.5 for 236 degrees of freedom (dof) with a photon index of $\Gamma = 0.97 \pm 0.05$ and intrinsic absorption $N_{H,i} = (1.3 \pm 0.4) \times 10^{21}$ cm^{-2}.

Table 2.4: Best fit parameters for the spectral fits. In all three models the *phabs* component is fixed at 8.4×10^{20} cm^{-2} (Dickey and Lockman, 1990). Errors, where reported, are the 90% confidence level.

Model	$N_{H,i}$ [10^{21} cm^{-2}]	Γ	kT_{BB} [keV]	Flux$^{(a)}$ [10^{-12} erg cm^{-2} s^{-1}]	$L_X^{(b)}$ [10^{36} erg s^{-1}]	χ^2_r/dof
*phabs*vphabs*powerlaw*	1.3 ± 0.4	0.97 ± 0.05	-	$3.4^{+0.1}_{-0.2}$	1.03 ± 0.09	1.15/236
*phabs*vphabs*(bbody+powerlaw)*	$1.6^{+1.0}_{-0.8}$	$1.4^{+0.5}_{-0.3}$	$1.8^{+0.2}_{-0.3}$	$3.2^{+0.1}_{-0.2}$	0.98 ± 0.09	1.08/234
*phabs*vphabs*(diskbb+powerlaw)*	5^{+3}_{-5}	4^{+1}_{-4}	$4.2^{+1.0}_{-0.6}$	3.0 ± 0.1	0.92 ± 0.06	1.09/234

Notes. $^{(a)}$ Observed flux in the 0.2-10.0 keV range. $^{(b)}$ Source intrinsic luminosity in the 0.2-10.0 keV range, corrected for absorption and assuming a distance to the LMC of 50.6 kpc.

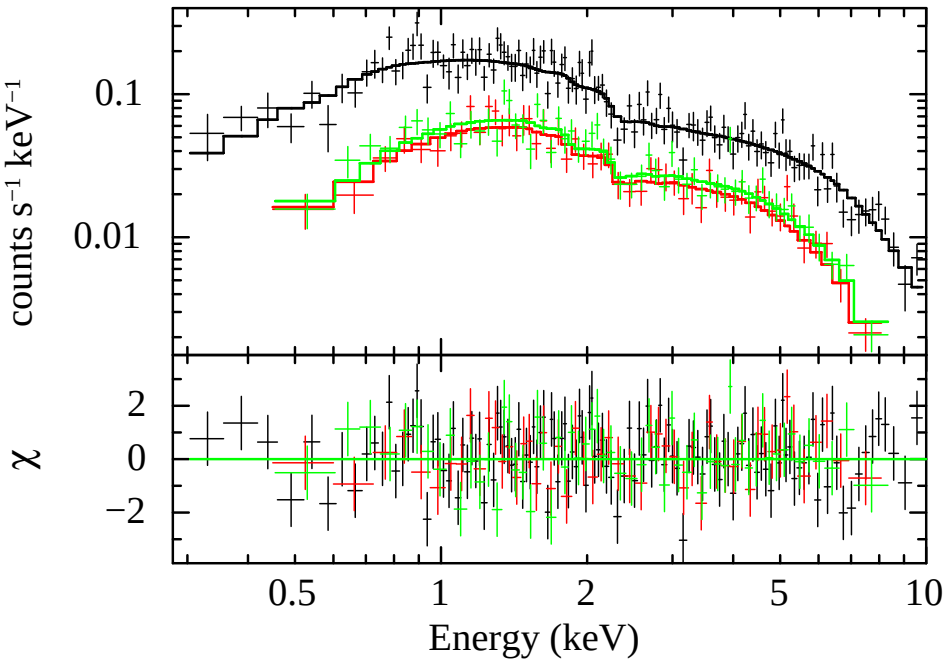

Figure 2.7: The 0.2–10.0 keV EPIC-pn (black), EPIC-MOS1 (red), EPIC-MOS2 (green) spectra of Swift J045106.8-694803. Top panel displays the background subtracted spectrum with best fit *phabs*vphabs(powerlaw+bbody)* model, bottom panel shows the residuals.

The photon index is typical for those seen in other Be/X-ray binaries, particularly in the SMC (Haberl *et al.*, 2008a).

The possibility of a thermal component was also explored and modelled by either a blackbody or diskbb model. Including these parameters improved the fit marginally (χ^2 of 252.8 and 255.7 for 234 dof respectively) but F-tests suggest that these are significant at 99.96% and 99.86% respectively (i.e. $>3\sigma$). Fig. 2.7 shows the 0.2–10.0 keV spectrum along with the best fit model (*phabs*vphabs(powerlaw+bbody)*). The parameters of all the models discussed here are included in Table 2.4. The best fit parameters for the *phabs*vphabs*(diskbb+powerlaw)* are both unphysical and poorly constrained (e.g. $\Gamma = 4^{+1}_{-4}$ is incredibly soft and $kT = 4.2^{+1.0}_{-0.6}$ is too hot for a disc, which have $kT \sim 0.1$), as such, only the results of the *phabs*vphabs*(bbody+powerlaw)* model are discussed in detail. The total unabsorbed flux from the blackbody component is $1.3 \pm 0.8 \times 10^{-12}$ erg cm^{-2} s^{-1}, accounting for approximately 40% of the total emission of the source.

An intrinsically narrow Gaussian was added to the model at 6.4 keV to see if any evidence for an Fe-Kα line exists. The upper limit on the equivalent width of this component was derived as 0.3 keV. Allowing the energy or width of this feature to vary does not alter this result, as such I conclude that there is no evidence for Fe-Kα emission in the X-ray spectrum of Swift J045106.8-694803.

2.3.3 Modelling the Phase Resolved Spectra and Pulse Profiles

The anticorrelation seen between the hardness ratio and pulse profile has previously been reported for another persistent BeXRB, RX J0146.9+6121 by La Palombara and Mereghetti (2006). Pulsed phased spectroscopy revealed that the change in spectra could be explained with a static blackbody and variable power law (among other solutions). This possibility was explored by generating 10,000 EPIC-pn spectra with the same absorption, photon index and blackbody temperature as the best fit model using the xspec command FAKEIT. These parameters were fixed as they are linked to the physical properties of the system and/or the local environment and so are unlikely to change on a timescale of seconds. The value of the normalisation for the power law and blackbody varied from zero to 5.0×10^{-4} in steps of 5.0×10^{-6}. The total number of counts as well as the hardness ratio were calculated for each of the simulated spectra. The results of the simulation were searched for the normalisation values which produced the same count rate and hardness ratio as the different phase bins in Fig. 2.6 within errors.

The results of the simulations, along with the pulse profile and hardness ratio, are shown in Fig. 2.8. Interestingly, a constant blackbody could not reproduce the range of hardness ratios seen. A modulation of the blackbody component $\sim \pi$ out of phase with that of the power law is required to reproduce the data. Figure 2.9 shows the simulated spectrum and model components of Swift J045106.8-694803 at the hardness ratio maximum (hardest) and minimum (softest). The pulsed fraction of the power law and blackbody components are consistent at 0.6 ± 0.2 and 0.7 ± 0.3 respectively.

Since the blackbody component varies with the rotation of the neutron star and can be inferred to have a small ($R < R_{NS}$) emitting size from L_X and KT_{BB}, it is possible that this region is a hot, magnetic polar cap on the neutron star surface. By adopting a model for the hot spot emission and fitting this model to the pulse profile, the geometry of the system can be constrained, in particular, the angle between the rotation and magnetic axis α and the angle between the rotation axis and line-of-sight ζ.

Proper modelling requires detailed knowledge of the magnetic field and temperature distributions over the neutron star surface and is beyond the scope of this work (see, e.g., Ho 2007). Nevertheless useful insights can still be easily obtained using a simple model: two antipodal hot spots that emit as a blackbody and have a beam pattern (i.e., angular dependence) which is isotropic and has no energy-dependence. For each (α, ζ), the pulse profile is calculated using the analytic approximation of

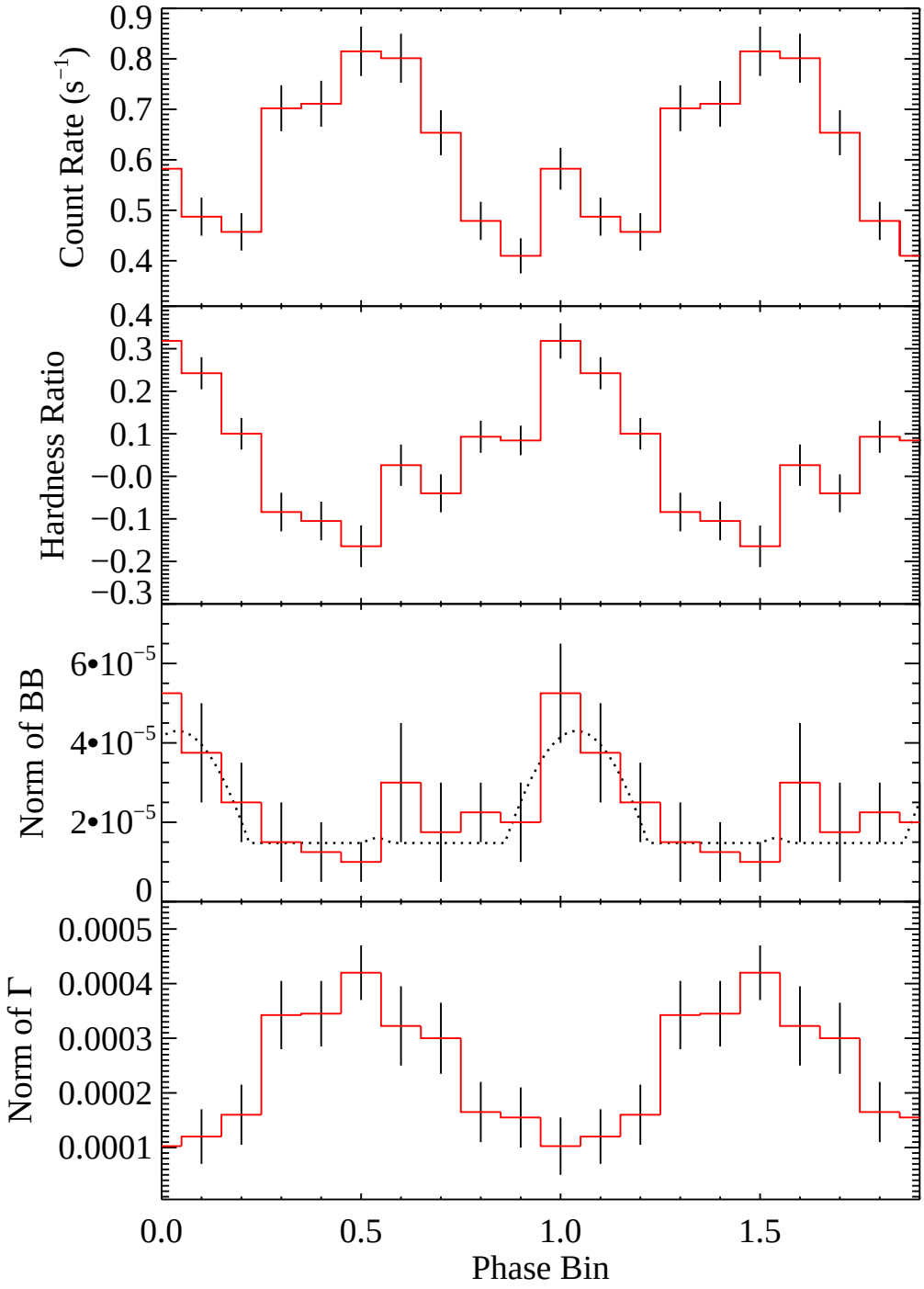

Figure 2.8: Panels from top to bottom show (1) 0.2-10.0 keV pulse profile (2) Hardness ratio (3) The normalisation of the blackbody (BB) required to produce the hardness ratio and count rate of the given phase bin and (4) The normalisation of the power law (Γ) required for the given phase bin. The broken line in panel (3) is the best-fit pulse profile (see text)

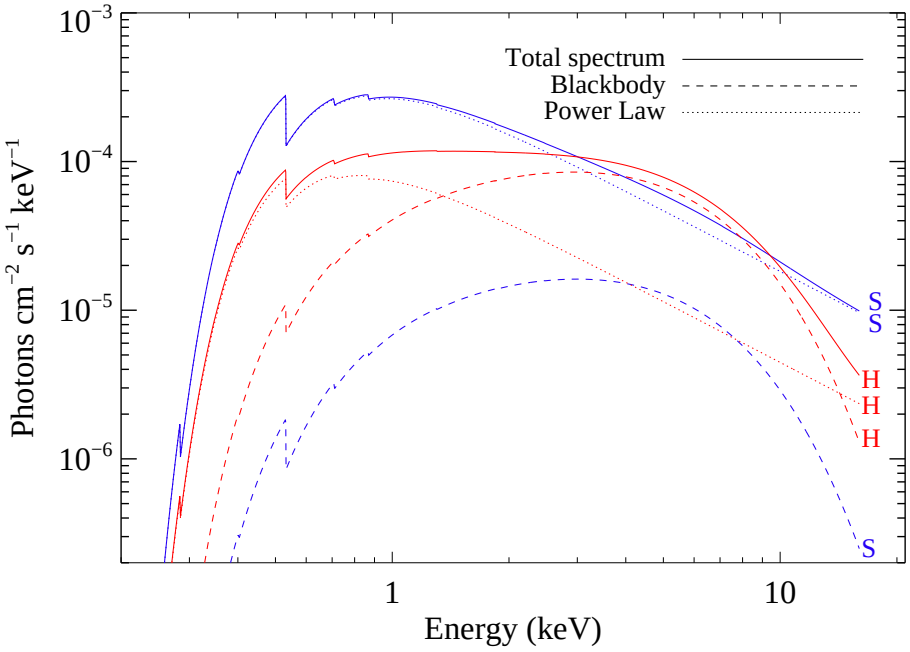

Figure 2.9: Figure shows the ”hardest” (red) and ”softest” (blue) states of the spectrum, according to the simulations, and the model components.

Beloborodov (2002) to the exact relation given in Pechenick *et al.* (1983) which accounts for gravitational light-bending. The pulse profiles are degenerate in the two angles, i.e., (α,ζ) and (ζ,α) produce the same profile. A neutron star mass $M_{\rm NS} = 1.4\,M_{\odot}$ and radius $R_{\rm NS} = 12$ km are assumed. These model pulse profiles are then fit to the blackbody pulse profile (see panel (3) of Fig. 2.8), allowing the phase and amplitude to vary. Shaded regions for χ^2_r (for 8 degrees of freedom) values are shown in Fig. 2.10, the crosses indicate the best-fit values.

For this emission model, the $\alpha-\zeta$ parameter space can be divided into four regions which correspond to four classes defined in Beloborodov (2002) (see Figure 2.11): Class I is where one pole is visible all the time, the second pole never, class II is where one pole is visible all the time and the second pole some of the time, class III is where both spots are seen some of the time and class IV is where both spots are always seen. A geometry in class IV is immediately ruled out as it requires the blackbody flux to be constant. Similarly, the out of phase pulsations of the power law (interpreted as the accretion column) and the blackbody suggests I can also rule rule out a geometry in class I, if the accretion column is located just above the neutron star surface since it will always be eclipsed by the neutron star. The results from the fitting suggest that both of the neutron star poles are visible during a rotation of the neutron star, with best-fit values for the angles of 53° and 70°.

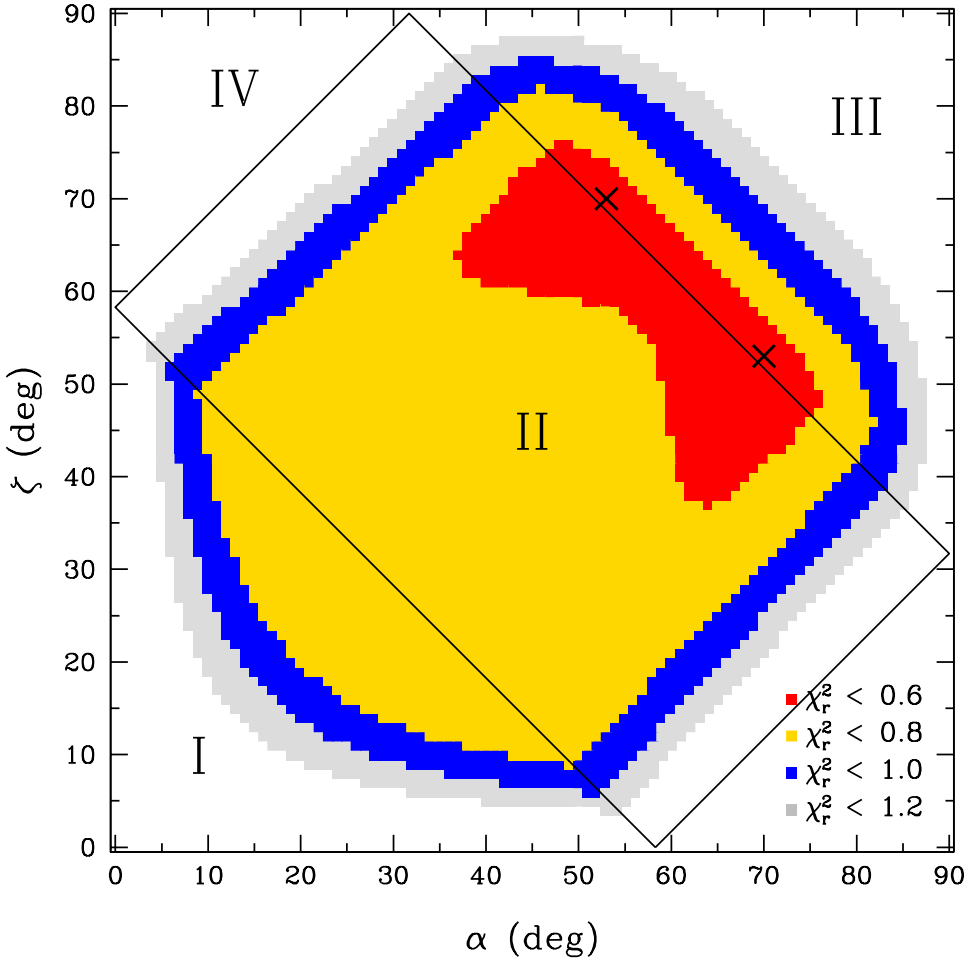

Figure 2.10: χ^2_r contours of the fit to the blackbody pulse profile for the angle between rotation and magnetic axes, α, and angle between rotation axis and line-of-sight, ζ. Crosses indicate the best-fit values. The four classes (I–IV) are defined in the text.

2.4 Discussion

A soft excess is a common feature in the X-ray spectra of HMXBs. It is hypothesised that a soft excess is in fact present in all HMXB spectra, though not always detected due to the high intrinsic absorption and flux of some sources. For systems with $L_X \gtrsim 10^{38}$ erg s^{-1}, this excess is thought to originate from the inner radius of an accretion disc surrounding the neutron star. For less luminous sources ($L_X \lesssim 10^{36}$ erg s^{-1}), the soft excess is attributed to other processes, e.g. thermal emission from the neutron star's surface (Hickox *et al.*, 2004).

The temperature and flux of the blackbody component detected in this observation of Swift J045106.8-694803 ($kT_{BB} = 1.8^{+0.2}_{-0.3}$ keV, $f_{X,BB} = 1.3 \pm 0.8 \times 10^{-12}$ erg cm^{-2} s^{-1}) along with a distance to the LMC of 50.6 ± 2.1 kpc (Bonanos *et al.*, 2011) implies an

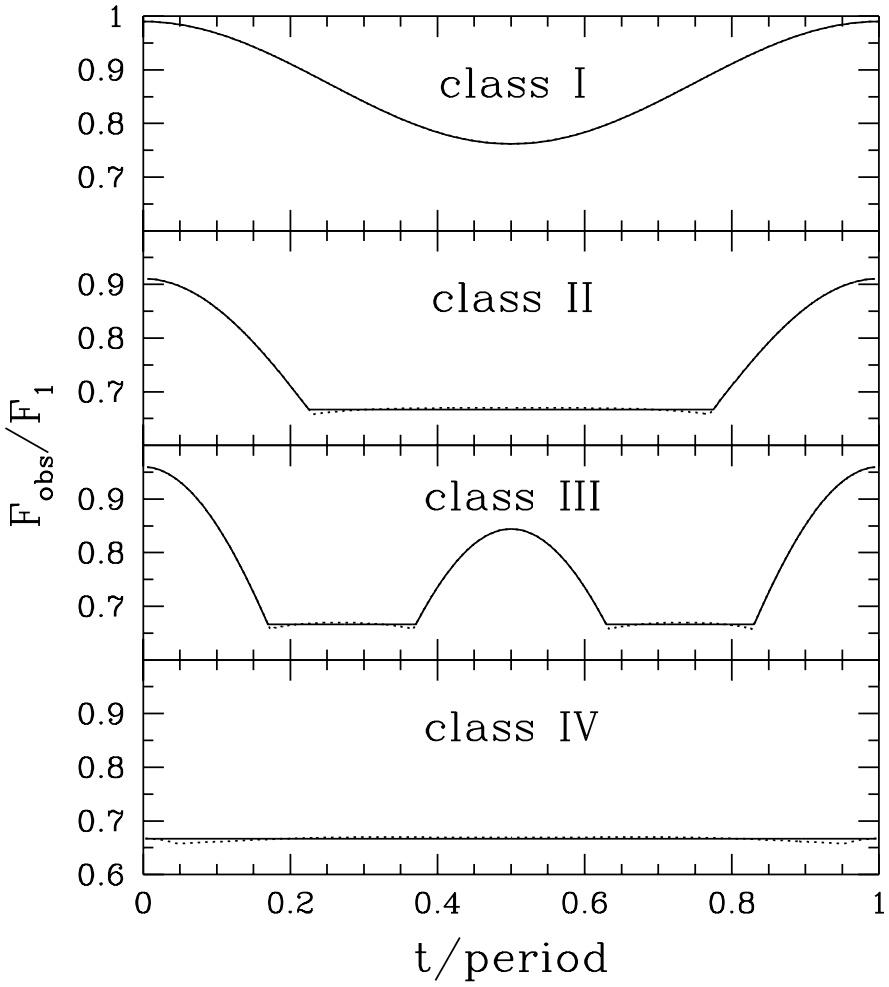

Figure 2.11: Blackbody pulse profiles for classes I-IV. (Taken from Beloborodov (2002))

X-ray luminosity $9.8 \pm 0.9 \times 10^{35}$ erg s^{-1} and blackbody radius of R_{BB}=0.5±0.2 km. This is calculated using the formula $R_{BB} = \sqrt{L_X/(4\pi\sigma T^4)}$ with all errors representing the 90% **confidence** limits. The radius is substantially less than that of a neutron star and, along with the low luminosity of $9.8 \pm 0.9 \times 10^{35}$ erg s^{-1}, rules out emission from the accretion disc as the origin of the excess.

In the last 10 years a subset of BeXRBs have been discovered which are reported to have a "hot" ($kT_{BB} > 1$ keV) thermal excess (see Table 2.1). These all have $R_{BB} \lesssim 1$ km, suggesting emission from the neutron star polar cap. These systems are characterised by long pulse periods (P>100 s) and persistent, low level X-ray emission, much like Swift J045106.8-694803. Could this be a selection effect? The ability to detect pulsations in a given observation decreases with increasing pulse period. This could lead to pulsars with longer pulse periods being observed for longer and thus having **a** greater number of counts in the source spectrum. This in

turn would allow fainter spectral components to be detected. However, there are several pulsars with both short and long periods that have been observed with a similar or greater number of total counts than seen here which have not shown any evidence for this spectral component (see Haberl *et al.* 2008a, Sturm *et al.* 2012b and Townsend *et al.* 2011, for recent examples with *XMM-Newton*). As such I conclude that this cannot be an observational bias.

Thermal emission is often assumed to have the greatest contribution to the soft band - the simulations show that this is not the case here. The blackbody component contributes the greatest proportion of the flux at energies $\gtrsim 4.0$ keV. If the thermal excess originates from the polar cap, then intuitively one would expect it to be pulsed. The results of the simulations performed seem to suggest that this is indeed the case. Despite similar levels of variation in both components in the hardness ratio minimum and maximum spectra (see Fig. 2.9), the overall spectrum varies very little above ~ 3 keV. This reflects the results of the Lomb-Scargle analysis of the higher energy light curves, which lack strong evidence for pulsations. It also explains the reduction in the pulsed fraction at higher energies, which is usually observed to increase with both increasing energy and decreasing source flux as the regions emitting the X-rays become more compact (Lutovinov and Tsygankov, 2008). Above 10 keV, the dominant component in the X-ray spectrum is once again the power law component. If the blackbody component is truly present then pulsations should once more be detectable at higher energies.

The decomposition of the spectral components has allowed the geometry of the neutron star to be constrained. The constraints are approximate since I assumed a simple blackbody emission model. More sophisticated modelling is not warranted at this time given the relatively large uncertainties on the pulse profile. Detailed modelling of deeper observations, with better signal-to-noise, could provide an independent measurement of the magnetic field; furthermore, future polarization studies could even break the degeneracy between α and ζ.

Klus *et al.* (2013) use the pulse period determined in this work along with data from *Swift* and *RXTE* to show that Swift J045106.8-694803 has a magnetic field above the quantum critical value. Two other "accreting magnetar" candidates (i.e. accreting neutrons stars with $B > B_{crit}$) are currently known, 4U2206+54 (Reig *et al.*, 2012) and SXP 1062 (Popov and Turolla, 2012; Hénault-Brunet *et al.*, 2012). Intriguingly, both of these sources are members of the hot thermal excess population (see Table 2.1) which suggests a possible link between these phenomena (although SXP 1062 is also surrounded by a supernova remnant with $kT_{BB} = 0.23 \pm 0.05$ keV possibly adding to the thermal excess, Haberl *et al.* 2012b). However, not all of the

sources listed in Table 2.1 have the large $\dot{P}$ indicative of a strong magnetic field, indicating that the hot thermal excess could be necessary but not sufficient evidence for a strong magnetic field.

2.5 Conclusion

I have presented detailed analysis of a recent *XMM-Newton* ToO observation of the HMXB Swift J045106.8-694803. I have classified the optical counterpart to this system as a B0-1III-V star, establishing this source as a BeXRB. The period was determined to be 168.5±0.2 s as of MJD = 56125.0. The detection strength of the pulsations decreases with increasing energy, with no detection of the period at energies >4.5 keV. The X-ray spectrum is adequately represented by two models, a single component continuum model (an absorbed powerlaw) and a two component continuum model (an absorbed powerlaw and blackbody). The extra blackbody component, though just formally significant, is not necessary for an acceptable fit to the spectrum and the parameters of the *phabs*vphabs*powerlaw* model are consistent with those reported for other BeXRBs. However, it is difficult to explain the dramatic decrease in the pulsations with increasing energy with a single component model. A two component model, with anticorrelated pulsations, can account for this behaviour and the anticorrelation of the hardness ratio and pulse profile and implies α and ζ values of 53° and 70°.

The high temperature of the blackbody ($kT_{BB} = 1.8^{+0.2}_{-0.3}$ keV) implies a radius of blackbody radius of $R_{BB} = 0.5 \pm 0.2$ km, and is attributed to emission from the polar cap of the neutron star. This is not the first detection of a hot thermal excess in the X-ray spectra of HMXBs (see Table 2.1 for recent examples) and interestingly Swift J045106.8-694803 shares common characteristics with these sources including persistent low level X-ray emission and a long pulse period (P>100 s). If confirmed to be the latest member of this emerging class, it would be the brightest and shortest period source.

Two of the other sources listed in Table 2.1 also have high $\dot{P}$ values, indicating a strong magnetic field. Whilst based on a small sample, this could suggest that there is a link between a hot thermal excess and the magnetic field strength. Further monitoring of the pulse periods of these sources as well as the temperatures of their thermal components could reveal if this is causal or coincidence. If our analysis is correct, I predict that above 10 keV the pulse period should once more be detectable as the power law becomes the dominant component in the X-ray spectrum once

again.

Most of the known X-ray pulsars in the Small and Large Magellanic Clouds have been detected with *RXTE* during a $\sim$10 yr monitoring campain (Galache *et al.*, 2008). *RXTE* has a limited response below 2 keV and this particular pulsar, with its soft pulses and low level emission, would not have been detected unless it went into outburst. Detailed analysis of the *XMM-Newton* survey of the SMC (Haberl *et al.*, 2012a) could reveal a further population of these softly pulsating HMXBs.

that quite definitely is the answer. I think the problem, to be quite honest with you, is that you've never actually known what the question is.

THE HITCHHIKER'S GUIDE TO THE GALAXY (1979)

3

Timing and Spectral Analysis of the Unusual X-Ray Transient XTE J0421+560/CI Camelopardalis

In this chapter I present a detailed X-ray study of the 2003 *XMM-Newton* observation of the sgB[e]-XRB CI Cam. This system consists of a compact object primary and supergiant B[e] secondary within a dusty torus, centred on the supergiant star. I decompose the apparently broad iron line into 3 separate components: FeI-Kα, FeI-Kβ and FeXXIV-XXVKα. It is unclear how both neutral and almost fully ionised iron can exist simultaneously, however I suggest this could be evidence that the compact object is embedded in the circumstellar material of the secondary star. This does not appear to be consistent with the X-ray flux and spectrum of the source, which has remained essentially unchanged since the initial outburst in 1998, which lead to this source's discovery. The iron abundance implied by the ratio of the neutral Fe-Kα and Fe-Kβ is compatible with solar. I find marginal evidence for an $\sim$10 ks lag in the neutral Fe-Kα light curve with respect to the continuum. I interpret this as the light crossing time of the torus which would suggest that the neutral iron is located at a radius of 10 AU. I discuss the nature of this system in light of the results and place it in context with other binary B[e] stars. The discus-

sion in this Chapter was written in collaboration with Dr. Simon Clark. Dr. Phil Uttley contributed the discussion on the use of the F-test for determining emission or absorption line significance.

3.1 Introduction

The X-ray transient XTE J0421+560 was discovered by the All-Sky Monitor on-board RXTE during a strong outburst in 1998 by Smith *et al.* It brightened to a peak flux of $\sim$2 Crab within a few hours before rapidly decaying, reaching quiescence in under two weeks. Observations at different wavelengths immediately after the outburst revealed similar behaviour in the optical and radio bands with a peak flux density of almost 1 Jy at 8.30 GHz (e.g. Clark *et al.* 2000). Initial radio observations suggested that there might be a superluminal expansion (Hjellming *et al.*, 1998), but subsequent analysis showed that the radio emitting region was expanding with a velocity of only $\sim$12,000 km s^{-1} (Mioduszewski and Rupen, 2004). The X-ray spectra seen by *SAX* (Frontera *et al.*, 1998), *RXTE* (Belloni *et al.*, 1999) and, more recently, *XMM-Newton* (Boirin *et al.*, 2002) are dominated by an emission feature at 6-7 keV attributed to the Fe-Kα fluorescence line.

The optical counterpart of XTE J0421+560 is CI Cam, a B0-2 supergiant B[e] star as classified by Clark *et al.* (1999), Hynes *et al.* (2002) and Robinson *et al.* (2002), establishing this system as a High Mass X-ray Binary (HMXB). Common properties of stars exhibiting the B[e] phenomenon are the presence of forbidden emission lines in their optical spectra and a strong infra-red (IR) excess. This IR excess is attributed to a hot circumstellar dust shell (Zickgraf *et al.*, 1986). Until the launch of *INTEGRAL* CI Cam was the only known sgB[e] companion star in a HMXB. *INTEGRAL* has since identified another sgB[e]-XRB candidate, IGR J16318-4848 (Courvoisier *et al.*, 2003).

The circumstellar gaseous environment of CI Cam has been under much scrutiny since the 1998 outburst. Robinson *et al.* (2002) propose a two-component wind from the sgB[e] star to explain their observations; a cool, low velocity "iron" wind and a hot, high velocity wind. The low velocity wind is dense, roughly spherical and extends to a radius of 13 to 50 AU. They note it is unclear as to how these winds with very different densities and velocities co-exist. Following a series of spectroscopic observations, Hynes *et al.* (2002) also conclude that the emission lines must originate from several physically separate regions. Unlike Robinson *et al.* (2002), they associate the H Balmer lines, He I and Fe II lines with the same region; a disk,

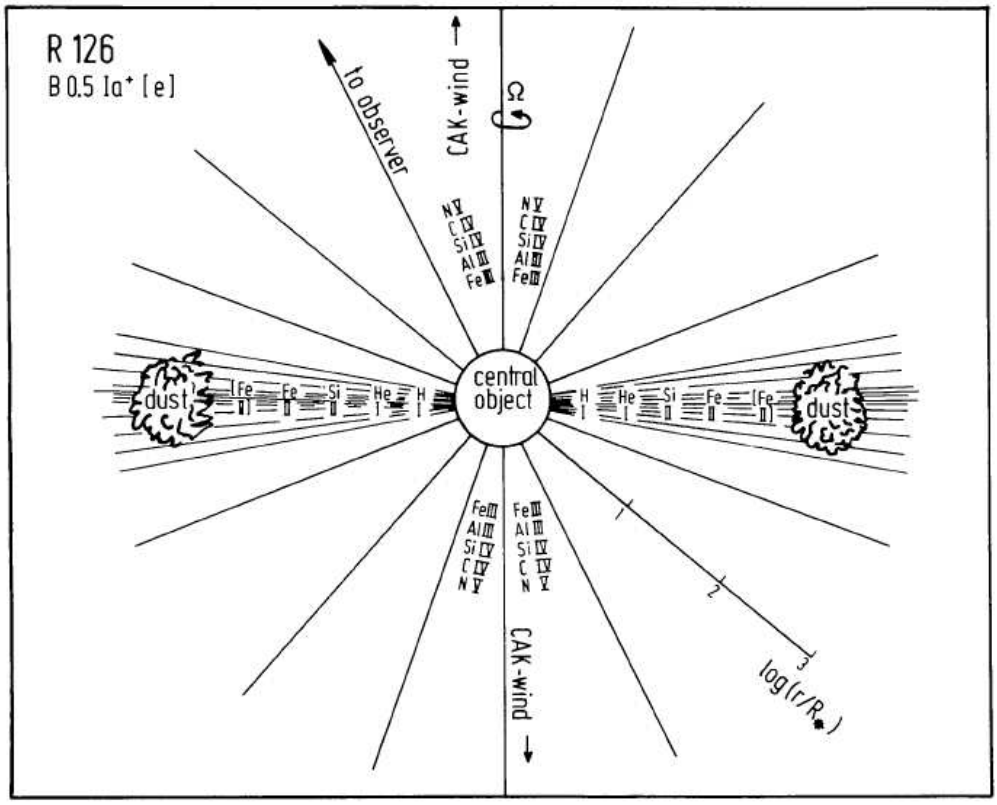

Figure 3.1: Proposed schematic of R126 - the archetypal sgB[e] star, taken from Zickgraf *et al.* (1985)

or equatorial outflow region, viewed nearly pole on. This is consistent with the two component stellar wind model for supergiant B[e] stars proposed by Zickgraf *et al.* (1985, 1986) (see Fig. 3.1).

Analysis of high resolution optical spectra by Miroshnichenko *et al.* (2002), observed almost 3 years after the outburst, revealed clearly resolved emission line profiles, displaying a triple peak structure. They suggest that this implies an intermediate inclination angle of the circumstellar disk with respect to the line of sight. Recent interferometric work in the near infrared over an eight year period from the outburst by Thureau *et al.* (2009) resolves the emitting region. They model this as a skewed elliptical Gaussian ring with semi-major axis $a = 19.0 \pm 1.2$ AU (assuming a distance of 5 kpc) with an inclination angle of $i \simeq 67^{\circ}$ (see Fig. 3.2). Barsukova *et al.* (2006) report a 19.41 ± 0.02 day orbit period in the optical light curve of CI Cam, along with Doppler shifts in the HeII 4686 Å line on the same time scale. The proposed period would put the semi-major axis of the binary orbit between 100-130 $R_{\odot}$: close to the surface of the star (based on mass and radii measurements of sgB[e] stars by Zickgraf *et al.* 1986).

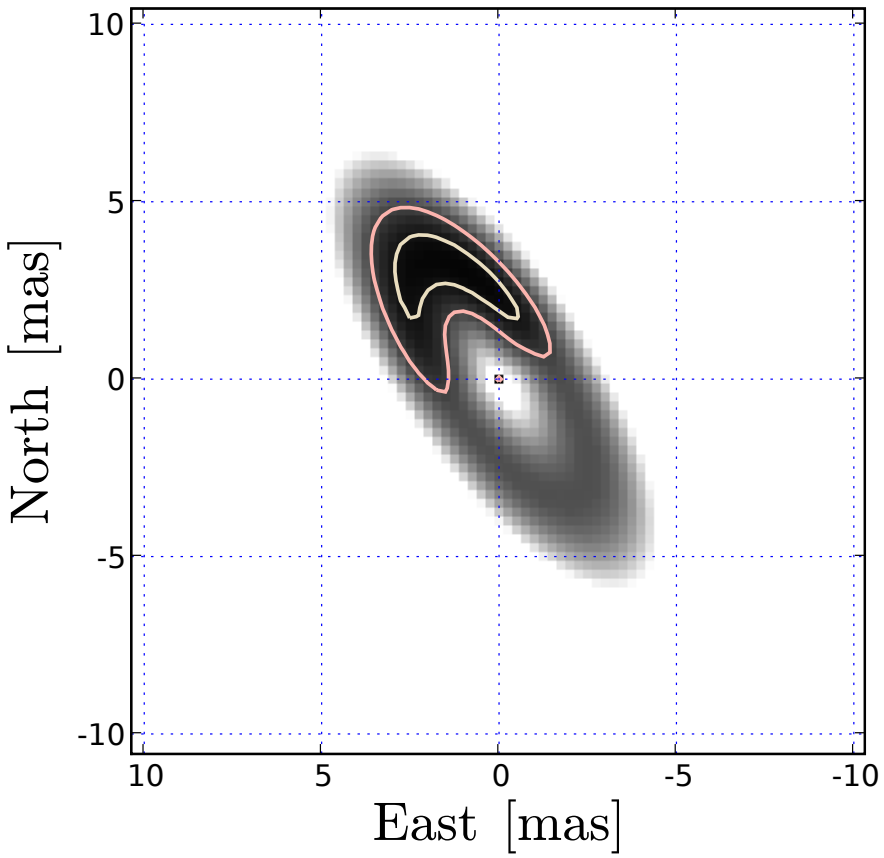

Figure 3.2: The best-fitting Gaussian skewed ring model to the infra-red interferometry data, taken from Thureau *et al.* (2009)

Unfortunately, distance estimates to XTE J0421+560 are uncertain with a wide range of values being adopted in the literature. This is primarily due to the lack of reliable spectral diagnostics available to determine the luminosity class of the mass donor. Consequently, estimates range from 1-17 kpc. This in turn means that the X-ray luminosity of the outburst is not well constrained and as a result the nature of the compact object of this binary system is still unclear. We critically discuss the distance and nature of the system in Section 3.5.

3.2 Observations and Data Reduction

The X-ray observation discussed in this Chapter was taken during satellite revolution #588 on February 24, 2003. The observational data files, light curves and spectra were processed and produced following the procedure detailed in Section 2.2.2. Table 3.1 summarises the details of the EPIC observations. The data were processed using the *XMM-Newton* SAS v9.0 along with software packages from

Table 3.1: *XMM-Newton* EPIC observations of XTE J0421+560 on 2003 February 24

Camera	Filter	Read out Mode	Observation MJD	Start	End(UT)	Exp. (ks)
MOS1/2	Medium	Full Frame	52694.5	12:34	05:50	59.5
pn	Thin1	Full Frame		12:56	05:50	60.3

FTOOLS v6.8.

Source counts were extracted from a 24 arcsec radius region (as recommended by the SAS task eregionanalyse) centered on XTE J0421+560 and were compared with those from statistically identical background regions with extraction radii 60 arcsec. Whilst several periods of high background activity are present in the data, the source is brighter than the background for all but the final $\sim$13 ks of the observation. Hence we have not included this final section in the light curves reported here. The closest of the statistically identical background region (located on a neighbouring CCD as the source in the case of the pn and the same CCD for the MOS detectors) was used as the final background region for the light curves presented in this Chapter. For the spectra, periods of high background activity were screened by removing any times when the single pattern count rate above 10 keV was $>$0.8 cts s^{-1} for the MOS detectors and $>$1.5 cts s^{-1} for the pn detector.

3.3 Spectral Analysis

The spectral analysis discussed in this work was performed using XSPEC (Arnaud, 1996) version 12.7.0. The spectra from the three EPIC detectors were fit simultaneously with the model parameters constrained to be identical across the three instruments. All models have an additional constant factor to account for the instrumental differences. All elemental abundances are set to the values of Wilms *et al.* (2000) unless otherwise stated.

Figure 3.3 shows the spectrum of XTE J0421+560 both before and after background subtraction along with the background spectrum used. The spectrum of XTE J0421+560 is characterised by heavy absorption and a large emission feature at $\sim$6.5 keV. Boirin *et al.* (2002) report a soft ($<$2 keV) excess in their 2001 observation. Whilst there does appear to be evidence for a soft excess in the background subtracted spectrum, when the uncorrected source spectrum is compared with the background spectrum, the shape of the spectrum and value of the data points below

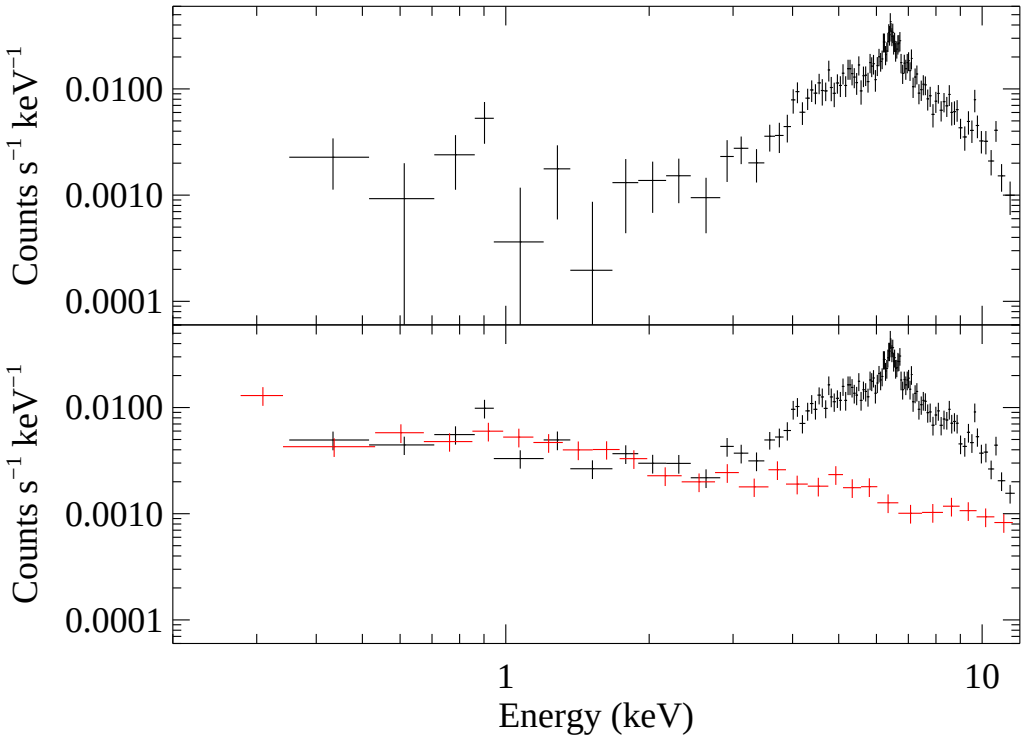

Figure 3.3: The 0.2-12.0 keV spectrum of XTE J0421+560. Top panel shows the background subtracted spectrum, bottom panel shows the source spectrum before background subtraction (in black) along with the spectrum of the background (red). All spectra are normalised.

3 keV are almost identical. A visual inspection of the X-ray image shows no detection of the source below 3 keV. Whilst the existence of a soft excess in the spectrum of XTE J0421+560 cannot be ruled out, I believe that this could be an artifact of the background subtraction and so do not include the $<$3 keV data points in the model fits.

The continuum of the spectrum was first fit by excluding the data around the iron line region (6.2-6.9 keV). The absorption was modeled with two elements, a Galactic foreground component, $N_{H,Gal}$ fixed to 4.5×10^{21} cm^{-2} (Dickey and Lockman, 1990) and a separate column density, $N_{H,i}$, intrinsic to the source which was allowed to vary. A simple absorbed power-law model (*phabs*phabs*powerlaw* in XSPEC) yielded a respectable fit with a χ^2 value of 135.6 for 128 degrees of freedom (dof; $\chi^2_r = 1.06$). A partially covered power law model was also fit to the data (*phabs*pcfabs*powerlaw* in XSPEC). In this model the underlying power law is fractionally covered by an absorbing material with the uncovered emission absorbed by the interstellar medium. This did not improve the continuum fit with a χ^2 value of 144.4 for 127 dof ($\chi^2_r = 1.14$). I also fit the continuum with a power

law partially covered by an ionised absorber (*phabs*zxipcf*po* in XSPEC). This produces a statistically better fit than the partial covering model alone with a χ^2 of 138.4 for 133 dof ($\chi^2_r = 1.04$), but with unfeasible model parameters ($\Gamma = 3.4^{+1.3}_{-1.6}$). Again, the covering fraction and ionisation parameter both suggest that an ionised partial covering model is unnecessary.

The region around the iron line was then included in the model fit. A single (unabsorbed), intrinsically narrow, Gaussian was added to the model with the energy of the line allowed to vary. The resulting fit has a Kα line at 6.43 ± 0.02 keV. The fit has a χ^2 of 196.7 (χ^2_r of 1.17 for 168 dof). A better fit is produced by allowing the Gaussian width to vary (χ of 167.3; χ^2_r of 1.00 for 167 dof), with a broad iron line at 6.48 ± 0.04 keV with $\sigma = 0.23^{+0.08}_{-0.06}$ keV. Figure 3.4 shows the EPIC-pn spectrum of the iron line region along with the best fit narrow and broad iron lines. Whilst statistically better than a single, narrow Gaussian, this fit has significant residuals and appears to be fitting the iron edge at 7.1 keV within the Gaussian. I do not believe this fit is physical.

A second intrinsically narrow Gaussian was added to the model at 6.67 keV, consistent with ionised Fe-Kα. This further reduced the χ^2 to 171.0 (χ^2_r=1.03 for 166 dof). Finally, a Kβ line was added to the model fixed at 7.06 keV. The normalisation was initially constrained to be 0.13 of that of the Kα line (Kaastra and Mewe, 1993). This reduced the χ^2 to 164.7 (χ^2_r=0.98 for 168 dof). When the normalisation and energy are unconstrained the line energy remains essential unchanged ($E_{K\beta} = 7.05^{+0.08}_{-0.07}$) and the ratio between Kβ and Kα rises to 0.3 ± 0.2, consistent with the theoretical value.

Determining the significance of the iron lines in the spectrum is tricky. Protassov *et al.* (2002) in particular warn against using the F-test to determine the significance of an emission line. One of the main criteria for using this statistical tool is that the two models in question must be nested, i.e. the parameter values of one model must be a subset of the second model. Allowing the line energy to be free (as in the fitting) means that the models are no-longer nested and so the energy of the line cannot be incorporated as a free-parameter in the F-test. Instead, I need to allow for the fact that I have conducted a number of trials, N, over the energy range of the line. Conservatively, I estimate that the chance detection probability is at most $\sim 1-(1-P)^N$, where P is the probability value returned by the F-test (see Porquet *et al.* 2004 for a full discussion). Since the line energies are within the instrument resolution of the expected values of 6.4 keV and 6.7 keV and not simply at some arbitrary redshift, the number of independent trials that I have effectively searched over is small. Here I adopt a value of 3 for N.

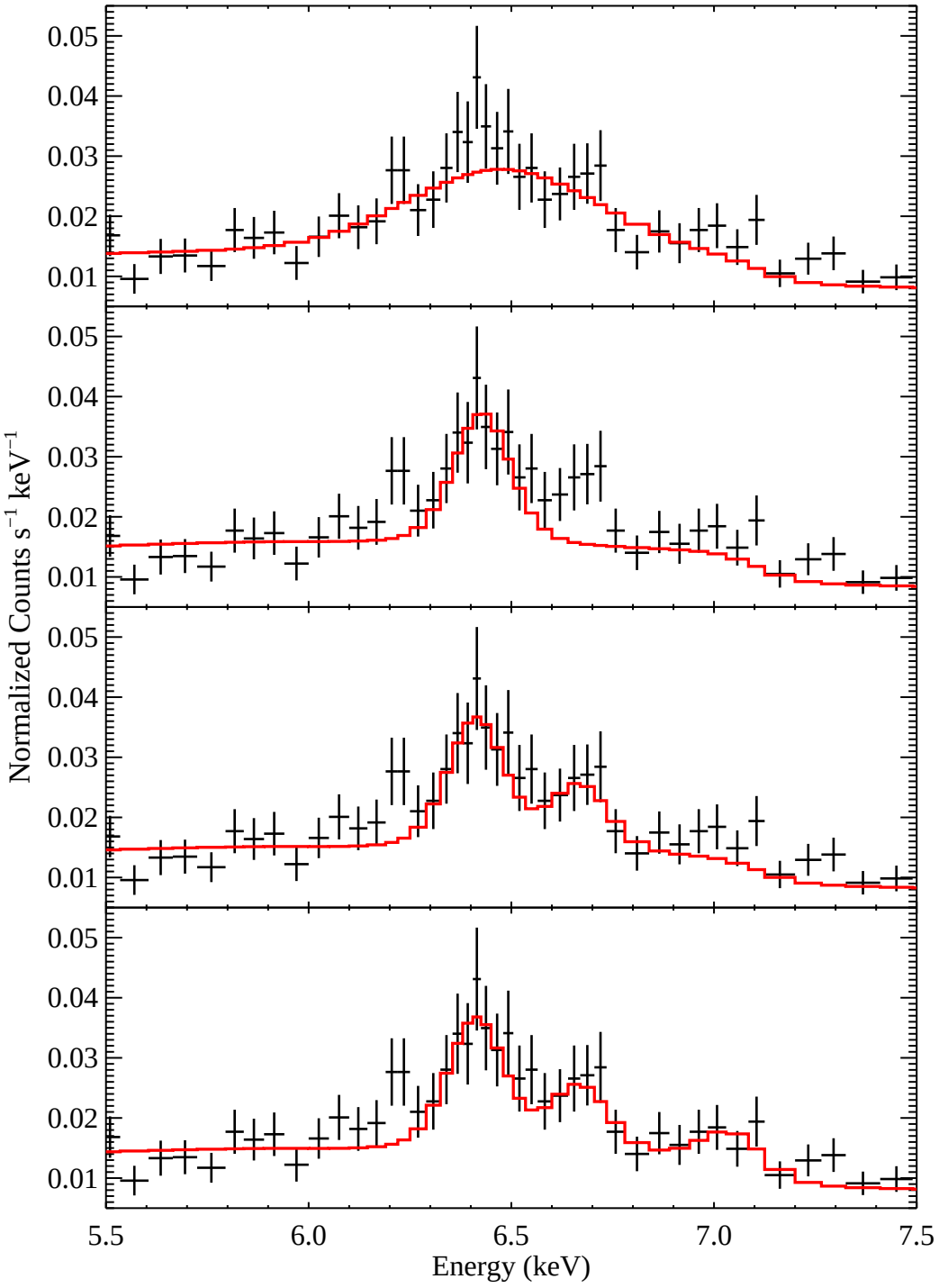

Figure 3.4: The EPIC-pn spectrum of XTE J0421+560 around the iron line. Top panel shows the single broad Fe-Kα line fit to the data, second panel shows the intrinsically narrow neutral Fe-Kα and ionised Fe-Kα line (see text), bottom panel shows the intrinsically narrow neutral Fe-Kα and Fe-Kβ line and ionised Fe-Kα line.

Table 3.2: Best fit parameters for the absorbed power law model fits to the full 3.0-12.0 keV spectrum. The abbreviations for the different model components are:"*ph*" for *phabs*, "*po*" for *powerlaw* and "*G*" for *Gaussian*. The widths of all Gaussians are fixed at 0 keV, i.e. intrinsically narrow. Errors, where reported, are the 90% confidence level.

Model			FeI Kα		FeXXIV-XXV Kα		FeI Kβ			
	$N_{H,i}$ ($\times 10^{23}$cm^{-2})	Γ	Energy (keV)	Flux (ph s^{-1} cm^{-2})	Energy (keV)	Flux (ph s^{-1} cm^{-2})	Energy (keV)	Flux (ph s^{-1} cm^{-2})	χ^2/dof
*ph*ph*po*	5.6 ± 0.6	1.4 ± 0.2	-	-	-	-	-	-	280.1/170
ph((ph*po)+G)*	$4.8^{+0.6}_{-0.5}$	1.2 ± 0.2	$6.43^{+0.02}_{-0.03}$	$(6 \pm 1) \times 10^{-6}$	-	-	-	-	196.7/168
ph((ph*po)+G+G)*	4.5 ± 0.5	1.1 ± 0.2	$6.42^{+0.01}_{-0.03}$	$(6 \pm 1) \times 10^{-6}$	$6.67^{+0.03}_{-0.04}$	$(3 \pm 1) \times 10^{-6}$	-	-	171.0/166
ph((ph*po)+G+G+G)*	4.4 ± 0.5	1.0 ± 0.2	$6.41^{+0.03}_{-0.02}$	$(6 \pm 1) \times 10^{-6}$	$6.67^{+0.02}_{-0.03}$	$(3.3^{+0.9}_{-1.0}) \times 10^{-6}$	$7.05^{+0.08}_{-0.07}$	$(2.0 \pm 0.9) \times 10^{-6}$	161.0/164

Table 3.3: Estimates of the significance of the iron lines based on the two methods described in the text. Errors, where reported, are the 90% confidence level.

F-Test	FeI Kα	FeXXIV-XXV Kα	FeI Kβ
F statistic	79.3	30.4	10.1
Chance detection probability	2.2×10^{-15}	3.8×10^{-7}	5.2×10^{-3}
Equivalent width	**FeI Kα**	**FeXXIV-XXV Kα**	**FeI Kβ**
Eqwidth (eV)	220^{+90}_{-50}	100^{+30}_{-40}	90 ± 50
Significance	7.24σ	4.11σ	2.96σ

The data were fit with the simple absorbed power law model and the narrow iron lines added incrementally, as described above. They were then frozen at the best fit energy from the *phabs*((phabs*po)+Gaus+Gaus+Gaus)* model and an F-test was performed after the addition of each line. As such each model is compared with the previous, simpler model. The significances were also estimated using the equivalent widths of the lines and their errors. The results of both of these methods are listed in Table 3.3. Both the neutral and ionised Kα lines appear to be clearly significant. There appears to be only a marginal detection of the expected Kβ line, nonetheless the flux of the line is consistent with Solar metallicity. A considerable iron abundance would be required for a strong detection of this line with the signal to noise reported here.

The continuum and line parameters for the best fit model are listed in Table 3.2. Figure 3.5 shows the best fit model to the spectrum. The final model fit has a photon index of $\Gamma = 1.0\pm0.2$ and an intrinsic absorption of $N_H = 4.4\pm0.5\times10^{23}$ cm^{-2}, with a χ^2 of 161.6 (χ^2_r=0.98 for 164 dof).

I also attempted to fit the thermal model of Ishida *et al.* (2004), derived from an *ASCA* observation, to the data. In this model emission from two regions of hot diffuse gas are photoelectrically absorbed independently (*phabs*mekal+phabs*mekal* in XSPEC) with the elemental abundances of Anders and Grevesse (1989). The parameters were frozen to the best fit values of Ishida *et al.* (2004), with only the normalisation allowed to vary, and fit to the 0.5-10.0 keV spectrum. This is the energy range investigated by Ishida *et al.* (2004) and allowed for a direct comparison. The resulting fit was poor with a χ^2 of 1023.6 (χ^2_r=5.62 for 182 dof), rising to 1040.6 (χ^2_r=6.09 for 171 dof) when only the 3.0-12.0 keV energy range was considered. Allowing the absorption and plasma temperature to vary improved the fit (χ^2=308.2; χ^2_r=1.7 for 178 dof) but with unfeasible model parameters (e.g. $N_H \sim 10^{26}$ cm^{-2}, kT$\sim$80 keV).

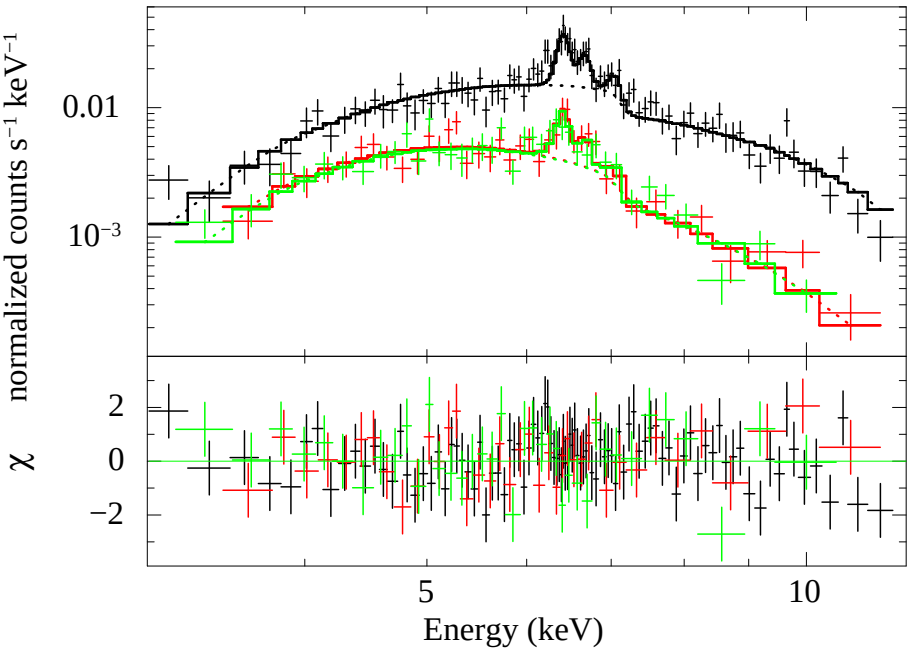

Figure 3.5: EPIC-pn (black), EPIC-MOS1 (red) and EPIC-MOS2 (green) spectra, along with best t *phabs*((phabs*po)+Gaus+Gaus+Gaus)* model to the data (solid line). Broken line shows the absorbed power law component.

3.4 Timing Analysis

Figure 3.6 shows the background subtracted 3.0-12.0 keV light curve for XTE J0421+560, with a bin time of 500 s, from the EPIC-pn detector. The total net counts for the light curve, after background subtraction and excluding triple and quadruple pixel events, is ∼5000 counts. This corresponds to an average net count rate of 0.107±0.002 counts s^{-1}, substantially brighter than the 2001 observation which found 0.024±0.002 counts s^{-1} (Boirin *et al.*, 2002). The light curve has a fractional root-mean-squared variability amplitude of 0.37 (calculated using equation (10) of Vaughan *et al.* 2003).

Figure 3.7 shows the source light curve split into three different energy bands. The top panel shows the light curve for the lower energy continuum (4.5-6.0 keV), the middle panel shows the light curve in the range defined as the Fe-Kα line from the spectral fits (6.20-6.55 keV) and the bottom panel shows the light curve for the higher energy continuum (7.5-9.0 keV). The Fe-Kα line spans a much narrower range of energies than the continuum light curves. This is to avoid contamination from the hypothesised ionised Kα line and the Kβ line, as well as to minimise any contribution of the underlying continuum to the cross correlation function (CCF).

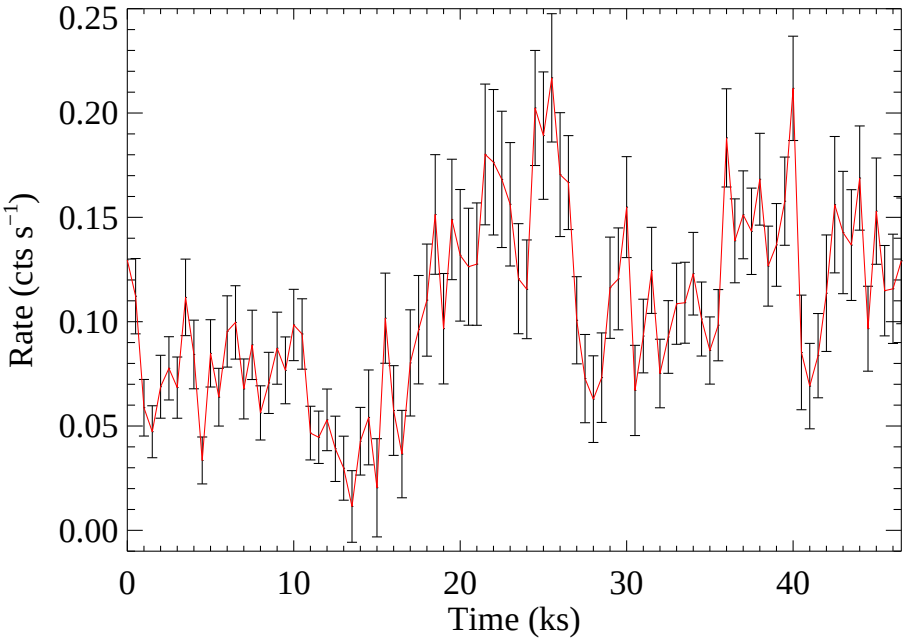

Figure 3.6: Background subtracted 3.0-12.0 keV light curve of XTE J0421+560 from the EPIC-pn detector.

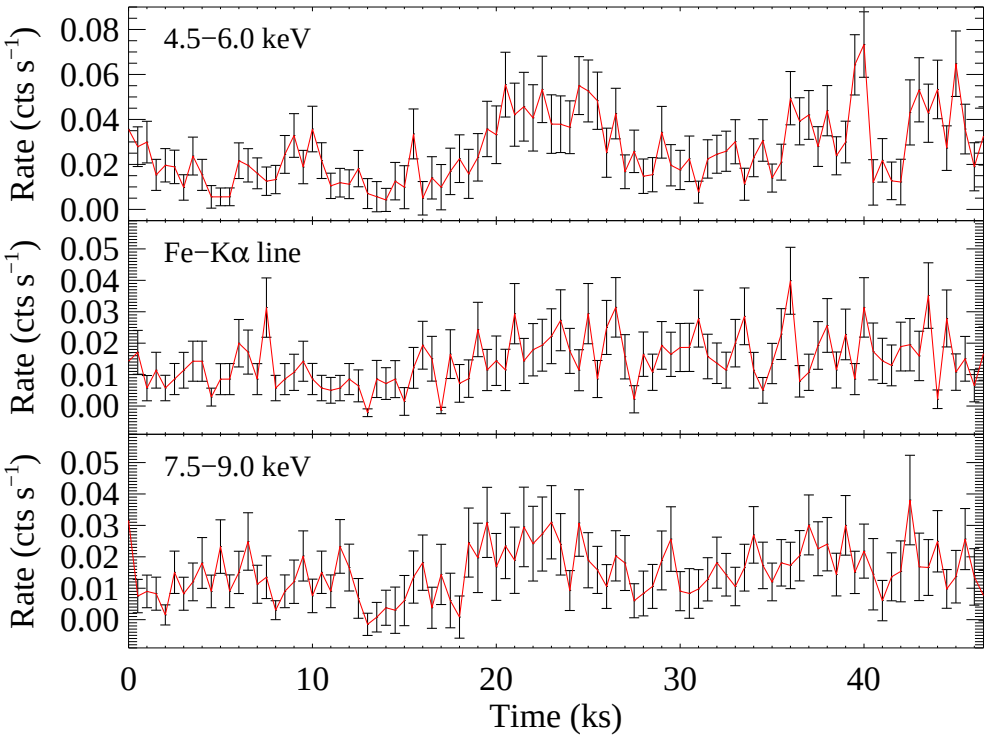

Figure 3.7: light curves of the background subtracted low energy continuum (4.5-6.0 keV), the Fe-Kα line (6.2-6.55 keV) and the high energy continuum (7.5-9.0 keV).

Above $\sim$9.0 keV the signal to noise of the system reduces and so these data are not included in the analysis.

Cross-correlation analysis was performed on the three light curves mentioned above and an additional low and high energy continuum light curves with energy ranges 3.0-4.5 keV and 9.0-10.5 keV respectively. The IDL routine c_correlate.pro from the IDL Astronomy User's Library[1] was used throughout. The continuum light curves were correlated with the sum of the other 3 continuum light curves (i.e. the rest of the spectrum without the iron line complex). The Fe-Kα line light curve was correlated with the sum of all the continuum light curves. Figure 3.8 shows the CCFs of the light curves with respect to the continua. The solid black lines are the same CCFs, smoothed using a moving average method with a window size of 3500 s (7 time bins) in an attempt to minimise the noise. A positive time delay corresponds to a lag in the variation of the light curve with reference to the continua. The Fe-Kα CCF appears to be more asymmetric than its continuum counterparts. More explicitly, the minimum present in the continua CCFs around $\sim$10 ks does not seem to be present.

Whilst the energy range of the Fe-Kα line has been deliberately defined to keep continuum contamination at a minimum, inevitably there will be some contamination as there is no way to separate the line emission from the continuum emission at these energies. As such I expect to see some correlation of the light curves at zero lag. However, an asymmetry in the CCF is often interpreted as evidence for a lag (e.g. Peterson *et al.* 1998) and so I explore the possibility that the shape of the CCF could be due a transfer function which includes some power at positive lags.

I define the "asymmetry factor", A_{sym}, of the CCFs to be the ratio of the difference of the half widths of the peak at tenth maximum, to the sum of the half widths. This gives a number between -1 and 1, with zero being perfectly symmetrical. A positive value of A_{sym} indicates that the gradient of the peak is steeper on the negative lag side and vice versa for a negative value. The A_{sym} values of the continua CCFs are all very similar, ranging from -0.04 to -0.08, suggesting they are essentially symmetrical. However, the A_{sym} value for the Fe-Kα CCF is 0.39, indicating a moderate level of asymmetry.

The method of Zhang (2002) was then used to see if the asymmetry seen in the Fe-Kα CCF could be caused by Poisson noise. Monte-Carlo simulations were performed to assess the significance of this asymmetry. Ten thousand red-noise light curves were generated with a power law slope of -2.0 using the method of Timmer

[1] http://idlastro.gsfc.nasa.gov/

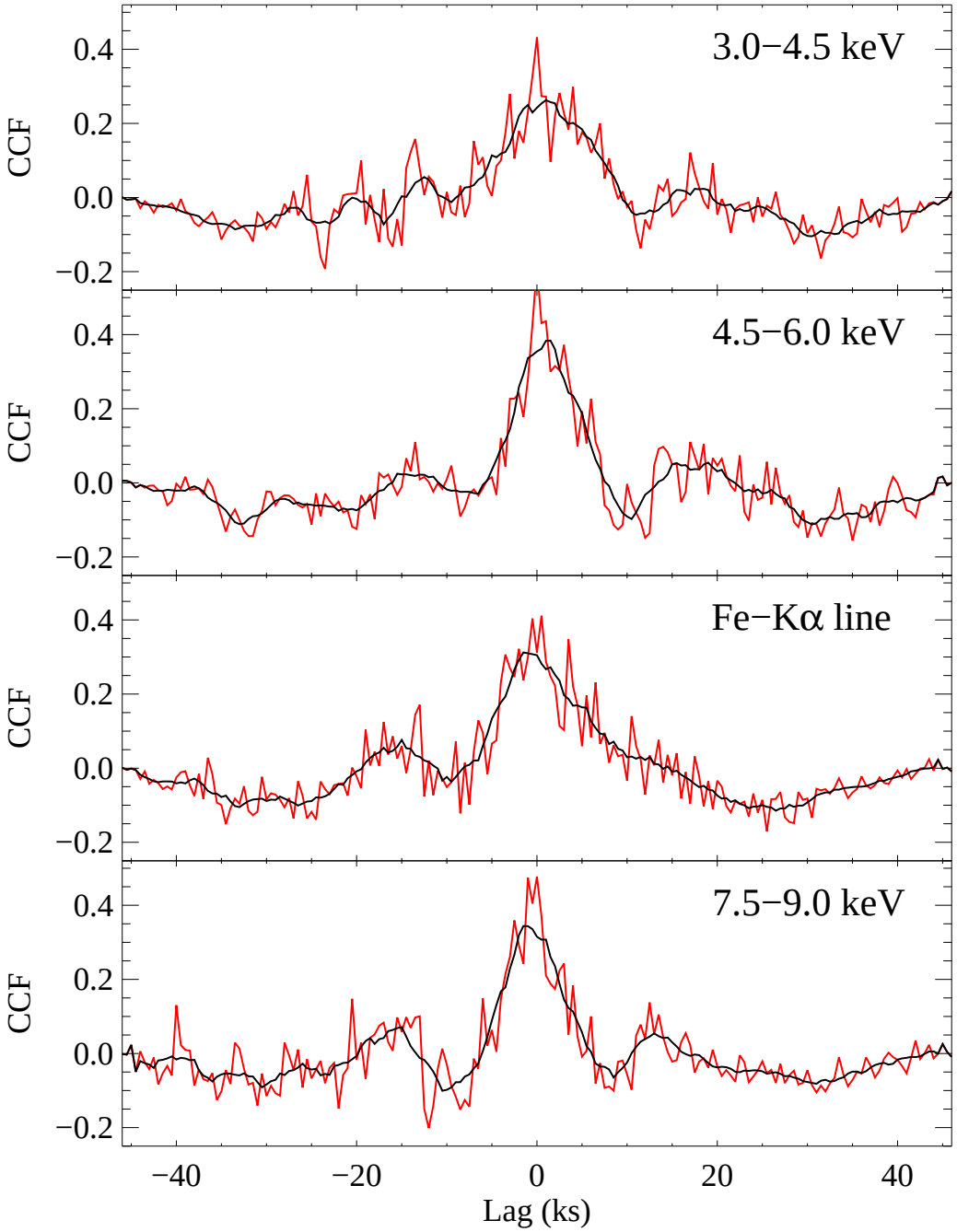

Figure 3.8: The cross-correlation functions of the light curves. The continua light curves (3.0-4.5 keV, 4.5-6.0 keV and 7.5-9.0 keV) were cross-correlated with the sum of the remaining continua light curves whilst the Fe-Kα (6.2-6.55 keV) light curve was cross-correlated with the sum of all the continua light curves. The solid black line is smoothed CCF.

and Koenig (1995) and the IDL routine rndpwrlc.pro. The light curves were initially simulated with a duration ten times longer than that of the actual data and were then cut down to the observed duration to account for red-noise leakage. The simulated light curve was then used to create four light curves with the statistical properties of the observed light curves, resulting in four identical light curves distinguishable only by their mean and standard deviation. Noise was then added to each data point of the simulated light curves by adding a Gaussian deviation with a mean of zero and a variance equal to that of the corresponding data point in the real light curve (similar to the method of Uttley *et al.* 2003). Any negative data points were then set to zero. The three continuum light curves were then combined and cross-correlated with the fake Fe-Kα line light curve in the exact same manner as the observed data. The asymmetry factor and peak value of the smoothed CCFs were then calculated.

Of the 10^4 CCFs generated in the Monte Carlo simulation, 303 were observed to have $A_{sym} > 0.39$ suggesting a significance of $\sim$97% or 2.1σ. This result remains at a similar significance (2.3σ) when a red noise power law index of -1.0 is considered. The asymmetry factors and peak values of the continuum CCFs all fall within the central 50% of the distribution. Whilst this result is not formally significant, the low signal to noise of the data makes a convincing result unlikely.

3.5 Discussion

The continuum parameters of the best fit model are consistent with those reported by Boirin *et al.* (2002). The total 3.0-10.0 keV flux of the model is $(1.36^{+0.04}_{-0.05}) \times 10^{-12}$ erg cm^{-2} s^{-1} corresponding to an X-ray luminosity of $L_{X(3-10keV)} = (4.1^{+0.1}_{-0.2}) \times 10^{33}$ erg s^{-1} at a distance of 5 kpc. This is a slight increase on that seen in the previous *XMM* observation ($L_{X(0.5-10keV)} = 3.5 \times 10^{33}$ erg s^{-1}; Boirin *et al.* 2002), however as there are no errors quoted on this value I cannot say whether this increase is significant. Whilst these luminosities do not cover the same energy range, as the system is undetected below 3 keV in this *XMM* observation it is unlikely that the $L_{X(0.5-10keV)}$ will vary much from the luminosity reported above. The flux values used to calculate the luminosities are derived from the spectral fits and so are also model dependant. The light curve seems to contradict the results from the spectral fits to the data, suggesting a factor of 4.46$\pm$0.09 increase in the average count rate over the two year period between data sets. A *BeppoSAX* observation in 2000 put an upper limit on the X-ray luminosity of $L_{X(1-10keV)} < 2.5 \times 10^{33}$ erg s^{-1} (Parmar *et al.*, 2000). As such, the X-ray emission from the source does appear to

have shown a moderate level of variability over the last few years.

The improved signal to noise has allowed the apparently broad Gaussian, reported by Boirin *et al.* (2002), to be decomposed into three intrinsically narrow components, neutral Fe-Kα and Kβ and helium like FeXXV Kα. It is unclear how both neutral and almost fully ionised iron can co-exist and only seems possible if the ionised line emission arises from a physically separate region from the neutral emission, possibly local to the compact object. This would require the compact object to be in the same plane as the equatorial outflows of the companion star and seems inconsistent with the X-ray activity of the system. The iron abundance implied by the ratio of the neutral Kα and Kβ line fluxes is just consistent with solar within errors.

Figure 3.9 shows the current hypothesised geometry for CI Cam proposed by Thureau *et al.* (2009), consisting of a binary system well within the torus. If it is assumed that the high column density originates from the leading (i.e. closest) edge of the surrounding torus (see Fig. 3.9) then the inclination, $i \sim 67^{\circ}$, and semi-major axis, a=19 ± 1.2 AU (Thureau *et al.*, 2009), give a lower limit to the height of the torus of 8.1 ± 0.5 AU. This is highly dependent on both distance and inclination angle, neither of which are secure.

The Kα fluorescence line of iron is already considered a powerful diagnostic tool for probing the central regions of both Galactic black hole candidate systems and active galactic nuclei (Reynolds and Nowak, 2003). A technique known as reverberation mapping involves searching for time dependent changes in the continuum, emitted by the primary X-ray source, and then looking for the echo, or "reverberation", in the emission lines located further out. The relationship between the continuum light curve and the emission line light curve is characterised by a geometry dependent "transfer function". Some idea of the spatial extent of the emission line region can be achieved by cross-correlating the light curves of the emission line, $L(t+\Delta\tau)$, and the continuum, $C(t)$. The function produced will be maximised at the lag, $\Delta\tau$, between the emission line and the X-ray continuum. If I assume that all the neutral iron is located in the torus at radius *r*, that the compact object is in the centre of the torus (i.e. that the semi-major axis of the orbit is negligible compared to the semi-major axis of the torus) and that the X-ray emission is isotropic, then the range of lags seen is simply

$$\Delta\tau = \frac{r}{c}(1-\cos\theta) \tag{3.1}$$

where θ is the angle, between the line of sight and the X-rays incident on the torus

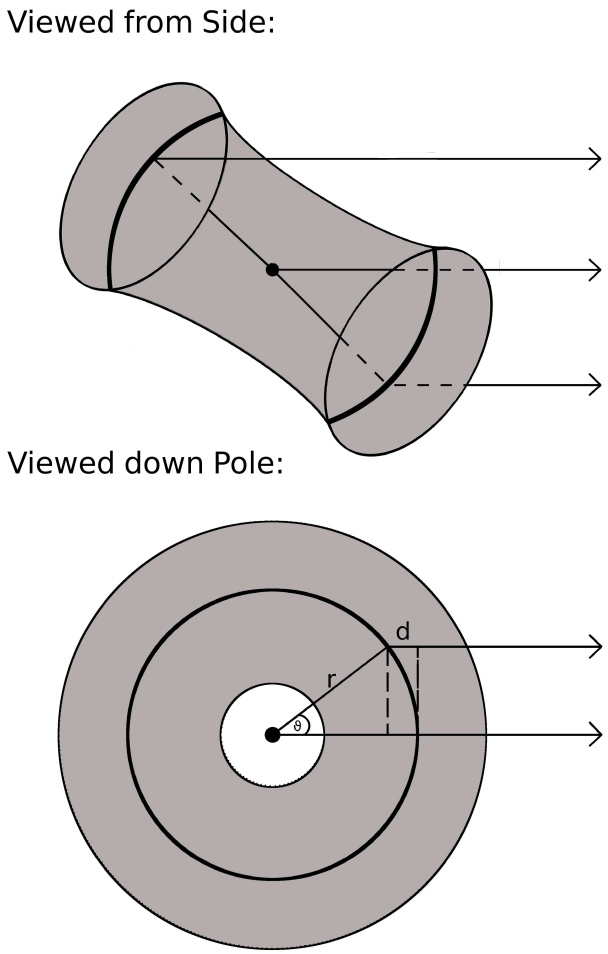

Figure 3.9: Sketch of the proposed geometry for CI Cam. The top figure shows the cross-section of the torus, whist the bottom figure shows the system as viewed down the pole. The thicker black ring at radius, *r*, is the assumed location of the neutral iron. The central object in this case is the sgB[e] star. The position of the compact object is believed to be close to the surface of the optical star and thus lying well within the torus (Barsukova *et al.*, 2006).

(see Fig 3.9). A more in depth description along with the fundamental principles and assumptions of reverberation mapping is given by Blandford and McKee (1982) and Peterson (1993).

There appears to be evidence for an asymmetry in the CCF of iron Kα energy range with the continuum, however much higher signal to noise data is needed to confirm this. If I consider the light curve of the Fe-Kα energy range, $L(t+\Delta\tau)$, as the sum of two lightcurves, $L_1(t+\Delta\tau)$ representing the line emission and $L_2(t)$ representing the continuum "underneath" the iron line in the same energy range,

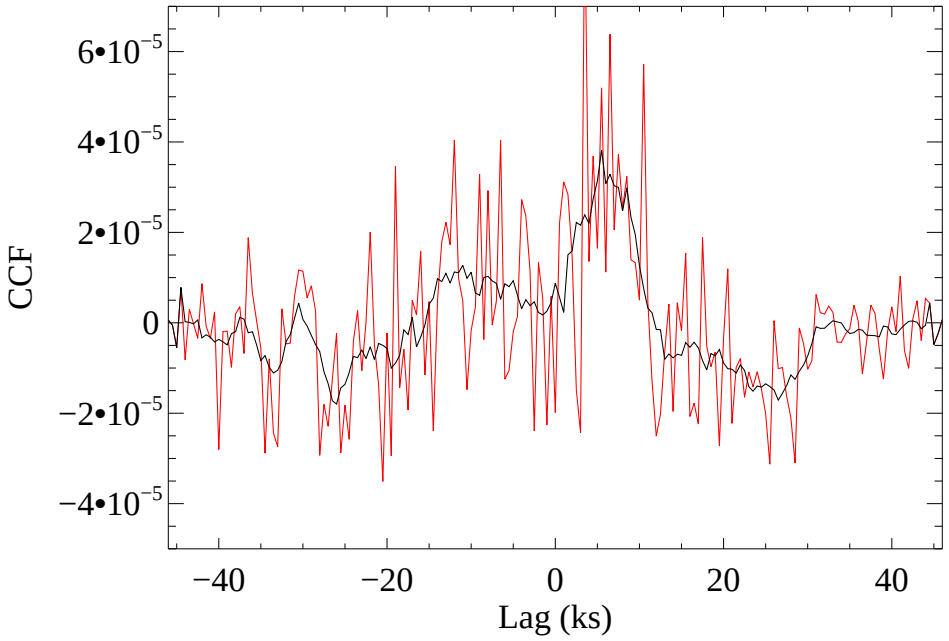

Figure 3.10: The CCF produced when the un-normalised 7.5-9.0 keV CCF is subtracted from the un-normalised Fe-Kα CCF.

then the CCF produced can be expressed as the sum of two CCFs:

$$\begin{aligned} F_{CCF}(\tau) &= \int_{-\infty}^{\infty} L(t+\Delta\tau)C(t)\,dt \\ &= \int_{-\infty}^{\infty} (L_1(t+\Delta\tau)+L_2(t))C(t)\,dt \\ &= \int_{-\infty}^{\infty} L_1(t+\Delta\tau)C(t)\,dt + \int_{-\infty}^{\infty} L_2(t)C(t)\,dt \end{aligned} \tag{2}$$

The first component of equation 2 represents the *un-normalised* CCF of the pure line emission (i.e. the CCF is not normalised by the root mean square of the light curve in each band) and the second component the *un-normalised* CCF of the underlying continuum. If this asymmetry is real and the continuum behaviour is simple and well represented by the CCF of the 7.5-9.0 keV light curve with the continuum (chosen as it is these photons which will be directly promoting the K-shell electrons into the L-shell), then subtracting the un-normalised 7.5-9.0 keV CCF from the un-normalised Fe-Kα CCF will leave the CCF of the pure Fe-Kα emission with the continuum.

Figure 3.10 shows the result of subtracting the un-normalised 7.5-9.0 keV CCF from the un-normalised Fe-Kα CCF (consistent with the mathematical proof above).

The poor signal to noise is in part a result of the 0.34 fluorescence yield of iron (Bambynek *et al.*, 1972); only $\sim$1 in 3 of the incident photons with energies $>$6.4 keV will result in a Kα photon. However, there does appear to be a distinct peak at 5-10 ks.

The most likely values of τ from equation 3.1 are ~ 0 and $\sim 2r$, where r is the radius of the torus. If the peak is interpreted as the lag at $2r$ then this would indicate that the neutral iron is located at a radius of $\sim$10 AU from the centre of the torus. This result relies on several assumptions and parameters which are by no means secure. The derived semi-major axis of the orbit (from the period of Barsukova *et al.* 2006) depends on the cubed root of total mass of the system. As such large changes in the total mass of the system only produce small alterations in the semi-major axis. Consider a companion star of mass $50 \pm 30\ M_{\odot}$ and a compact object with a mass $5 \pm 5\ M_{\odot}$ (consistent with observed neutron star and stellar mass black hole mass estimates), then the semi-major axis is 0.5 ± 0.1 AU. This is a small fraction of the semi-major axis of the torus and so the approximation that the compact object is at the centre of torus seems valid. However, in reality the neutral iron is unlikely to be located in an infinitesimally thin ring in the torus, it seems more likely that there exists an inner radius at which neutral iron can form. In this case a lag would also have a more complex density dependence than the one that is considered here. Both these factors will serve to broaden the peak seen at $2r$, and so the derived radius is likely the radius where the neutral iron density is at a maximum.

3.5.1 The nature of CI Cam

A significant obstacle to understanding the nature and behaviour of CI Cam is the uncertainty in the distance, with estimates ranging from $\sim$ 1.1 kpc (Barsukova *et al.*, 2006) to $>$10 kpc (Robinson *et al.*, 2002). The consequential uncertainty in the luminosity impacts on the nature of both the mass donor and the accretor, with the former authors favouring a B4III-V + white dwarf model and the latter a sgB[e] star + relativistic accretor (neutron star or black hole). In support of the former interpretation, Ishida *et al.* (2004) infer the presence of a white dwarf from analysis of the *ASCA* X-ray spectrum. This was fit with an optically thin, thermal hard X-ray model, characteristic of cataclysmic variables which contain a white dwarf. Our analysis (Section 3) clearly favours the power law model, with similar parameters to those reported for the other known sgB[e] HMXB, IGR J16318-4848 (Matt and Guainazzi, 2003; Barragán *et al.*, 2009), which Filliatre and Chaty (2004) claim hosts a neutron star based on the ratio of the X-ray and radio flux (though they

note that the unique environment means they are cautious about applying such a relationship). The photon index reported is also consistent with those found in neutron star Be/X-ray binaries by Haberl *et al.* (0.6-1.4; 2008).

Additionally, Ishida *et al.* (2004) favour a rather large distance of 5-17 kpc for CI Cam, based on the relationship between the peak flux and the decay timescale of novae. This is significantly in excess of that suggested for such an accretor by Barsukova *et al.* (1.1-1.9 kpc; 2006), a range derived assuming a main sequence donor star which in turn has been inferred from the widths of the wings of the photospheric profiles of the high Balmer series. However, the authors note that the stellar mass implied by their analysis of the orbital period is in excess of that expected for such a classification. Hynes *et al.* (2002) caution against this approach due to significant contamination by the emission spectrum of the circumstellar disk. Support for a larger distance is also provided by an analysis of the optical NaD lines by Hynes *et al.* (2002), who infer a *minimum* distance of ~ 4 kpc to CI Cam; noting that this would be inconsistent with the spectral classification of the mass donor by Barsukova *et al.* (2006).

An alternative approach is to employ the (uncontaminated) UV spectrum obtained during quiescence (Robinson *et al.* 2002; Hynes *et al.* 2002). In particular, the P Cygni profiles observed in the SiIV 1394, 1402Å and CIV 1549, 1551Å doublets serve as powerful luminosity (and temperature) diagnostics for OB stars (e.g. Walborn *et al.* 1995). Specifically strong P Cygni emission in the SiIV doublet is unambiguously indicative of an $\sim$05-B1 supergiant, rather than a lower luminosity star.

3.5.2 Comparison to other B[e] supergiants

To date only two other supergiant B[e] stars have been detected as X-ray sources; the sgB[e]-XRB IGR J16318-4848 (e.g. Filliatre and Chaty 2004; Chaty and Rahoui 2012) and the cluster member Wd1-9 (Skinner *et al.* 2006; Clark *et al.* 2008). IGR J16318-4848 shows a striking similarity to CI Cam, with a quiescent X-ray spectra best fitted with an absorbed, truncated power law and a strong Fe-Kα line. There is no evidence for the ionised iron line in the higher resolution *Suzaku* data of IGR J16318-4848 (Barragán *et al.*, 2009) suggesting that this could be unique to CI Cam. The X-ray spectrum of Wd1-9 instead demonstrates a spectrum consistent with emission from an optically thin thermal plasma ($kT \sim 2.3$keV; Clark *et al.* 2008). This is suggestive of emission from a colliding wind binary rather an accreting binary, consequently this source is not discussed further.

As discussed in Section 1.4.2.1, uncertainties in the distances to both CI Cam and IGR J16318-4848 mean that it is difficult to compare quiescent luminosities. However, results suggest that they appear broadly comparable (to within a factor of a few) under the assumption that CI Cam is located at ∼5 kpc and IGR J16318-4848 is within the 1.6-4 kpc range favoured by Chaty and Rahoui (2012) (Matt and Guainazzi 2003, Section 3.3) implying that the quiescent fluxes in both CI Cam and IGR J16318-4848 arise via a similar mechanism. Both sources have undergone X-ray "flares" with current temporal sampling suggesting that these events are rare and aperiodic; only two flares separated by ~ 9 yrs have been associated with IGR J16318-4848 (1994 and 2003; Courvoisier *et al.* 2003; Murakami *et al.* 2003) and just the one event in 1998 with CI Cam (noting that photometric observations between 1989-92 also show no evidence for flaring in this period; Clark *et al.* 2000). Moreover the peak luminosity also differs between the systems; with Filliatre and Chaty suggesting $L_X \sim 2.6 \times 10^{36}$erg s^{-1} for IGR J163818-4848 (assuming a distance of 4 kpc) compared to $L_X \sim 3 \times 10^{38}$erg s^{-1} for CI Cam (e.g. Hynes *et al.* 2002).

Both CI Cam and IGR J16318-4848 appear to be rather luminous supergiants, with comparable bolometric luminosities. Both sources also support a mid-IR excess attributed to circumstellar gas, although different modeling assumptions (optically thin/thick emission, spherical or disc geometry and composition) make direct comparison of the physical properties (e.g. inner radius, dust mass) of the dusty components difficult. The dust temperature at the inner radius of the envelope appears rather high in both cases ($\sim$ 767K for IGR J16318-4848 (Chaty and Rahoui, 2012) and $\sim$ 1550K for CI Cam (Thureau *et al.*, 2009)). The geometry of the dusty envelope has been unambiguously determined for CI Cam by Thureau *et al.* (2009), who showed that it resides in a ring or torus with inner radius ~ 8 AU (at 5 kpc). No conclusions as to the dust geometry in IGR J16318-4848 were drawn by Moon *et al.* (2007), although by analogy to other B[e] stars Chaty and Rahoui (2012) adopt a disc like geometry with inner radius $\sim$ 1 AU/kpc. If the ∼19.3 day orbital period Barsukova *et al.* (2006) propose for CI Cam is confirmed, the binary would also lie interior to the dusty disc mapped by Thureau *et al.* (2009). Unfortunately no orbital period is known for IGR J16318-4848.

3.6 Conclusions

We have presented a detailed analysis of the spectral and timing properties of XTE J0421+560/CI Cam. The continuum of the spectrum is well described by a heavily absorbed ($N_H = (4.4 \pm 0.5) \times 10^{23}\mathrm{cm}^{-2}$) power law with photon index consistent with those seen in neutron star BeXRBs ($\Gamma = 1.0 \pm 0.2$). We also attempted to fit the white dwarf model of Ishida *et al.* (2004) but could not achieve an acceptable fit or sensible model parameters. The apparently broad iron line has been decomposed into three, intrinsically narrow lines, neutral Fe-Kα and Kβ and almost completely ionised FeXXV Kα, suggesting multiple emitting regions. The quiescent spectrum seems to point to a neutron star or black hole accretor, however this is inconsistent with the X-ray activity of the system. I cannot suggest a mechanism for the large X-ray flare seen in 1998.

Further observations of XTE J0421+560/CI Cam of increased duration are required to confirm or refute the presence of the lag suggested in this Chapter. Better quality data could be used to solve the transfer equation and could be used to explore the possibility of a lag between the neutral and ionised Fe-Kα emission, both of which are beyond the scope of this work. Better constraints on other system parameters, such as distance, inclination and system mass, would also help to constrain the geometry of this unusual system using this method.

"Have you any idea how much damage that bulldozer would
suffer if I just let it roll straight over you?"
"How much?"
"None at all,"

THE HITCHHIKER'S GUIDE TO THE GALAXY (1979)

4

The Search for High Mass X-ray Binaries in the Phoenix Dwarf Galaxy

In this Chapter I report on the first X-ray images of the Phoenix dwarf galaxy, taken with *XMM-Newton* in July 2009. This local group dwarf galaxy shares similarities with the Small Magellanic Cloud (SMC) including a burst of star formation $\sim$50 Myr ago. I investigated the possibility of an HMXB population in Phoenix with the intention of furthering the understanding of the HMXB-star formation rate relation. The data from the combined European Photon Imaging Cameras (EPIC) were used to distinguish between different source classes (foreground stars, background galaxies, AGN and supernova remnants) using EPIC hardness ratios and correlations with optical and radio catalogues. Of the 81 X-ray sources in the field of view, six are foreground stars, four are galaxies and one is an AGN. The remaining sources with optical counterparts have $\log(\frac{f_X}{f_{opt}})$ consistent with AGN in the local universe. There is nothing to suggest the presence of an HMXB population at this time. The existence of any persistent XRB (i.e. an sgXRB) can be ruled out, while the transient nature of the BeXRBs mean that a possible population of these sources cannot be discounted, but I conclude that it cannot be extensive.

4.1 Introduction

The Phoenix dwarf galaxy was discovered in 1976 by Schuster and West who described it as a very distant ($\sim$100 kpc) globular cluster. It was later identified as a dwarf irregular galaxy (dIrr) by Canterna and Flower (1977). These galaxies are HI rich and show obvious signs of recent star formation. Despite this classification, Phoenix has characteristics of a dwarf spheroid galaxy (dSph) and it has been suggested that it belongs to an intermediate class of galaxy between the dwarf spheroidal and dwarf irregular, along with three other dwarf galaxies (Pegasus, Pisces (LGS3) and Antila). The distance to Phoenix has been determined to be $\sim$420 kpc using a variety of different methods and data sets (for example see van de Rydt *et al.* 1991; Martínez-Delgado *et al.* 1999 and, more recently, Menzies *et al.* 2008) placing Phoenix well within the Local Group.

The HI gas surrounding Phoenix was mapped by Young et al. (1997; 2007) using the VLA. They identified several regions in the immediate vicinity with a variety of shapes and velocities. One such cloud, located $\sim$5 arcmin south west of the main stellar body, has been unequivocally associated with Phoenix based on the excellent agreement of the radial velocities of the stars, obtained from stellar spectra (Irwin and Tolstoy, 2002) from the VLT, and the velocity of the HI cloud. Young *et al.* (2007) recognise that this offset suggests that Phoenix could offer a unique opportunity to study the possible mechanisms responsible for gas removal in dwarf galaxies, transforming a gas-rich dIrr into a gas-poor dSph.

Extensive optical data of the central region of Phoenix also exist: the Wide Field Planetary Camera (WFPC2) onboard *HST* has imaged the central field of the galaxy with both F814W and F555W filters (for example see Holtzman *et al.* 2000 and Hidalgo *et al.* 2009, hereafter H09). Young *et al.* (2007) use both of these data sets to derive separate star formation histories for the eastern and western sides of Phoenix. They report an asymmetry in the star formation rate across the face of the galaxy, in agreement with Martínez-Delgado *et al.* (1999). The western side of Phoenix displays evidence for strong episodes of star formation at 180 and 40 Myr ago whilst the eastern side shows evidence for more continual star formation from 250 to 50 Myr ago. They note that this is consistent with the HI location, offset to the west of the galaxy's optical emission. These epochs of star formation are similar to those for another dIrr galaxy: the SMC (Section 1.5.1). In fact, the Phoenix dwarf galaxy shares many other common features with the SMC, including its low metallicity (Z=0.004 for the SMC, Russell and Dopita 1992; Z=0.0015 for Phoenix, H09).

Table 4.1: *XMM-Newton* EPIC observations of the Phoenix galaxy on July 7, 2009

Camera	Filter	Read out Mode	Observation MJD	Start	End(UT)	Exp. (ks)
MOS1/2	Medium	Full Frame	55019.4	08:13	21:11	46.6
pn	Thin1	Full Frame		08:36	21:06	45.0

The relationship between the number of LMXBs and the host galaxy mass was briefly mentioned in Chapter 1. The low mass Local Group dwarf galaxies like Phoenix (3.3×10^7 $M_\odot$, Mateo 1998), which are not massive enough to harbour LMXBs, are ideal for probing the HMXB - star formation relation in the low luminosity limit. The most recent epoch of star formation in Phoenix had a SFR of $2.5 \pm 1.8 \times 10^{-5}$ $M_\odot$ yr^{-1}arcmin^{-2} (Young *et al.* 2007 compared with $8.1 \pm 1.4 \times 10^{-5}$ to $1.5 \pm 0.6 \times 10^{-5}$ $M_\odot$ yr^{-1}arcmin^{-2} depending on the area of the SMC, Antoniou *et al.* 2010). It is only by probing galaxies across a broad spectrum of mass, star formation history, and chemical composition that astronomers can establish both trends in the HMXB populations of these galaxies and understand the significance of these objects as tracers of star formation.

4.2 Observations and Data Reduction

The first X-ray images of the Phoenix dwarf galaxy were taken with *XMM-Newton* during the satellite revolution #1754 on July 7, 2009. Table 4.1 summarises the details of the EPIC observations. The data were processed using the *XMM-Newton* SAS v9.0 along with software packages from FTOOLS v6.8.

As in the previous Chapters, the MOS and pn observational data files were processed following the procedure detailed in Section 2.2.2. Periods of high background activity were screened by removing any times when the single pixel pattern count rate above 10 keV was $>$0.8 cts s^{-1} for the MOS detectors and $>$2.0 cts s^{-1} for the pn detector. The filtered event files were then split into five energy bands: (0.2–0.5), (0.5–1.0), (1.0–2.0), (2.0–4.5) and (4.5–12.0) keV to identify and discriminate between hard and soft sources in the field of view. For the pn detector, only the single (PATTERN=0) pixel event patterns were selected in the range 0.2–0.5 keV, for all the other bands single and double (PATTERN$\leq$4) pixel events were accepted. For the MOS, single to quadruple (PATTERN$\leq$12) pixel events were selected.

Four of the X-ray brightest sources (for exact details on which sources, see Sec-

tion 4.4) were identified with >500 counts in the full energy range (0.2–12.0 keV) across all three detectors and were subject to further spectral analysis. Eregionanalyse suggested extraction regions with radius ~ 20 arcsec for all 4 sources, thus this value was adopted for all sources extraction regions. Light curves and spectra were extracted from several background regions (with radius 60 arcsec) and examined to confirm that they were statistically identical. The same background region was used for all the MOS spectra, as all the sources fell on the central CCD. For the pn detector, regions on neighbouring chips which contained no sources were identified and again were confirmed to be statistically identical. The spectrum from the closest region to a source was then used as the background spectrum.

4.2.1 Source Detection with *XMM-Newton*

Detecting sources in an *XMM-Newton* data set involves several stages as detailed below:

1. **Exposure map creation with eexpmap.**. Exposure maps contain all the information on the spatial efficiency of the instruments, which reduces with increasing off axis angle. This is energy dependent and so is run on all 15 images (3 detectors, 5 energy bands).

2. **Detection mask creation with emask.** Detection masks identify the areas where the source detection need not be performed (e.g. chip gaps and bad pixels).

3. **Sliding box source detection in local mode with eboxdetect.** This is run on all 15 images simultaneously. A 3×3 pixel box is moved across the image and the total number of counts within the box is calculated. The background is then taken from a 7×7 box centred on the same pixel, excluding the central 3×3 region. If the net counts are greater than zero, then the detection likelihood, L, is given by $L = -\ln p$ where p is the probability that the observed counts were caused by Poissonian fluctuations. Locations with a detection likelihood over a user defined threshold value (in this case, 10) are considered sources.

4. **Background map creation with espline.** This task removes the preliminary sources located in the previous step from the images. The background map is then created by fitting spline functions to the image (minus sources).

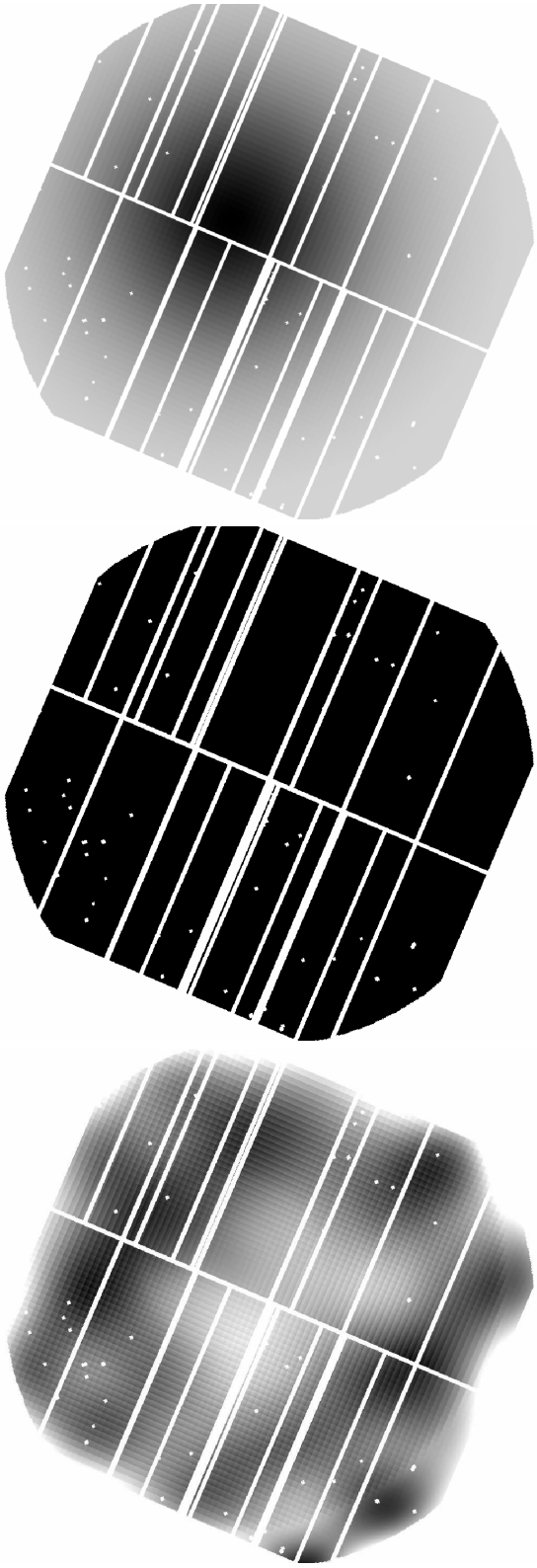

Figure 4.1: From top to bottom, the exposure map, detection mask and background map of the pn image in the 4.5-12.0 keV energy range.

5. **Sliding box source detection in map mode with eboxdetect.** As in Step 3, source counts are calculated from a 3×3 (or 5×5) pixel window. However, rather than calculating the background from the surrounding pixels, it is now determined from the background map. This improves the detection sensitivity.

6. **Maximum likelihood fitting with emldetect.** This takes the source location list, created in the previous step, and fits the detector point spread function (PSF) to the source count distribution, optimising the source centering. The source position is constrained to be the same for all 15 images.

Examples of an exposure map, detection mask and background map from this observation are shown in Figure 4.1.

The maximum likelihood fitting yielded 90 sources in the field of view, each with a total detection likelihood larger than 10. This corresponds to a probability of a source being a spurious detection of $\sim 5 \times 10^{-5}$ in a single image, and 3×10^{-6} for the case of simultaneously using 15 images. The PSF of the pn detector is comparable to the angular size of the pixels (6.6” versus 4.1”). Oversampling the PSF allows for better discrimination between real sources and any remaining bad pixels or columns as real sources increase in size with more oversampling. As such, the data were screened by eye to remove obvious false detections caused by instrumental effects, resulting in a final list of 81 sources.

To convert source count rates into flux values, the energy conversion factors (ECFs) from the *XMM-Newton* Serendipitous Source catalogue (Watson *et al.*, 2009) were used. Whilst these ECFs do assume a spectrum typical for an AGN with low absorption, Pietsch *et al.* (2004, hereafter P04) show that the ECFs calculated for a typical supernova remnant (an absorbed 1 keV thin thermal spectrum) and supersoft source (absorbed 30 eV black body spectrum) in M33 only vary from those calculated for a typical hard source by about 20% for both EPIC detectors. The flux values calculated using the ECFs are used in source classification (see Section 4.3) over a broad energy range (0.2–4.5 keV, bands 1–4) to be consistent with the findings of Maccacaro *et al.* (1988) and the method of P04. A large deviation from a power law spectrum would be required for these results to be inadequate over such a range. The flux values for band 5 are calculated, but are not used in the source classification.

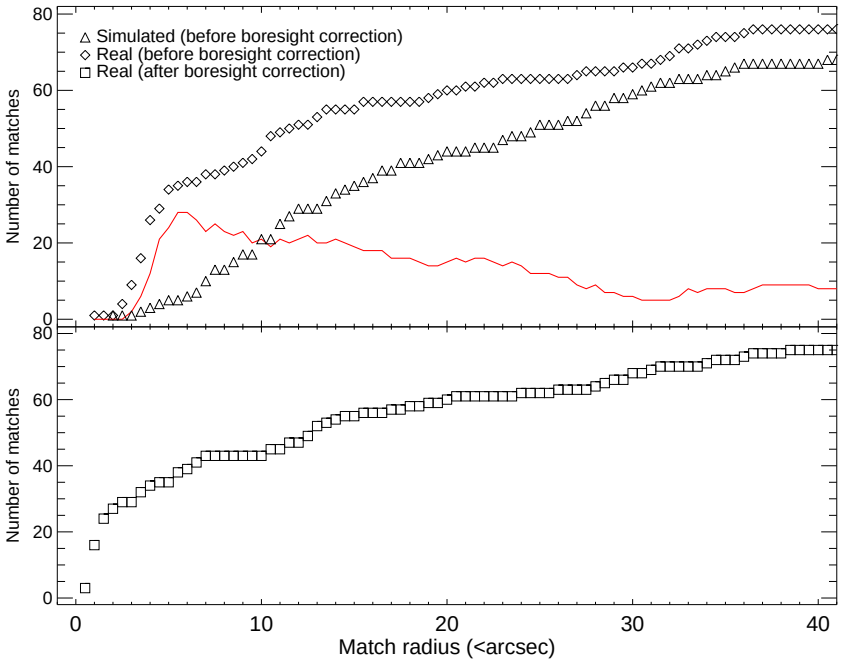

Figure 4.2: The top panel shows the cumulative number of matches as a function of search radius between the LGGS catalogue and the positions of the X-ray sources (diamonds). The number of matches between the X-ray positions and the simulated optical catalogue are also plotted (triangles). The solid red line is the difference between these two values. The bottom panel shows the number of matches between the LGGS catalogue and the boresight corrected X-ray positions, shown for comparison (squares).

4.3 Source Classification

The positions of the 81 X-ray sources in Phoenix were cross-correlated with the Local Group Galaxy Survey (LGGS, Massey *et al.* 2007) catalogue and the separation to the nearest optical match calculated. This was compared with the number of matches found with a simulated catalogue. The simulated positions were generated by independently reassigning both the right ascensions and declinations of all the optical sources. Figure 4.2 shows the results of the correlations as a function of search radius. The solid line shows the difference between the number of X-ray sources matched with the real catalogue and the number matched with the simulated catalogue. The radius at which the number of real matches increases at the same rate as the number of simulated matches, i.e. the radius at which the solid line plateaus, can be considered as the maximum search radius. At radii greater than this value, all matches with the real catalogue are false associations. The figure indicates that this occurs at about 6 arcsec.

The source classification described in this section was performed in two stages. The SIMBAD and NED archives and the LGGS and United States Naval Observatory-B1.0 (USNO B1.0, Monet *et al.* 2003) catalogues were searched for correlations around the X-ray source positions. The preliminary classification used a search radius of up to 6 arcsec for all sources. This was primarily to identify galaxies and AGN for an astrometric boresight correction. Foreground stars were purposely not used when performing the boresight correction due to the possibility of proper motion. The four galaxies and possible AGN listed in section 4.4.2 identified from the SIMBAD and NED databases were used along with the SAS task eposcorr to obtain accurate positions for all the sources. The final boresight correction was 4.7 ± 1.5 arcsec. The bottom panel of Figure 4.2 shows the number of matches between the corrected X-ray positions and the LGGS catalogue for comparison. The gradient of the curve decreases dramatically after 2 arcsec indicating that the boresight correction has been successful and that the error on the X-ray source positions are dominated by the error the required co-ordinate shift. This error is added quadratically to the statistical error derived in the source detection. The classification was then performed for a second time, using the individual 3σ error circles as the search radius for each source. Figure 4.3 shows the combined EPIC image in the 0.2-4.5 keV energy range with HI contours from Young *et al.* (2007) superimposed. Also shown in this figure is the combined *RVB* band optical image from the Local Group Galaxy Survey (LGGS) image (Massey *et al.*, 2007). The positions of the sources detected by the analysis are also displayed (the boresight corrected positions on the optical image, the uncorrected positions on the X-ray image) along with a unique identification number for each source.

In order to locate any candidate HMXBs in Phoenix, it is necessary to identify as many of the foreground stars and background sources in the field of view as possible. Following the method of P04 I attempt to identify or classify all the X-ray sources in the field of view as either foreground stars (fg stars), AGN, galaxies (GAL), Super-soft Sources (SSS), Supernova Remnants (SNR) or hard sources (which could be HMXBs or unidentified AGN).

P04 use the hardness ratios (HRs) of the sources (both known and unknown) in M33 to create X-ray colour plots and identify areas corresponding to specific source classes. The limitations of this method of source classification are discussed in detail in P04, the main drawback being that sources with similar spectra (e.g. foreground stars and supernova remnants; HMXBs and AGN) cannot be differentiated when the statistics are low. An alternative to HR classification is the quantile analysis technique of Hong *et al.* (2004), however this is not suit-

able for *XMM-Newton* data due to the high background. The HRs were defined as $HR_i = (B_{i+1} - B_i)/(B_{i+1} + B_i)$ where B_i is the count rate in energy band i. The bands are the same as those used in the source detection: (0.2–0.5), (0.5–1.0), (1.0–2.0), (2.0–4.5) and (4.5–12.0) keV. To improve the statistics, the counts from all three EPIC instruments were combined before HRs are calculated. The hydrogen column density in the direction of M33 is a factor of 4 greater than towards Phoenix (1.5×10^{21} cm^{-2} for Phoenix and 6×10^{21} cm^{-2} for M33, Dickey and Lockman 1990). Phoenix does not have the considerable X-ray coverage of M33 and so I did not attempt to derive new HR criteria. Instead I simulated the model spectra used by P04 to derive their HR criteria, using the XSPEC command FAKEIT, to confirm that they are valid for this work despite the different column densities. Modifications were made where appropriate.

The modified and original P04 criteria used for source classification are summarised in Table 4.2. Where only one set of criteria are presented, no changes have been made to the original criteria. Where two sets of criteria are presented, the original criteria from P04 are listed underneath the modified criteria in italics. Figure 4.4 shows the X-ray hardness ratio plots for all the X-ray sources in Phoenix.

For sources such as foreground stars, galaxies and AGN, it is the additional information at other wavelengths that drives the classification and not the X-ray HRs. Foreground stars are classified based on the ratio of X-ray to optical flux, calculated using their magnitudes given by $\log(\frac{f_X}{f_{opt}}) = log(f_X) + (m_V/2.5) + 5.37$ following Maccacaro *et al.* (1988). If V-band magnitude information was not available, the average of the m_B and m_R values were used in place of the m_V. The distances to all but a handful of stars in our own Galaxy are unknown, making it difficult to assess the level of extinction for an individual foreground star, regardless of the pointing direction. As such, no modifications were made to the HR criteria for foreground stars.

The HR2$<$0 criterion for a galaxy classification is a constraint applied when an association was made between a galaxy and one of the X-ray sources. It is primarily to distinguish between a galaxy without an active nucleus and an AGN with a much harder spectrum. There is a smooth transition between the two classifications depending on the relative contributions of star formation and the activity of the central black hole.

The HR criteria are more important for hard sources, supernova remnants and super-soft sources, where no other information is used in the classification. Super-soft sources are generally accepted to be white dwarf systems burning hydrogen on their surface. Any super-soft sources in Phoenix will reside in the bottom left-hand

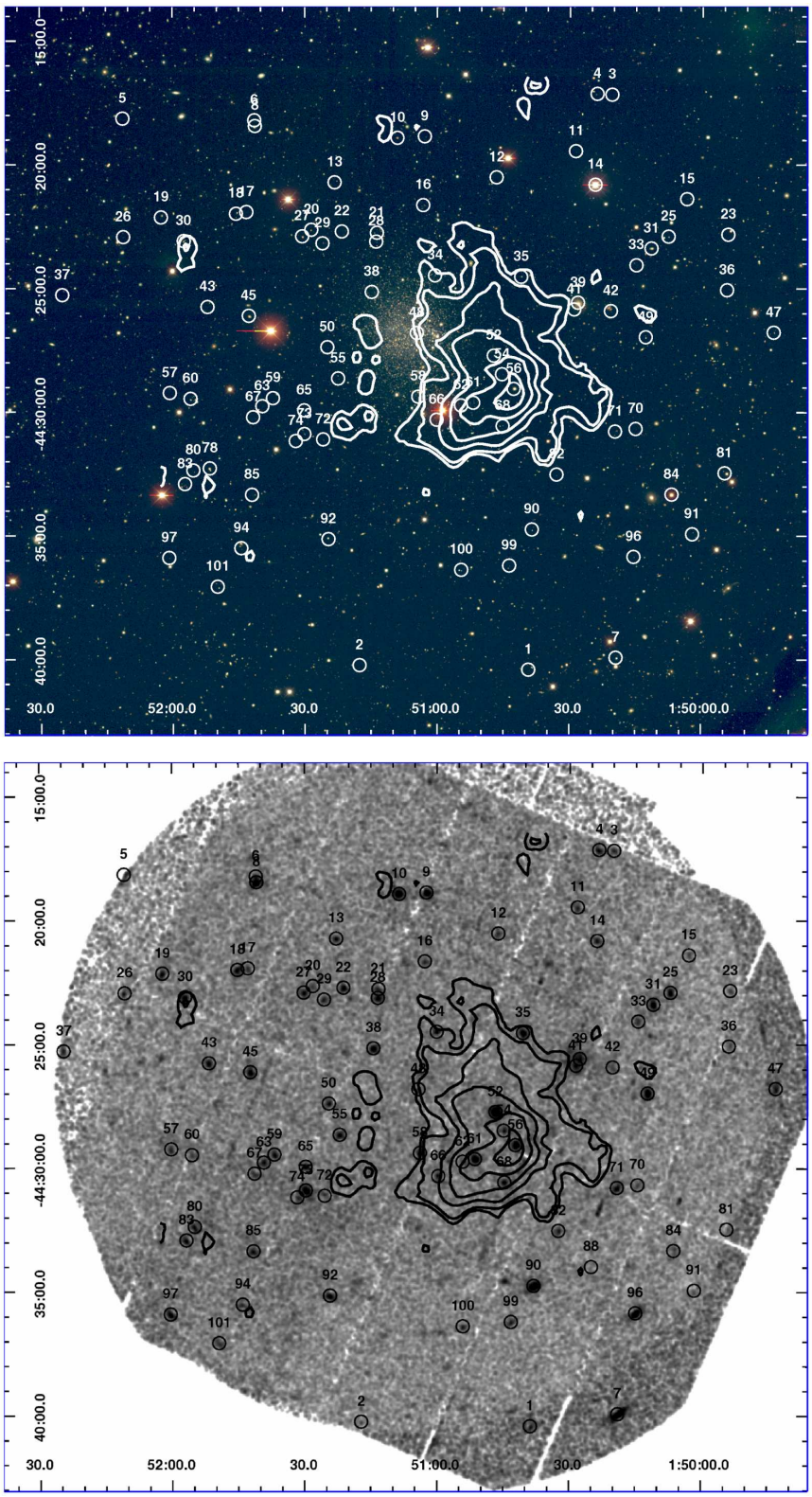

Figure 4.3: Top panel shows the optical Local Group Galaxy Survey (LGGS) image, the bottom panel shows the combined 0.2-4.5 keV EPIC data. HI contours from Young *et al.* (2007) are overlaid on both images. The contour levels correspond to column densities $(0.5, 1, 2, 3, 4, 5) \times 10^{19}$ cm^{-2}. The circles are the positions of the sources detected by the box sliding and maximum likelihood detection analysis, they are not indicative of the size of the error circles and are illustrative only.

Table 4.2: Summary of criteria, identifications and classifications, for more details see text. EHR2 is the error on HR2.

Source Type	Selection Criteria	Identified	Classified
fg star	$\log(\frac{f_X}{f_{opt}})$< -1.0 and HR2<0.3 and HR3<-0.4 or not defined	5	1
SNR	HR1>0.1 and HR2<-0.4 and not a fg star		
AGN	Radio source and classified hard		1
GAL	optical id with a galaxy and HR2<0.0	1	3
SSS	HR1<-0.2, HR2-EHR2<-0.99 or HR2 not defined, HR3 and HR4 not defined		
hard	HR2-EHR2>-0.3 or only HR3 and HR4 defined and no other classification		50
	HR2-EHR2>-0.2 or only HR3 and HR4 defined and no other classification		*48*

corner of the top panel of the HR plots (see Figure 4.4). HRs were calculated for typical super-soft sources (absorbed 30 eV and 50 eV blackbodies) over a range of column densities (10^{19}–10^{21} cm^{-2}) to see how the difference in the column density to M33 and Phoenix affects the HR values. All the HRs calculated were well within the original HR limits and so the criteria were left unchanged.

The spectra of supernova remnants are very similar to those of foreground stars. Following P04, I assumed that all foreground stars have been identified from the correlation with optical data leaving any remaining sources that fit the HR criteria as supernova remnant candidates. Again, HRs were calculated for typical supernova remnant spectra (absorbed thermal plasma models with temperatures of 0.5 keV and 1.0 keV) over the same range of column densities as before. All the HRs calculated were within the original criteria and so the criteria were not modified.

The hard classification is arguably the most important for this work. Sources classified as hard are believed to be either unidentified AGN or HMXBs, both of which have absorbed power law spectra. HRs were calculated for an absorbed power law spectrum over a range of column densities (10^{19}–10^{21} cm^{-2}) and photon indices (0.6–3.0). Only the very steepest photon indices ($\geq$2.8) with low absorption ($\leq 2 \times 10^{20}$ cm^{-2}) did not fit the hard criterion. Such spectra would imply an AGN with very low intrinsic absorption. The criterion for hard sources were adjusted so that all photon indices with galactic absorption or greater are classified hard.

4.4 Source List

The X-ray hardness ratios of all sources in the field of view are displayed in Figure 4.4. The red squares are the 5 sources that are identified in Section 4.5 for further analysis. The black diamonds are the other 76 sources in the field of view. The hardness ratio criteria are also displayed. Only two X-ray sources have a SIMBAD object within their error circle, five matches were found within the NED database, 35 matches in the LGGS catalogue and a further 3 sources in the USNO-B1 catalogue. The criteria used for source classification are summarised in Table 4.2. It is important to note that the source classifications suggested here should be regarded as the proposed nature of the source. The original criteria were derived using the overall properties of large sample populations and not individual sources, consequently some characteristics of subclasses and sources are not accounted for, such as the X-ray soft, narrow line Seyfert I galaxies, and rare events like stellar flares. A source is *"identified"* if it meets all the criteria for a particular group and is *"clas-*

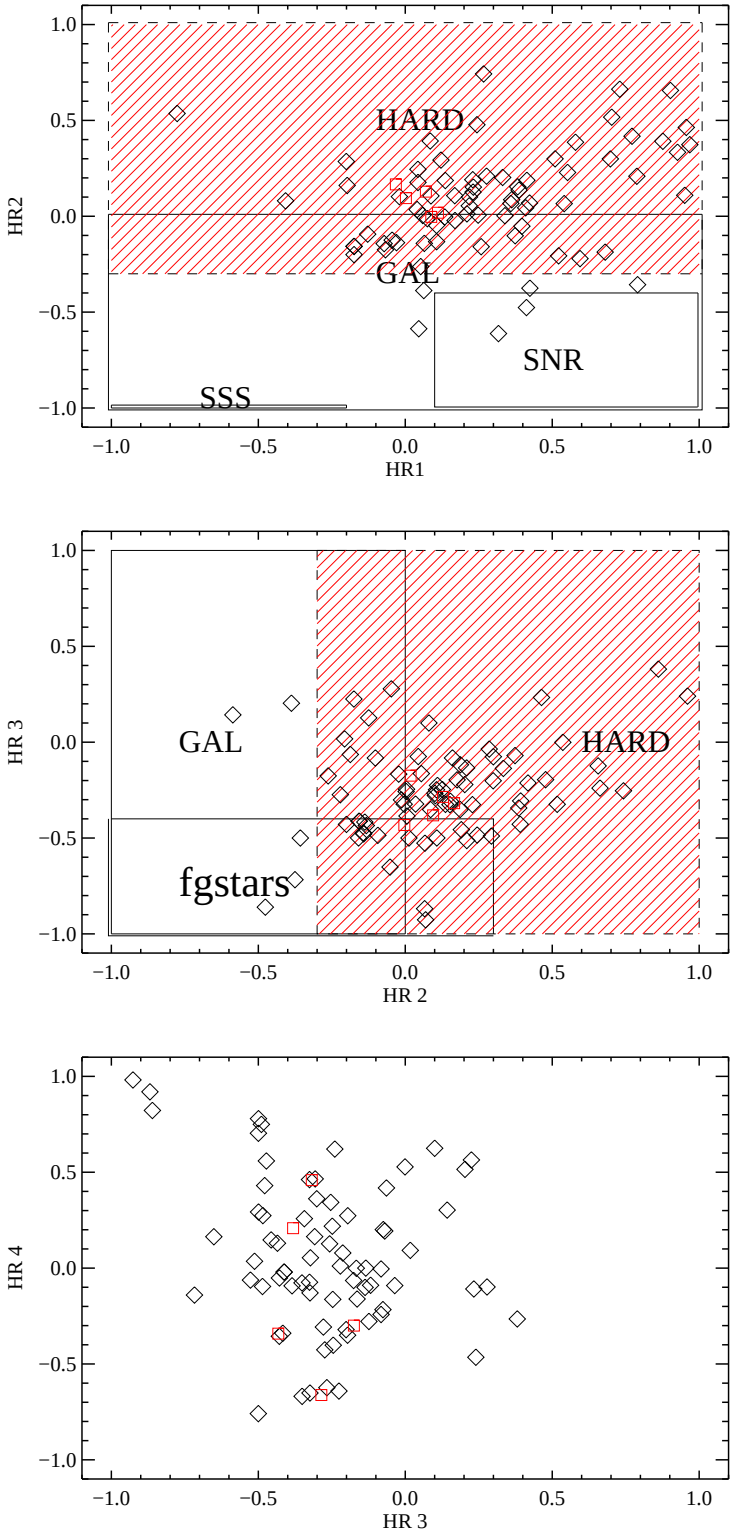

Figure 4.4: X-ray hardness ratios for all sources in the field of view. The regions marked on the plots show the hardness ratio criteria for the different objects. For objects such as galaxies and foreground stars, it is the information gained at other wavelengths that drives the classification. The errors are not shown for clarity. The red squares are the five sources discussed in Section 4.5.

sified" if it meets the majority of the criteria. Nineteen sources remain unclassified. The source classifications of all the sources in the field of view can be found in Appendix A.

4.4.1 Foreground stars

Foreground stars are expected to lie in the lower left corner of the HR3/HR2 plot (middle panel of Figure 4.4). Of the 38 X-ray sources in the field of view with an LGGS or USNO counterpart, one source (#14) was positively identified as a star from the SIMBAD database and another source (#56) from the NOMAD catalogue (Zacharias *et al.*, 2004). A further two sources (#27 and #99) were identified as stars based on the optical information available in the LGGS and USNO catalogues.

Sources #78 and #84 both have $\log(\frac{f_X}{f_{opt}})$ indicating a stellar classification, but only source #78 fits the hardness ratio criteria within errors so is also identified as a foreground star. Source #84's HR3 value is greater than the -0.4 required for classification. The optical counterpart is listed in the NOMAD catalogue as being a 14th magnitude star with colours consistent with being a late K/early M type star. The ratio of X-ray to optical flux is also consistent with a K or M type star. I have already stressed in Section 4.3 that for foreground stars, it is the information at other wavelengths that drives the classification. Despite the fact that the HR3 value does not fit the criterion, I feel that the strong agreement of the X-ray to optical flux value and the optical colours warrants a stellar classification. As such source #84 is classified as a foreground star.

4.4.2 Galaxies and AGN

The X-ray spectrum of a galaxy without an active nucleus is softer than that of a galaxy with an AGN, and so will reside in the lower and left hand side of the HR1/HR2 and HR2/HR3 plots in Figure 4.4. Cross correlation with the SIMBAD database identified one source, #39, with a known galaxy in the field of view just outside the HI cloud. This corresponds to SUMSSJ015027.5-442537 at z=0.13. Four more X-ray sources (#10, #31, #43 and #60) have NED objects in their error circles. #10, #31, and #60 all fit the X-ray HR criteria for galaxies. #43 is not a galaxy, but listed as an unclassified extragalactic candidate within NED, detected in the radio band. The X-ray source just fits the criteria for a hard source and as such, #43 is classified as an AGN.

4.4.3 Super-soft Sources and Supernova Remnants

The area of Figure 4.4 where the super-soft sources should reside (bottom left-hand corner of the top panel) is remarkably empty. I do not identify or classify any sources as super-soft sources in the field of view. Supernova remnants are expected to fall in the area of the same plot marked SNR. Only two sources fit these HR criteria. They are #14 and #27, two identified foreground stars. As I am confident in the assessment of these sources, I don't find evidence for any SNR in the data.

4.4.4 Extended sources

Five sources were found to have some measurable extent, these were #36, #41, #81, #91 and #101. With the exception of source #41, these sources are all found on the edge of the field of view and close to a pn chip border. It is more likely that the elongation of the off-axis point spread function (PSF) is not well accounted for at these locations. #41 is in very close proximity to #39, the galaxy identified in the SIMBAD database and discussed in Section 4.4.2. The source has an extent of 5.7 ± 0.2 pixels, which corresponds to 23.4 arcsec on the sky, greater than the separation of #41 and #39 (around $\sim$19 arcsec). Along with #39, #41 appears to be embedded within a single extended source in the X-ray image. It is likely that these two sources are in fact part of one extended source.

4.5 HMXB candidates

Of the 81 sources in the field of view, only one source, #48, is coincident with the optical emission of the galaxy. Interestingly some of the brightest sources in the field of view are offset from the optical emission and spatially coincident with the HI region. Eleven sources (#34, #35, #48, #52, #54, #56, #58, #61, #62, #66 and #68) lie within the lowest HI contour shown in Figure 4.3. The recent bursts of star formation in the western side of the galaxy means that the location of these sources is compatible with a possible HMXB population. Source #56 is the only identified source in this list. Five sources (#34, #35, #52, #61 and #68) have appreciable X-ray emission above 2 keV (with flux values $> 8 \times 10^{-15}$ erg cm^{-2} s^{-1}) and occupy an area of $<$40 square arcminutes. Their HRs are shown by red squares in Figure 4.4. Synthesis models of the cosmic X-ray background by Treister and Urry (2006) and Gilli *et al.* (2007) suggest that $\sim 2.3^{+1.2}_{-1.9}$ background sources will be detected in this energy range and in an area this size. The errors stated are the 90% confidence lim-

its. Whilst five is not an obvious excess over the predicted background numbers, I feel these sources warrant further investigation, particularly as the expected number of HMXBs in Phoenix is small.

Temporal and further spectral analysis are required to distinguish between HMXBs and as yet unidentified AGN. No other X-ray data are available for Phoenix, so I cannot draw comparisons between my results and past observations, but power spectra created from the entire (non GTI filtered) light curves for all five of these sources showed no evidence for pulsations.One thousand fake pulsar lightcurves were generated by adding a sinusoid with a period of 100 s to a constant equal to the background subtracted count rate of the brightest source. The light curves have an amplitude corresponding to a pulsed fraction of 0.3 (the typical value quoted for HMXBs in the SMC, Coe *et al.* 2010). Random noise was added to every point in the light curve using the IDL program poidev[1], ensuring that the total number of counts in the light curve was conserved. The simulated light curves were then binned with the same bin time as the real light curves. When Lomb-Scargle analysis was performed, only 46 of the 1000 light curves resulted in a significant detection (a 5σ detection according to the formula of Horne and Baliunas 1986). An unrealistically high pulsed fraction of 0.6 is required to consistently produce a significant result at 100s with a count rate equal to that of the brightest HMXB candidate. Thus it can be concluded that these observations do not have the sensitivity to detect pulsations from a typical pulsar in Phoenix using this method.

EPIC spectra were extracted between 200 eV and 10 keV for the five sources listed above and were fit with an absorbed powerlaw (*phabs*vphabs*powerlaw*) model. The *phabs* component is fixed at 1.5×10^{20} cm^{-2} (Dickey and Lockman, 1990) for galactic foreground absorption with elemental abundances from Wilms *et al.* (2000). The *vphabs* component accounts for absorption in Phoenix and is a free parameter with metal abundances reduced to 0.075, calculated from values given in H09. Throughout the investigation XSPEC version 12.6.0 was used. Table 4.3 contains the best fit parameters with 90% confidence errors.

As discussed in Section 1.5.3, the spectral distribution of BeXRBs in the SMC is consistent with that of the Milky Way, despite the very different environment. Thus it seems reasonable to assume that any BeXRB in Phoenix will fall in the same range of spectral classes (O9V-B2V). Taking the M_V magnitudes from the stellar flux library of Pickles (1998) and scaling them with the distance to Phoenix predicts V-band magnitudes in the range 18.7-21.2. These values include an A_V

[1]http://idlastro.gsfc.nasa.gov/ftp/pro/math/poidev.pro

extinction value of 0.062 mags (H09). The distance modulus to Phoenix, 23.1, has an error of $\pm$0.1 (H09) which leads to the same error on the magnitudes calculated for BeXRBs in Phoenix. Similarly, if it is assumed that any sgXRB present will also fall into the same range of spectral classes as those already discovered in our own galaxy and beyond (O8.5I-B3I; Liu *et al.* 2006) and scale to the distance of Phoenix, they will have *V*-band magnitudes in the range 16.1-16.7 $\pm$0.1. When searching for HMXB candidates in the SMC, Shtykovskiy and Gilfanov (2005) required that the optical colours of the companion star were $B-V<0.20$. I adopt the same criteria for this work, but take into account the different levels of extinction between the SMC and Phoenix (Rieke and Lebofsky, 1985). This leads to the constraint that $B-V<0.14$ for any optical counterparts.

Black hole X-ray binaries can exist in several states, the high/soft state, the low/hard state and the quiescent state (which can be considered to be a special case of the low/hard state; Kong *et al.* 2002). The mass of Phoenix is too low for an LMXB population, but no such restriction applies to the high mass black hole systems. The observations are not deep enough to see any quiescent black hole binaries in Phoenix, which would have a flux of about $\sim 5\times10^{-17}$ erg cm^{-2} s^{-1}(Lewin and van der Klis, 2006). The luminosity of the high/soft state is typically seen around 10% of the Eddington luminosity (Nowak, 1995), for a 6M$_{\odot}$ black hole at the distance of Phoenix, this is $\sim 8\times10^{37}$ erg s^{-1} corresponding to a flux of $\sim 4\times10^{-12}$ erg cm^{-2} s^{-1}. This is an order of magnitude brighter than even the brightest source in the field of view. Consquently, any black hole binaries present in the data set must be in the low/hard state, which is charactised by a power law spectrum with a photon index $\sim$1.7 and a luminosity around $\sim$2% Eddington or less (Lewin and van der Klis, 2006; Maccarone, 2003). In the X-ray band, BeXRBs typically have photon indices of $\leq$1.4 (see Section 1.4.3).

4.5.1 Source #34

Source #34 is one of the two spectra with lower signal and as such the parameters for the model fit are not well constrained. The photon index of $1.9^{+0.4}_{-0.3}$ rules out the possibility that #34 is a BeXRB but is consistent with a black hole XRB in Phoenix. The large uncertainty in the parameters and the relatively poor fit means that this should be treated with caution. The optical counterpart is too faint and red for an early type star (m_V=21.5, $B-V$=0.23). Source #34 is most likely an AGN.

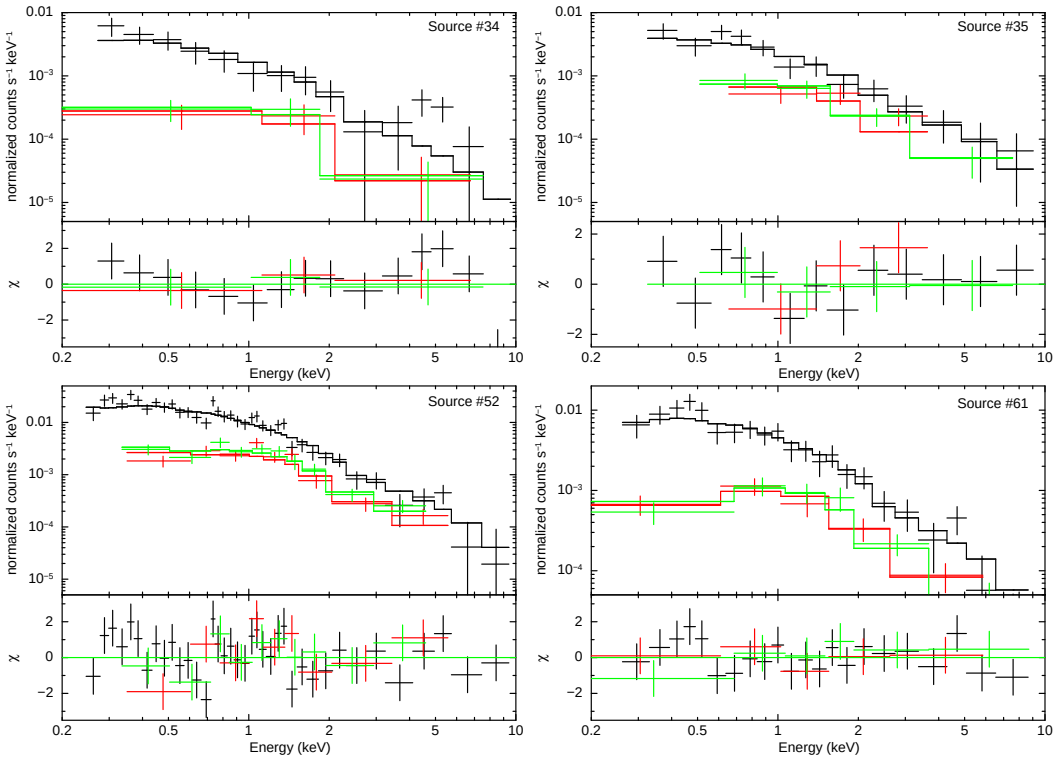

Figure 4.5: X-ray spectra of four of the sources in the H I region and their best fit models.

4.5.2 Source #35

The X-ray spectrum of source #35 suffers from the same low signal problems as #34. The photon index ($1.6^{+0.3}_{-0.2}$) is just consistent with that of a neutron star in a BeXRB but comfortably within the range of indices seen for black hole binaries and AGN. The optical counterpart has m_V consistent with a B-type star in Phoenix, but is well outside the acceptable colour range. as with #34, #35 is probably an AGN.

4.5.3 Source #52

The photon index of #52 (2.1 ± 0.1) is too soft for even a black hole XRB, and so source #52 is almost certainly an AGN. The optical information for this source supports this as again, it is far too red for an early type star in Phoenix ($B-V$=0.21 ± 0.01).

4.5.4 Source #61

Source #61 has the greatest X-ray to optical luminosity ratio of the sample and the second greatest in the entire field of view (source #28 has a slightly greater $\log(\frac{f_X}{f_{opt}})$ value, but is located further from the optical centre of Phoenix and on the eastern

Table 4.3: Properties of the sources detected in the HI region. Fluxes are from the model fits in the 0.2–10 keV energy range. For #68, this information isn't available and so the 0.2–12.0 keV flux from the source detection is reported. Ratio of X-ray to optical value has been calculated following the method of Maccacaro *et al.* (1988) using the flux values from the model fit where possible.

ID	RA J2000	Dec J2000	$err_{1\sigma}$ arcsec	HR1	HR2	HR3	HR4
35	01:50:41.0	-44:24:32.9	1.5	0.11±0.06	0.02±0.06	-0.17±0.06	-0.30±0.09
68	01:50:45.2	-44:30:34.7	1.6	0.0±0.1	0.17±0.09	-0.3±0.1	0.46±0.09
52	01:50:47.2	-44:27:44.2	1.5	0.09±0.03	0.00±0.03	-0.43±0.03	-0.34±0.06
61	01:50:51.8	-44:29:38.4	1.5	0.07±0.05	0.13±0.04	-0.29±0.05	-0.7±0.1
34	01:51:00.5	-44:24:29.7	1.6	0.00±0.09	0.09±0.08	-0.4±0.1	0.2±0.2

	N_H 10^{20} cm^{-2}	Γ	Flux erg cm^{-2} s^{-1}	χ^2_r/d.o.f	m_V	B-V	$\log(\frac{f_X}{f_{opt}})$
35	0^{+82}	$1.6^{+0.3}_{-0.2}$	1.9×10^{-14}	0.84/15	19.93±0.01	0.44±0.01	-0.38
68			$6.3\pm0.7\times10^{-14}$		21.22±0.02	0.28±0.02	-0.12
52	$5.2^{+5.2}_{-3.7}$	2.1±0.1	6.5×10^{-14}	1.21/54	19.49±0.01	0.21±0.01	-0.14
61	$5.2^{12.6}_{-5.2}$	1.8±0.2	3.8×10^{-14}	0.63/28	21.63±0.02	0.51±0.04	0.42
34	0^{+13}	$1.9^{+0.4}_{-0.3}$	1.2×10^{-14}	1.58/16	21.47±0.02	0.23±0.04	-0.12

side of the galaxy). The photon index (1.8 ± 0.2) is consistent with a black hole XRB in Phoenix (though also consistent with an AGN). Its optical counterpart is too faint and red for an early type star (m_V=21.6, $B-V$=0.51). Source #61 is again probably an AGN.

4.5.5 Source #68

Source #68 is an unfortunately placed X-ray source, falling on a bad column on the EPIC-pn detector and near a chip border in both MOS detectors. The total number of counts for this source was not sufficient to extract a spectrum and so few conclusions can be drawn. The optical counterpart has brightness, but not colours, consistent with an HMXB in Phoenix (m_V=21.2, $B-V$=0.28) and the 0.2–12.0 keV flux value derived from the source detection (6.3×10^{-14} erg cm^{-2} s^{-1}) suggests a luminosity of 1×10^{36} erg s^{-1} (assuming #68 is associated with Phoenix). However this flux value should be interpreted with care as detector edge effects may introduce an additional uncertainty that cannot be accounted for. Source #68 is also probably an AGN.

4.6 Other sources associated with Phoenix

Interestingly, only one source in our field, #48, is coincident with the most obvious optical emission of the Phoenix dwarf galaxy. Massive black holes have been discovered in nearby dwarf galaxies (for example see van Wassenhove *et al.* 2010) and the location of the source, close to what appears to be the centre of the galaxy, led me to consider the source as a possible massive black hole candidate. Although radial velocities have been measured for a handful of stars in Phoenix (Gallart *et al.*, 2001; Irwin and Tolstoy, 2002) no information on the location of the dynamical centre is available.

An estimate of the position of the galaxy centre has been obtained by maximising the number of LGGS sources within a circular region when the centre and size of the region is varied, following the method of Dieball *et al.* (2010). The uncertainties are estimated via a bootstrapping method. One thousand artificial catalogues were created by sampling with replacement from the original LGGS catalogue. The centre was then estimated for each of these artificial catalogues using the same method detailed above. The error on our position is taken to be the standard deviation of these centre estimates. The final result was obtained using a circular region with a 150 pixel (40.5 arcsec) radius, but experiments with other region sizes

produced consistent results. The galaxy centre was put at RA=$01^h51^m8.2^s \pm 6.1$", Dec=-44°26'55.9"$\pm$7.6". This position should be treated with caution as the LGGS catalogue is by no means complete.

Source #48 is situated 40 arcsec away from the centre position with a position error of 1.7 arcsec. This mis-match in positions suggests that source #48 is unlikely to be a massive black hole located at the centre of the Phoenix galaxy. The source hardness ratios are also not consistent with a black hole/AGN in Phoenix. However, the errors on all these values are large and better X-ray and optical data are needed before drawing any firm conclusions about this source.

4.7 Discussion

Of the 81 X-ray sources detected in the *XMM-Newton* field of view, six have been categorised as foreground stars, four as background galaxies and one as a possible AGN. The majority of the remaining sources in the field of view with optical counterparts have $\log(\frac{f_X}{f_{opt}})$ values between -1 and 1, typical of local AGNs and high star forming galaxies (Hornschemeier *et al.*, 2001). Source #96 has the greatest $\log(\frac{f_X}{f_{opt}})$ value at 1.13, putting it at the very X-ray brightest end of these objects and a possible BL Lac candidate. Further analysis of 5 potential HMXB candidates in the field of view suggests they are all AGN.

There is no evidence for any black hole binaries in Phoenix. The mass of Phoenix is too low for us to expect any LMXBs, so any black hole binaries present would be expected to be high mass black hole X-ray binaries, in the low/hard state. The expected ratio of BeXRBs with neutron stars to black holes in the Galaxy is relatively high (see Section 1.4.1). Thus far, not a single BeXRB has been found to host a black hole. This leaves only black hole supergiant systems. These systems are a small fraction of the total HMXB population in our own Galaxy and are not found at all in the SMC (e.g. Coe *et al.* 2009). If the population of HMXBs is as small as predicted, the presence of a black hole supergiant HMXB in Phoenix seems unlikely.

If these sources are spectroscopically confirmed to be AGN, their position behind the gas cloud and their magnitude will make them an excellent tool to further probe the metallicity of this region using the NaID and CaIIK lines (for e.g. see van Loon *et al.* 2009). Accurate measurements of the Na and Ca column density across these sources could tell us more about the gas cloud and may even reveal inhomogeneities in the chemical composition across the region.

BeXRBs in the SMC are found in regions where a burst of star formation occurred ∼25-60 Myr ago. As such the five X-ray sources identified offset to the west main stellar body, where a strong episode of star formation took place around ∼40 Myr ago, were good BeXRB candidates. However, none of these sources display all the X-ray and optical characteristics of a BeXRB. The strongest evidence for a neutron star is periodic modulation of the X-ray flux. We do not have the required sensitivity to detect this in the data but this condition is sufficient, not necessary, for proof of a neutron star's existence.

In general, BeXRBs are by far the most numerous subclass of HMXBs (Section 1.4.1) and so have the greatest likelihood of existence in Phoenix. However, as sgXRBs hosting neutron stars are persistent sources of X-rays, we may have a better chance of seeing them in a single epoch. The lack of evidence for any supergiant binaries, with either a black hole or a neutron star secondary, would strongly suggest that they do not exist in Phoenix. This is in line with current predictions based on star formation rate (Section 1.5.2) and is further evidence in support of this relation. The transient nature of BeXRBs means there is a possibility that a greater population exists than is hinted at here. From our regular observations of the SMC over a 10 yr interval, we find that BeXRBs are in outburst for around ∼10% of an orbital period and are active, on average, for ∼20% of the time (Galache *et al.*, 2008; McGowan *et al.*, 2008). It follows that the probability of seeing a particular BeXRB active at any one moment is about ∼2%. Should the number of BeXRBs in Phoenix be limited to just 1–2 systems, then the probability of seeing just one system active at any moment in time is <10%. Further observations of the Phoenix dwarf galaxy could yet reveal a HMXB population.

Since every piece of matter in the Universe is in some way affected by every other piece of matter in the Universe, it is in theory possible to extrapolate the whole of creation every sun, every planet, their orbits, their composition and their economic and social history from, say, one small piece of fairy cake.

THE HITCHHIKER'S GUIDE TO THE GALAXY (1979)

5

The SMC BeXRBs as probes of Neutron Star Formation Channels

In this Chapter I will discuss another project, started as part of my PhD, as a follow up paper to Knigge *et al.* (2011). The authors of this paper demonstrated that the SMC BeXRBs can be split into two sub populations based on their pulse periods. This bi-modality is even more significant when we consider the SMC, LMC and MW BeXRB systems together. They interpret these two populations as evidence for the two main formation channels of neutron star, iron core collapse supernovae and electron capture supernovae which, until now, have been thought to produce almost indistinguishable compact objects. Here we report on our attempts to find further evidence for the two channels of neutron star formation. Much of the work has been done in consultation with Prof. Christian Knigge.

5.1 Introduction

When studying HMXBs in detail, one has to look to the galactic population or those of our closest neighbours, the LMC and SMC. The HMXBs in the SMC are ideal for population studies: they do not suffer from the large distance uncertainties that

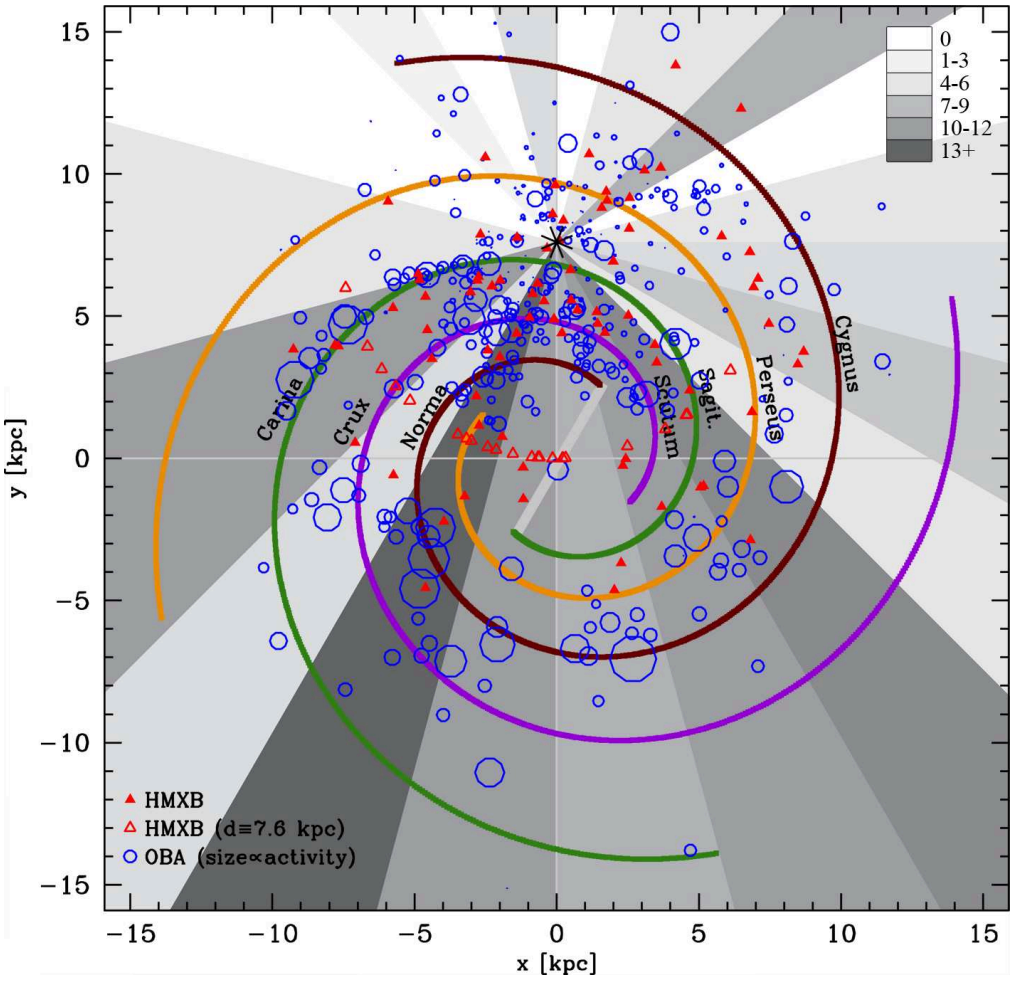

Figure 5.1: Galactic distribution of HMXBs with known distances (filled triangles) and the locations of OB associations. HMXBs whose distances are not known have been placed at 7.6 kpc (empty triangles). The shaded histogram represents the number of HMXBs in each 15° bin of galactic longitude as viewed from the Sun. Taken from Bodaghee *et al.* (2012)

plague the galactic population, are all believed to be formed in one star formation episode, and so are all roughly the same age, and exist in very similar environments within the SMC. With the exception of SMC X-1, all the HMXBs in the SMC are BeXRBs. The low mass of the SMC means that the predicted number of LMXBs is small (0-1). As mentioned in Section 1.4.1, the ratio of Be/black hole binaries to Be/neutron star binaries is such that we would expect ≤ 1 system in the SMC. As such the sample of neutron stars has very little risk of contamination, this is discussed further in Section 5.1.1. The small angular size of the SMC ($\sim 2 \times 2$ degree) means that this large, homogeneous population of BeXRBs can be observed with relative ease.

It has long been thought that most neutron stars in the universe are formed by

two particular types of core-collapse supernovae, iron-core collapse supernovae or electron-capture supernovae. In the first case, a high-mass star's iron core exceeds the Chandrasekhar limit. In the second case, a lower mass oxygen-neon-magnesium core collapses due to a loss of pressure support caused by a sudden capture of electrons by the neon and/or magnesium nuclei in the core. However, the neutron stars produced by these two different channels are practically indistinguishable. The neutron stars produced by electron capture supernovae should be slightly less massive ($<$1.3 $M_\odot$ compared with $\sim$1.4 $M_\odot$ for iron core collapse supernovae, Nomoto 1984) and will receive a smaller supernova kick velocity ($v_{kick} \simeq 50$ km s^{-1} versus $v_{kick} \simeq 200$ km s^{-1}). The aim of this project was to investigate if there was any further evidence for these two different formation channels in the physical parameters in any of the SMC BeXRBs.

5.1.1 The Data Set

Table 5.1 gives the positions of the the SMC X-ray Pulsars (SXPs) used in this work. Only pulsars with secure pulse periods were selected to avoid any contamination with potential Be/White Dwarf systems and to guarantee that all sources are indeed neutron stars. These are the same sources used by Knigge *et al.* (2011), compiled by Prof. Malcolm Coe. The sources are either spectroscopically or photometrically confirmed, i.e. have an emission line star in their X-ray error circle with colours consistent with those of an early type star. This includes the sample used by Coe *et al.* (2005) with the exception of SXP0.92 and SXP8.02 which are now thought to be spurious.

5.2 BeXRB-Cluster separation

Early type main sequence stars are not uniformly distributed on the sky, instead they are loosely concentrated in groups, known as "associations" (Blaauw, 1964). The clustering between HMXBs and OB associations has been well established (e.g. Bodaghee *et al.* 2012, see Figure 5.1). Coe *et al.* (2005) assume that the closest stellar cluster to a BeXRB in the SMC is the natal cluster (i.e. the birthplace of the BeXRB) and use the BeXRB-cluster separations to constrain the kick velocity. If this assumption is correct and the distribution of kick velocities is indeed bimodal, then this should be reflected in the separation of the BeXRBs from the closest cluster. The positions of the BeXRBs in Table 5.1 were compared with those of the

Table 5.1: Summary of SXPs used in this work and Knigge *et al.* (2011)

SXP ID	RA	Dec	P_{spin} s	P_{orb} days	Spectroscopically confirmed?
SXP2.37	00:54:34	-73:41:03	2.37	18.62	YES
SXP2.76	00:59:12.8	-71:38:44	2.76	82.1	
SXP3.34	01:05:02	-72:11:00	3.34	10.72	YES
SXP4.78	00:52:19	-72:19:48	4.78		
SXP6.62	00:54:46	-72:25:23	6.62		
SXP6.85	01:01:24	-72:43:30	6.85	22	YES
SXP6.88	00:54:46.2	-72:25:23	6.88	2.71	
SXP7.78	00:52:07.7	-72:25:43.70	7.78	44.8	YES
SXP7.92	01:01:56	-72:32:36	7.92	36	
SXP8.80	00:51:52	-72:31:52	8.9	33.4	YES
SXP9.13	00:49:13.6	-73:11:39	9.13	40.1	YES
SXP11.5	01:04:41.4	-72:54:04.60	11.48	36.3	YES
SXP11.9	00:48:13.9	-73:22:03.50	11.89		
SXP15.3	00:52:15.3	-73:19:14	15.3	75.1	YES
SXP18.3	00:49:11.4	-72:49:39	18.37	17.2	
SXP22.1	01:17:40.5	-73:30:52	22.07		YES
SXP25.5	00:48:14.1	-73:10:04	25.55		YES
SXP31.0	01:11:09	-73:16:46	31	90.4	YES
SXP46.6	00:53:53.8	-72:26:35	46.6	137.4	YES
SXP59.0	00:54:57.4	-72:26:40.30	58.95	122	YES
SXP65.8	01:07:12.6	-72:35:33.80	65.8	111	YES
SXP74.7	00:49:04.6	-72:50:53	74.8	33.3	YES
SXP82.4	00:52:09	-72:38:03	82.4	362	YES
SXP85.4	00:57:12	-72:18:00	85.4		
SXP91.1	00:50:55	-72:13:38	91.1	88	YES
SXP138	00:53:23.8	-72:27:15	138	125	YES
SXP140	00:56:05.2	-72:22:00	140.1	197	YES
SXP152	00:57:50.3	-72:07:56	152.1		YES
SXP169	00:52:54	-71:58:08	169.3	68.6	YES
SXP172	00:51:50	-73:10:40	172.4	70.4	YES
SXP202A	00:59:20.8	-72:23:17	202		YES
SXP202B	00:59:29	-72:37:03	202	229.9	
SXP214	00:50:11	-73:00:26	214		YES
SXP264	00:47:23.7	-73:12:27	263.6	49.2	YES

SXP ID	RA	Dec	P_{spin} s	P_{orb} days	Spectroscopically confirmed?
SXP280	00:57:48	-72:02:40	280.4	127.3	YES
SXP293	00:58:12.64	-72:30:48	293	59.7	YES
SXP304	01:01:01.70	-72:07:02	304.5	520	YES
SXP323	00:50:44.8	-73:16:06	323.2		YES
SXP327	00:52:52.5	-72:17:14.90	327	45.99	YES
SXP342	00:54:03.8	-72:26:32	342		
SXP348	01:03:13	-72:09:18	349.9	93.9	YES
SXP455	01:01:20.5	-72:11:18	452	75	YES
SXP504	00:54:55.6	-72:45:10	503	269	YES
SXP565	00:57:36.2	-72:19:34	564.8	95	
SXP645	00:55:35.2	-72:29:06	645		
SXP701	00:55:17.9	-72:38:53	702	412	YES
SXP726	01:05:55.3	-72:03:50.20	726		
SXP756	00:49:42.1	-73:23:14.10	755.5	394	YES
SXP892	00:49:29.7	-73:10:58	892.8		YES
SXP967	01:02:06.7	-71:41:15.80	967		YES
SXP1323	01:03:37.5	-72:01:33	1323		YES

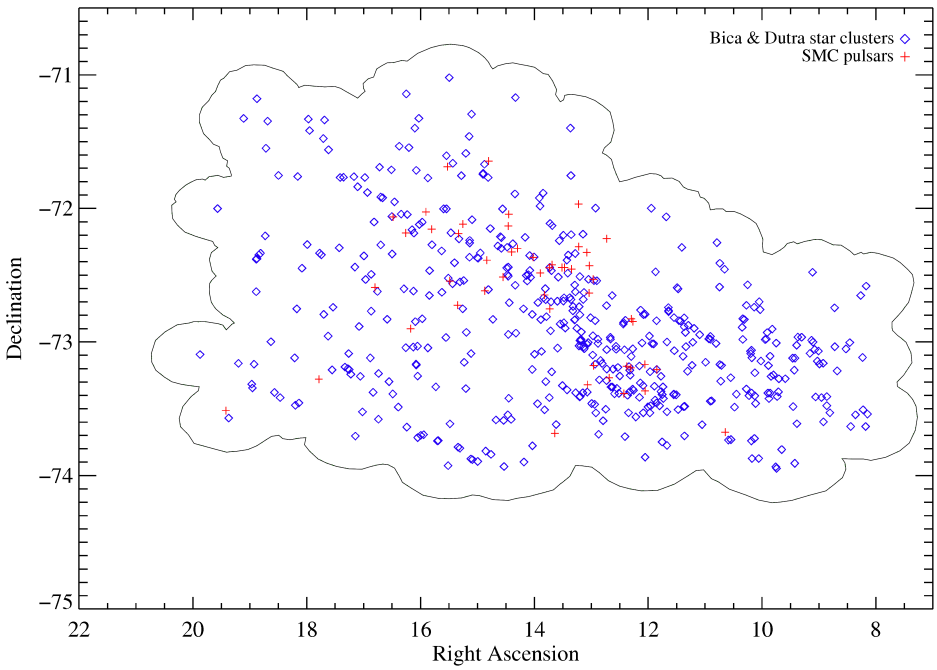

Figure 5.2: Position of the SXPs and star clusters from Bica and Dutra (2000). The envelope indicates the area defined for the random points.

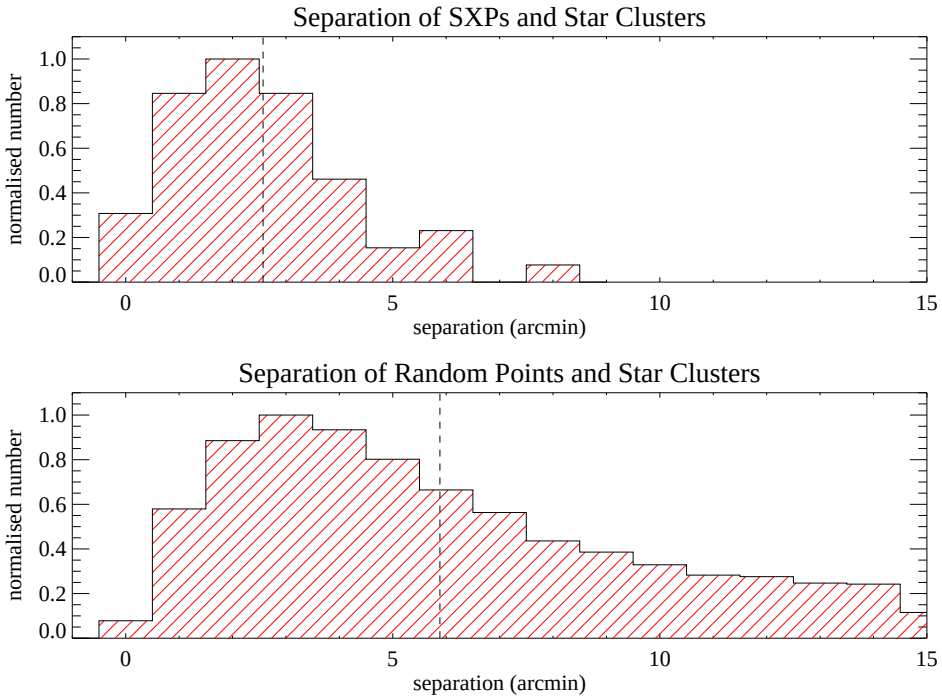

Figure 5.3: From top to bottom, histograms of the BeXRB-closest cluster separation and the random points-cluster separation respectively. The broken lines marks the mean of each distribution

$\sim$600 star clusters in the SMC from Bica and Dutra (2000) and the projected distance to the nearest cluster calculated.

Approximately 500,000 random points were generated within the SMC by defining an area centred on, but larger than, the SMC ($\sim$70 deg^2) and then restricting the maximum distance a point could be from a star cluster to$<$15 arcmin. This not only allows the whole of the SMC to be evenly sampled but also greatly reduces the chance of any artificial result due to the coverage of the catalogue (i.e. because a significant fraction on the random points are generated outside the coverage of the survey). Figure 5.2 shows the positions of the star cluster and SXPs along with the region that the random points occupy (enclosed by the solid black line).

Figure 5.3 shows the distribution of the separations for both the real and simulated sources. The average separation between a BeXRB and a star cluster is 2.6' compared with 5.9' for the random points. A KS test performed on the separations of the two samples calculated that the probability that both sets of sources are drawn from the same distribution is 2.4×10^{-9}%. This is just less than a 6σ significance.

However this test may over emphasise the significance of the clustering, as the random positions may not fairly reflect the spatial distribution of the BeXRBs in the SMC. To confirm the result, we shifted the BeXRBs by an amount D_{crit} in the

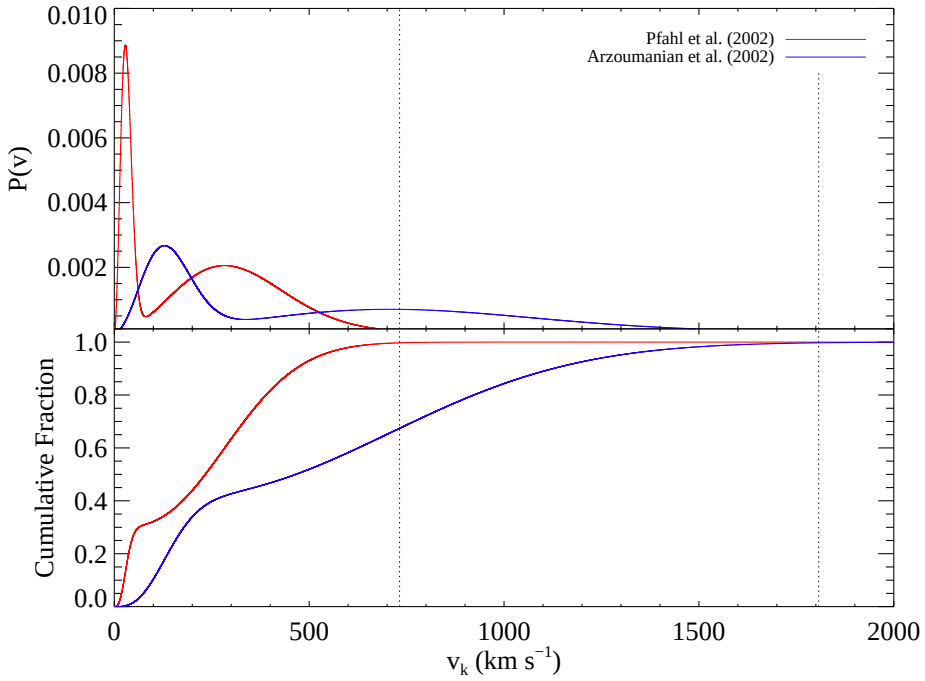

Figure 5.4: Two theoretical distributions of neutron star kick velocities from Pfahl *et al.* (2002) and Arzoumanian *et al.* (2002). Top panel shows the probability distribution function (PDF), bottom panel shows the cumulative distribution function (CDF). Broken lines shows the velocities at which the CDFs equal 0.9973.

negative right ascension (RA), positive right ascension, negative declination (dec) and positive dec in turn, calculated the distance to the closest clusters and compared these results to those of the real data set. The choice of D_{crit} is non trivial: the shift needs to be big enough to destroy any real associations but small enough to keep the SXPs in their local environment. A shift of 2 degrees would certainly satisfy the first criteria, but would shift most of the SXPs out of the SMC. Similarly, a shift of 2 arcmins would keep the SXPs in their local environment, but is unlikely to destroy all the real associations.

To define D_{crit} I estimated the maximum distance a BeXRB in the SMC could travel from its natal cluster. To do this I used the bimodal kick velocity distributions of Pfahl *et al.* (2002) and Arzoumanian *et al.* (2002), shown in Figure 5.4 and the spectral distribution of BeXRBs in the SMC from McBride *et al.* (2008). I took the value of v_{kick} to be that which is greater than 99.73% of the cumulative distribution function (CDF). This would suggest that only 3 in 1000 BeXRBs should experience a kick greater than this value, since the sample contains only 51 sources, I am confident that no BeXRB in the SMC should have experienced a kick greater than this. This gave v_{kick} values of 732 km s^{-1} and 1807 km s^{-1} for the Pfahl *et al.*

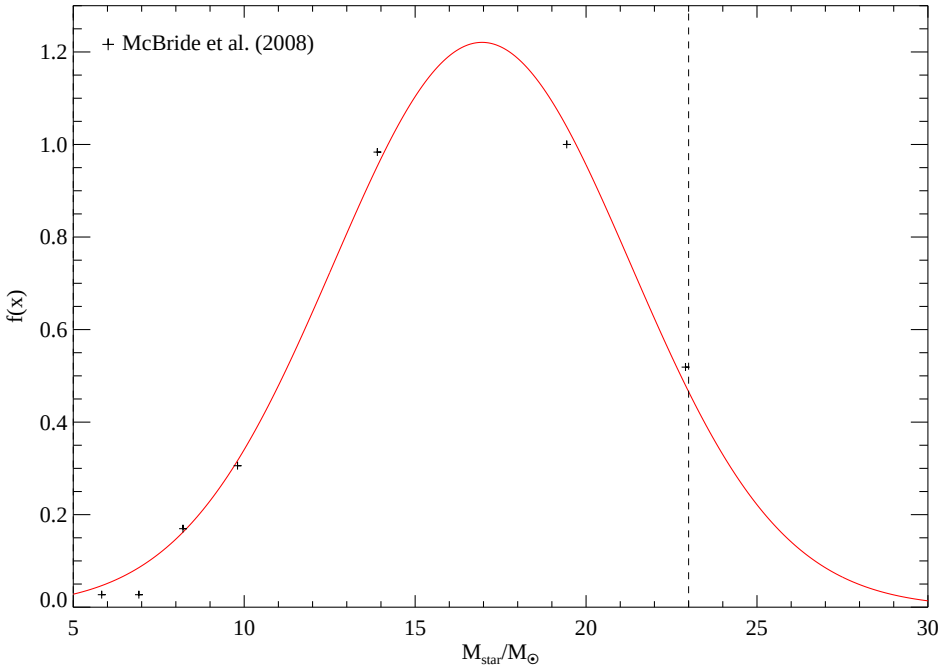

Figure 5.5: Mass distribution of the optical counterpart to the SXPs. Points show the data from McBride *et al.* (2008). The solid line shows the Gaussian distribution fit to the data. The broken line marks the maximum mass of an optical counterpart in the simulation (see Section 5.2.1).

(2002) and Arzoumanian *et al.* (2002) distributions respectively.

Using the $\log\frac{L}{L_\odot}$ values of main sequence stars from de Jager and Nieuwenhuijzen (1987), the relationship

$$\frac{L}{L_\odot} = \left(\frac{M}{M_\odot}\right)^{3.5} \tag{5.1}$$

and the spectral distribution of SXPs reported by McBride *et al.* (2008), I produced a mass distribution for the spectral counterparts, shown in Figure 5.5 . This was fit with a Gaussian using the IDL routine gaussfit.pro[1] with a mean value 16.96 $M_\odot$ and standard deviation 4.35 $M_\odot$. Adopting an average counterpart mass of 17 $M_\odot$, a neutron star mass 1.4 $M_\odot$ and conserving momentum gives system velocities, v_{sys} of 55.7 km s^{-1} and 137.5 km s^{-1} for the two distributions respectively.

The most massive optical counterparts of the SXPs have spectral type O9.5V and so a mass $\sim 23\ M_\odot$. The nuclear timescale of a star, defined as the time it would

[1] http://www.solar.ifa.hawaii.edu/Tropical/Bin/tropical_idl/usr/local/lib/idl/lib/gaussfit.pro

take the star to exhaust its nuclear fuel reserve based on its current consumption, is

$$\tau_{nuc} \propto \frac{M}{L}$$

$$= 10^{10} \left(\frac{M}{M_{\odot}} \right)^{-2.5} \text{ yr} \tag{5.2}$$

substituting Equation 5.1 for L. This gives a stellar lifetime of $\tau_{nuc} \sim 4$ Myr for an O9.5V star. If we assume that all the BeXRBs in the SMC were formed at the same time, $\tau \simeq 4$ Myr ago, then $D_{crit} = \tau v_{sys}$. This gives *maximum* shift values of 13 arcmin and 32 arcmin for the Pfahl *et al.* (2002) and Arzoumanian *et al.* (2002) kick velocity distributions respectively (assuming the distance to the SMC is 61 kpc, Hilditch *et al.* 2005).

The separations of the new, shifted sources to the closest cluster were calculated and compared with those of the unshifted (i.e. real) sources. The significance of the shifts were, again, calculated with the KS test. The results were highly dependent on both the direction and the value of D_{crit} used. For example, the KS test gave a probability that the separations of the sources shifted by 13 arcmin in the positive RA direction were drawn from the same distribution as the real sources of 85%. The sources shifted by the same amount in the negative dec direction only had a 0.001% probability of being drawn from the same distribution. When D_{crit} was increased to 32 arcmin, the probabilities for these shifts became 0.05% and 16% respectively. This implies that the spatial distribution of the stellar clusters in the SMC is highly structured.

Figure 5.6 shows the distribution of the cluster-cluster separations. Whilst the average cluster-cluster separation is similar to that of the average SXP-cluster separation (3.3 arcmin compared to 2.6 arcmin), the distribution peaks at a smaller separation. This, along with the results discussed above, suggests that the average value of the separation distribution does not reflect the characteristic distance scale. When the shape of the separation distributions are also considered, it becomes apparent that the spatial structure of the clusters has a shorter characteristic distance than that of the BeXRB-cluster separations and that the assumption that the closest cluster to a BeXRB is its natal cluster is almost certainly incorrect. This in turn implies that a bimodal v_{kick} distribution may not leave any signature on the BeXRB-cluster separation distribution.

This indeed seems to be the case: Figure 5.7 shows the plot of BeXRB cluster separation against P_{spin}. Figure 1.20 suggests that the break between the long and

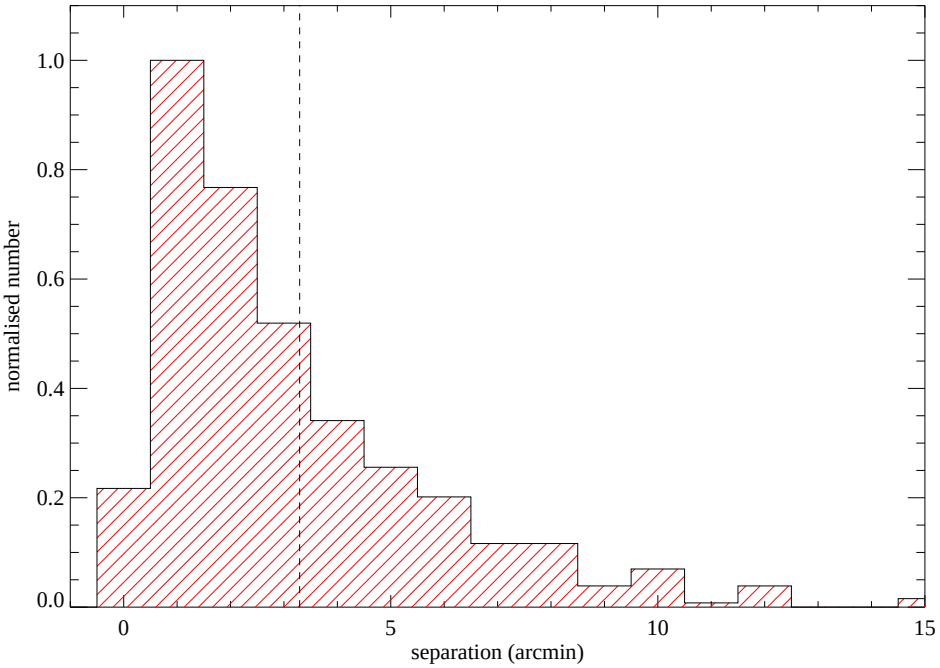

Figure 5.6: Histograms of the cluster-cluster separation. The broken line marks the mean of the distribution.

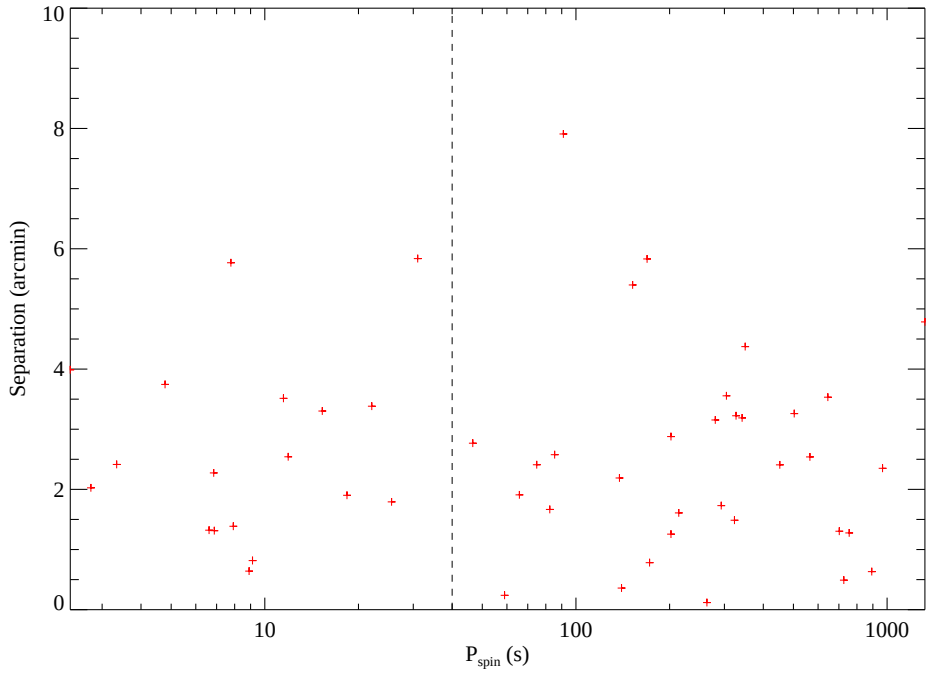

Figure 5.7: Plot of BeXRB cluster separation against P_{spin}, the break between the long and short period BeXRBs $P_{spin} = 40$ s is marked by the broken line

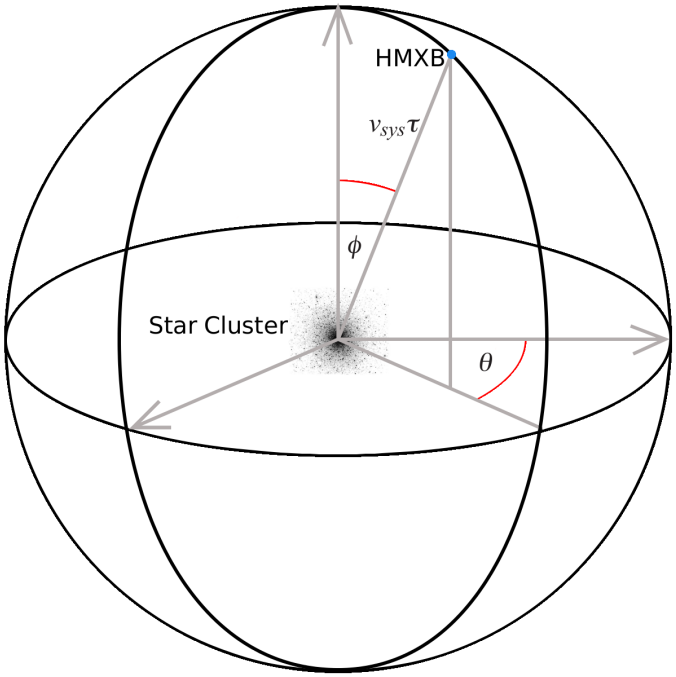

Figure 5.8: Schematic of the simulation. After a time τ, the simulated HMXB has spherical co-ordinates $(v_{sys}\tau,\theta,\phi)$ with respect to the natal cluster.

short spin period systems occurs at ∼40 s. A KS test yields a probability that the separations of these two sub groups are drawn from the same distribution of 82%.

5.2.1 Simulation

Whilst I have shown that it is not possible to obtain any information about the underlying v_{kick} velocity from the separations of the BeXRBs from the clusters, it may yet be possible to recreate the distribution of the SMC BeXRBs from a given v_{kick} distribution. I have written a simulation that attempts to do this. Uniformly distributed random numbers are generated to determine:

- a cluster from the Bica and Dutra (2000) catalogue
- a mass from the the distribution shown in Fig. 5.5
- a kick velocity from the Pfahl *et al.* (2002) distribution shown in Fig. 5.4
- two angles, θ and ϕ (see Fig. 5.8)

We again assume that all the sources were created in one event $\tau = 4$ Myr ago. The lifetime of the counterpart selected is calculated using Equation 5.2, if it is less

than τ (i.e. earlier than spectral type O9V) it is removed from the sample. The mass at which this occurs is shown as a broken line in Figure 5.5. The distribution is truncated at 5 $M_{\odot}$ (spectral type B3) to keep the simulated BeXRBs consistent with the observed spectral distribution seen. Momentum is then conserved to find the corresponding v_{sys} for a given v_{kick} and assuming a neutron star mass of 1.4 $M_{\odot}$.

The position of a simulated source after a time τ is then given by the spherical co-ordinates, centered on the random cluster selected as its natal cluster with radius $v_{sys}\tau$ (see Fig. 5.8. To ensure even coverage this sphere, the angles θ and ϕ cannot be drawn from uniform distributions themselves as this leads to bunching around the poles. Instead the variates u and v (which can take any value between 0 and 1) are used to calculate θ and ϕ.

$$\theta = 2\pi u$$

$$\phi = \cos^{-1}(2v - 1)$$

The 3 dimensional position of the simulated source is then converted into sky co-ordinates RA and dec. The distance to the closest cluster is calculated for the simulated sources and then compared with the the cluster-BeXRB separation distribution.

5.2.1.1 Work to be Done and Preliminary Results

Currently the simulation does not take into account any effects binarity may have on these systems: it assumes that all the BeXRBs were formed at exactly the same time (4 Myr ago) and that the counterparts evolve completely separately from the neutron star. Whilst these assumptions may be acceptable, this should be confirmed. In particular, the value of 4 Myr for the age of BeXRBs should be reexamined and better justified. The simulation also assumes that the binary survives the supernova that creates the neutron star, regardless of the kick velocity imparted. Whilst Portegies Zwart (1995) have shown that the value of the kick velocity experienced by the systems has very little effect on the spectral distribution of BeXRB counterparts (see Section 1.5.3), it may be that, when these effects are fully accounted for, the distribution of available kick velocities is truncated. The simulation does not take the current X-ray coverage of the SMC into account. Some of the simulated sources are located on the very edge of the SMC. This leads to outliers in the simulated source-cluster separation distribution, which may lead to a significant difference when compared with the real BeXRB-cluster separations. However, if these areas

have not been observed with any of the X-ray telescopes then these sources should not be included in the final simulated source-cluster separations, as any BeXRB population in these regions are also not included in the real sample. Until recently,

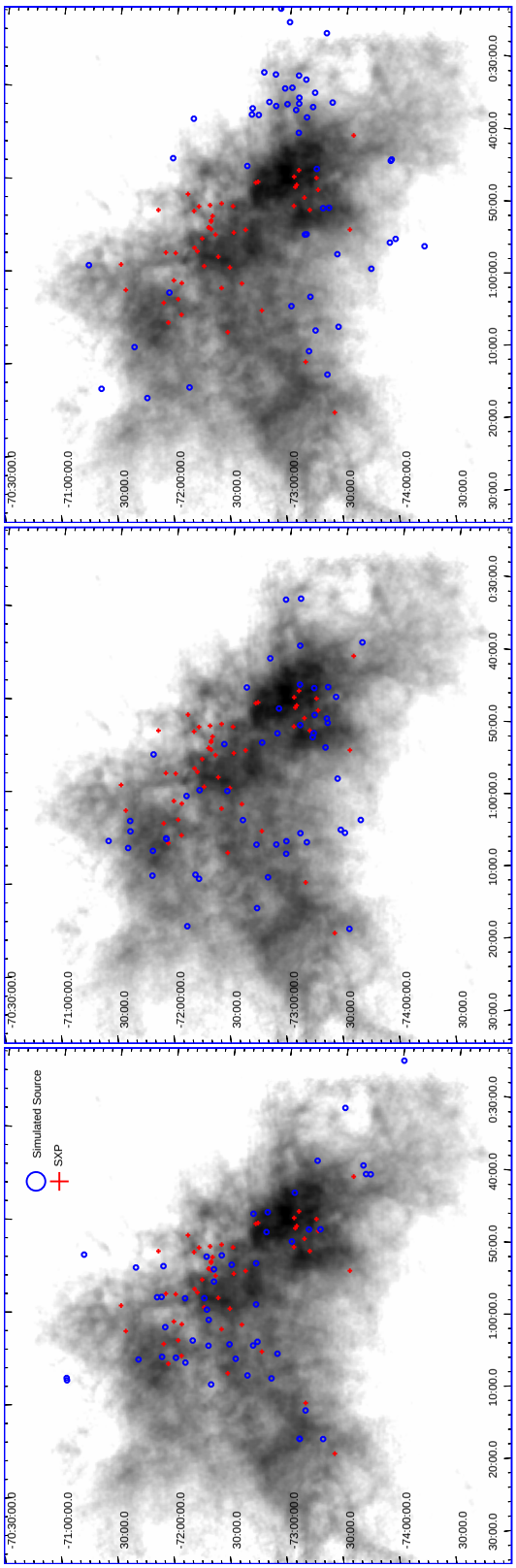

Figure 5.9: Results of the simulation described in Section 5.2.1. The crosses mark the positions of the real SXPs, the circles show the positions of sources generated by the simulation. From left to right, panels show sources generated when only the youngest, mid-aged and oldest clusters in the Glatt *et al.* (2010) catalogue are considered as potential natal clusters.

much of the X-ray coverage of the SMC has focused on the Bar (Galache *et al.*, 2008), with occasional deeper looks at the Wing (e.g. McGowan *et al.* 2008). The *XMM* catalogue (Haberl *et al.*, 2012a) has observed the entire SMC down to a limiting magnitude of a few 10^{33} erg s^{-1}: the quiescent level of BeXRBs. This should lead to a complete catalogue of SMC BeXRBs with even coverage, allowing an envelope to be defined outside which any simulated sources should be discounted.

No information is available in the Bica and Dutra (2000) catalogue about the age of the stellar clusters. This information is included in the more recent, but smaller Glatt *et al.* (2010) catalogue, which is approximately half the size of Bica and Dutra (2000). Nevertheless very preliminary results, shown in Figure 5.2.1.1 do suggest that when the clusters are divided into three age ranges, $\leq 10^7$ yr, $10^7 - 10^8$ yr and $\geq 10^9$ yr and each subgroup of clusters are considered as potential natal clusters in turn, it is the youngest clusters which produce the result most consistent with observations. The KS test gives probabilities that the separations of the simulated and real sources from the clusters are drawn from the same distribution of 44%, 3.0% and 0.19% for the youngest, mid-aged and oldest clusters respectively. More generally, the simulation has only been run using the kick velocity distribution of Pfahl *et al.* (2002). Several other hypothesised distributions exist (e.g. Arzoumanian *et al.* 2002) which should also be trialled, potentially leading to some to being ruled out.

5.3 BeXRB Neutron Star Mass Distribution

As mentioned in Section 5.1, the different supernovae are expected to produce different mass neutron stars. Constraining the neutron star mass is notoriously difficult. To date only a handful of the neutron stars in HMXBs have had their mass reliably constrain, all of which have been in eclipsing systems (e.g. OAO 1657-415, Mason *et al.* 2012 for a recent example). However the $log_{10}(-\dot{P}) - log_{10}(P_{spin}L^{\frac{3}{7}})$ diagram of Ghosh and Lamb (1979), introduced in Section 1.5.6, does allow for the mass of the neutron star to be inferred from observational measurements, under certain assumptions. Figure 5.3 shows a $log_{10}(-\dot{P}) - log_{10}(P_{spin}L^{\frac{3}{7}})$ diagram with the subset of the sources in Section 5.1.1, for which $-\dot{P}$ is known (see Table 5.2). These are sources that have had outbursts long enough to determine $-\dot{P}$, $P_{spin}$and L_{37}. The theoretical curves over plotted show the relationship between the two parameters for different neutron star masses, assuming a magnetic moment of $\mu_{30} = 0.48$ (the best fit value from Ghosh and Lamb 1979).

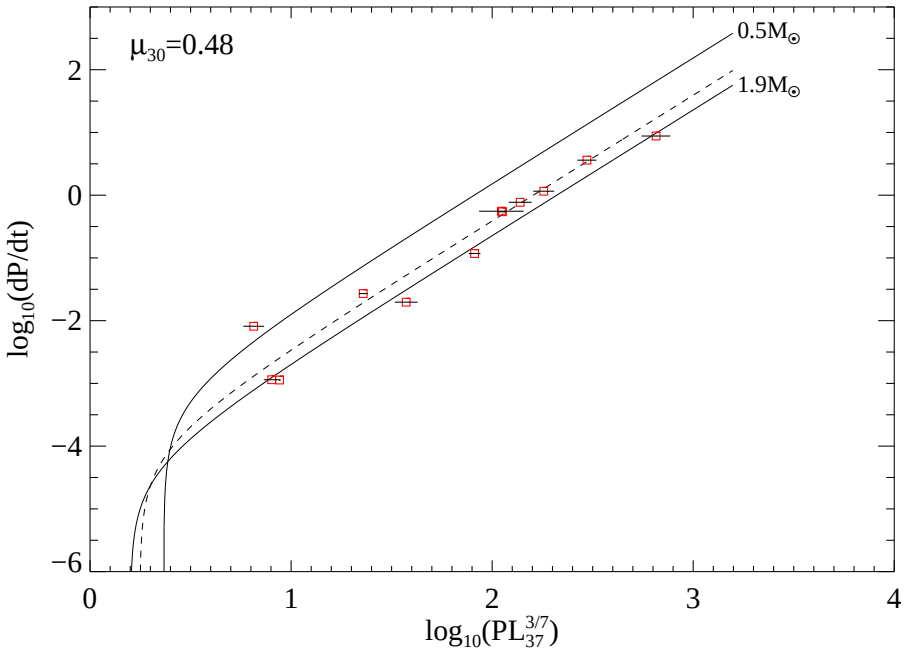

Figure 5.10: $log_{10}(-\dot{P}) - log_{10}(P_{spin}L^{\frac{3}{7}})$ diagram for the SMC BeXRBs.

Approximately 100 of these theoretical curves were generated in the neutron star mass range $0.1 - 3.5\ M_{\odot}$, assuming $\mu_{30} = 0.48$. The masses corresponding to the contours which intersected the data points (within errors) are shown in Figure 5.3. There is no clear evidence for a bimodal mass distribution, however as with the BeXRB-cluster separations, this does not mean that the true mass distribution is not bimodal. The errors on the $PL^{\frac{3}{7}}$ values, which are driven by the errors on the luminosities, are large enough to disguise any bimodality and this method requires the BeXRBs to have the same magnetic moments - an assumption which may not be valid.

5.4 Conclusion

Thus far, no evidence has been found to support the hypothesis of two different channels of neutron star formation using the SMC BeXRBs (beyond that given in Knigge *et al.* 2011). The spatial distribution of the stellar clusters in the SMC makes it impossible to determine the underlying kick velocity distribution of the neutron stars from the BeXRB-cluster separation alone. Simple simulations are not yet able to reproduce the distribution of the SMC BeXRBs, however I have identified several areas where these simulations can be improved. More detailed cluster catalogues are

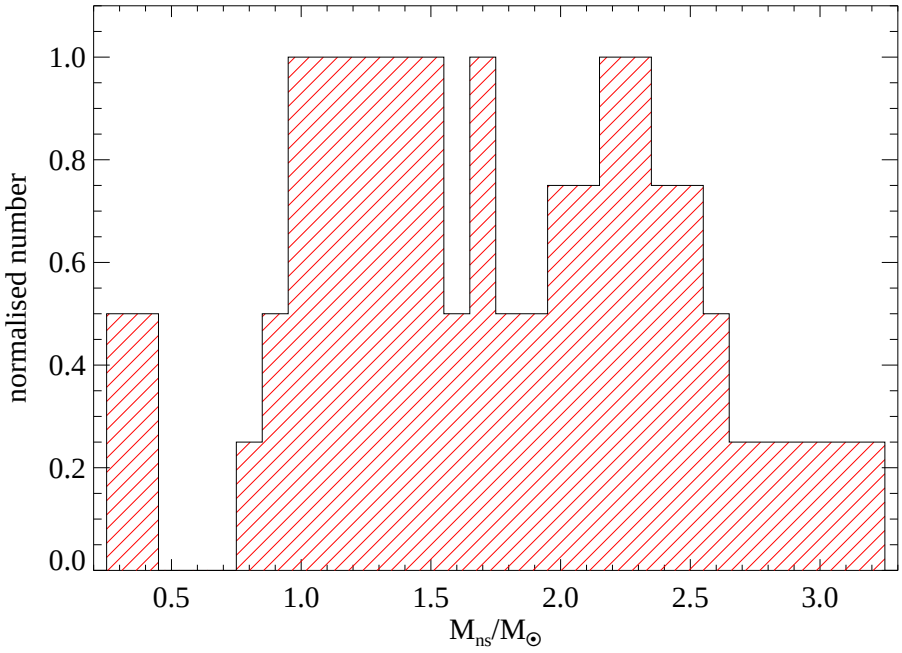

Figure 5.11: Histogram of the neutron star mass values consistent with the $-\dot{P} - P_{spin}L^{\frac{3}{7}}$ values of the SMC BeXRBs, assuming $\mu_{30} = 0.48$.

Table 5.2: Subset of SXPs in Table 5.1 for which $-\dot{P}$ is known. All measurements are simultaneous.

SXP ID	P_{spin} s	$\dot{P}$ s s^{-1}	L_{37} $\times 10^{37}$ erg cm^{-2} s^{-1}
SXP2.37	2.372±0.001	$-3.10 \pm 0.02 \times 10^{-6}$	21.1±0.24
SXP6.85	6.851±0.002	$-3.13 \pm 22.5 \times 10^{-6}$	1.44±0.20
SXP7.78	7.785±0.002	$-2.23 \pm 0.10 \times 10^{-5}$	0.66±0.12
SXP18.3	18.38±0.01	$-7.40 \pm 0.09 \times 10^{-5}$	1.66±0.13
SXP46.6	46.5±0.05	$-5.40 \pm 5.67 \times 10^{-5}$	0.60±0.12
SXP59.0	58.8±0.02	$-3.22 \pm 0.09 \times 10^{-4}$	2.16±0.22
SXP91.1	90.1±0.05	$-1.49 \pm 0.04 \times 10^{-3}$	1.68±0.11
SXP169	167±0.5	$-3.17 \pm 0.32 \times 10^{-3}$	1.20±0.22
SXP172	172.2±0.2	$-1.52 \pm 0.09 \times 10^{-3}$	0.36±0.14
SXP172	171.6±0.2	$-2.11 \pm 0.26 \times 10^{-3}$	0.60±0.12
SXP323	319±0.5	$-9.90 \pm 0.34 \times 10^{-3}$	0.84±0.14
SXP892	895±5.0	$-2.40 \pm 1.23 \times 10^{-2}$	0.48±0.12

required which include the approximate ages of the stellar clusters to fully explore any cluster age dependence hinted at here. A complete SMC BeXRB catalogue is also needed for the results of the simulation to be convincing.

The current observational parameters of the BeXRBs are not of sufficient quality to determine the underlying mass distribution of the BeXRB neutron stars. All of the data in Table 5.2 has come from the *RXTE* monitoring of SMC. The lack of imaging introduces a large error in the luminosity values of the outbursts as it is not possible to identify the background level. Observations of Type II outbursts with the next generation of X-ray telescopes, e.g. *XMM-Newton* or *Chandra* would have smaller errors on the flux values which may improve the mass determination following the method outlined in Section 5.3. A better understanding of the magnetic fields of BeXRBs is required to validate or refute the assumption that the magnetic moments of the BeXRBs are approximately the same, currently the data are completely consistent with neutron stars of equal mass with varying magnetic moments (see Figure 1.21). Maggi *et al.* (2013) have discovered the first eclipsing BeXRB in the LMC. Should a population of eclipsing BeXRBs exist, they would be an invaluable tool. Mass determinations of their neutron stars would break the neutron star mass-magnetic moment degeneracy and could be used to determine an acceptable average value for the magnetic moment (if indeed such a value exists). This in turn may allow for the mass distribution of the SMC BeXRBs to be determined using the method detailed in this Chapter.

"Life! Don't talk to me about life."

THE HITCHHIKER'S GUIDE TO THE GALAXY (1979)

6

Conclusions & Future Work

Throughout my PhD I have studied HMXBs both individually and as a population. In this Chapter, I will summarise my work and identify areas where my results may be used as stepping stones for new projects.

In Chapter 2 I explain the decrease in the pulsed fraction of Swift J045106.8-694803 with increasing energy and the anticorrelation of the hardness ratio and pulse profile with a two component source spectrum (an absorbed power law and black body). Simulations run to reproduce the anticorrelation in the pulse profile and hardness ratio show that this behaviour can be explained if the two components are pulsating $\sim \pi$ out of phase. Despite the fact that both spectral components have similar pulsed fractions, the combined effect of the two pulsating components has very little effect on the overall spectrum at energies $\gtrsim 3$ keV, thus explaining the reduction in the pulsed fraction. The temperature and X-ray luminosity of the black body suggests an emitting radius of 0.5 ± 0.2 km. This, along with the apparent variation of the black body with rotation, suggests the emission originates from a polar cap. The simulated pulse profile of the black body was used to constrain the angles between the rotation axis and the magnetic axis, α and the angle between the rotation axis and line-of-sight ζ.

In Chapter 3 I decompose the apparently broad iron line of CI Cam into three intrinsically narrow lines, neutral Fe-Kα and Kβ and almost completely ionised

FeXXV Kα. It is unclear how both neutral and almost fully ionised iron can co-exist and could suggest multiple emitting regions. The iron abundance implied by the ratio of the neutral Kα and Kβ line fluxes is consistent with solar within errors. The light curve extracted in the energy range defined as the Fe-Kα line from the spectral fits (6.20-6.55 keV) shows marginal evidence for a lag when cross correlated with that of the continuum.

Chapter 4 describes the search for HMXBs in the Phoenix dwarf galaxy, a dwarf irregular galaxy with similarities to the SMC. None of the 81 X-ray sources detected in the *XMM-Newton* field of view have the X-ray and optical characteristics of an HMXB. More generally, Chapter 4 spotlights the difficulties of searching for HMXBs, in particular BeXRBs.The transient nature of these systems make single epoch searches ineffective, unless the limiting flux of the observation probes down to their quiescent level. The similarity of HMXB and AGN spectra makes it impossible to distinguish between the two in the low count rate regime. Similarly, simulations of simple sine waves indicate that detecting pulsations (conclusive evidence for the presence of a neutron stars) requires a greater count rate than that observed in the brightest source in Chapter 4. Multiple observations of limited depth which can identify short term X-ray variability are a much more effective way of detecting these sources (e.g. Galache *et al.* 2008).

Chapter 5 presents the work done searching for evidence of two different channels of neutron star formation. Thus far, no evidence has been found to support the hypothesis of two different channels of neutron star formation in the cluster-BeXRB separations or in the neutron star masses implied by the $log_{10}(-\dot{P}) - log_{10}(P_{spin}L^{\frac{3}{7}})$ relation. However, the results are preliminary, and many of the areas requiring improvement before this work is published are already highlighted within the Chapter.

6.0.1 Future Work

The source discussed in Chapter 2, Swift J045106.8-694803, is the latest member of an emerging subclass of BeXRB which are characterised by persistent low luminosity ($L_X < 10^{36}$ ergs s^{-1}), long pulse period ($P > 100$ s) with hot black body components ($kT_{BB} < 1$ keV). I would like to extend the work done in Chapter 2 to six other persistent BeXRBs listed in Table 2.1, at least one of which has shown similar behaviour to Swift J045106.8-694803 (an anticorrelation between the hardness ratio and pulse profile): RX J0146.9+6121 (La Palombara and Mereghetti, 2006). Most of these sources have much greater signal to noise and so could be used to test the simulation by performing pulsed phased spectroscopy in parallel and comparing

the results. If valid, the results of the simulation can then be used to constrain the geometry of all of these systems.

The high spin-up rate of Swift J045106.8-694803 suggests it is an accreting magnetar candidate along with other members of this class, 4U 2206+54 and SXP1062, suggesting a link between the magnetic field and the hot excess. However, at least one of these sources (X Per) does not demonstrate any magnetar characteristics. The magnetic fields of all the remaining sources have thus far been assumed to be B$\sim 10^{12}$ G. Using archival measurements of spin and luminosity and the formulae of Ghosh and Lamb (1979) and Shakura *et al.* (2012) the magnetic fields of the remaining sources could be determined and any link between the two parameters further explored.

Further observations of CI Cam (the topic of Chapter 3) of increased duration would allow the presence of the lag to be confirmed or, indeed, refuted. They could also allow me to explore the possibility of any lags between the ionised Fe-Kα line with both the continuum and the neutral Fe-Kα line. This in turn could provide further insight into the system, identifying where the different ionisation states of iron exist in relation to each other and the X-ray source. I would like to continue this work by searching for time delays in the iron line of the only other known sgB[e]-XRB, IGR J16318-4848. Interestingly this source shows no evidence for an ionised Fe-Kα line, indicating there is a clear difference between the two sources.

In Chapter 5 I identify several of the reasons that make the SMC ideal for doing population studies of HMXBs: its well constrained distance, the high density of source and small angular size. The *XMM-Newton* survey of the SMC (and ongoing survey of the LMC) provide a homogeneous sample of B[e] stars all at the same distance and observed down to a similar flux limit. It has been hypothesised that binary interactions could be somewhat responsible for the B[e] phenomenon (e.g. Zickgraf 2003; Kastner *et al.* 2010), however as yet only three B[e] binaries are known (Ci Cam and IGR J16318-4848, which appear to be bona fide HMXBs and Wd1-9, a colliding wind binary). Much controversy has surrounded the nature of the compact object in CI Cam (and to a lesser extent IGR J16318-4848) due to the uncertainty in the distances to these systems.

By identifying an extragalactic population of these sources, with well defined distances, I could get an idea of the range of X-ray luminosities these sources can have, which in turn can be used to better understand the Galactic population. Two sgB[e] stars have already been identified as X-ray sources in the preliminary data analysis. One in the SMC (S18) and one in the LMC (S134). An archival study of the optical behaviour of S18 has already shown it does not conform to the tradi-

tion picture of sgB[e] stars as essentially static objects. It is highly photometrically and spectroscopically variable with no obvious correlation between the two. Shore *et al.* (1987); Zickgraf *et al.* (1989) have already suggested that the highly variable behaviour of the HeII 4686Å line in particular is caused by binarity. Any X-ray emission in excess of that expected from such a star would add weight to this suggestion and could possibly identify the nature of the unseen companion. Further work is required to confirm that these are genuine counterparts to the sgB[e] stars and extract hardness ratios. These can be compared with those of CI Cam and IGR J16318-4848, Wd1-9 and simulated spectra of background AGN to confirm the nature of these X-ray sources. Along with any other sgB[e] stars yet to be identified in the survey and flux limits for any undetected sources, this will be the first study of sgB[e] stars as a population in X-rays.

APPENDICES

A

Complete X-ray Source List for the Phoenix Dwarf Galaxy

Table A.1: Properties of all the sources detected in the *XMM-Newton* observation of the Phoenix dwarf Galaxy. Count rates and fluxes are both given for the 0.2–12 keV energy range. The $\log(\frac{f_X}{f_{opt}})$ is calculated from the 0.2–4.5 keV flux values and the optical data available in the LGGS or USNO catalogues. The classification column follows the designation in the text with *classified* sources in square brackets. Unclassified sources are listed as "unclass". Sources marked with * were analysed in Section 4.5 with XSPEC and so the flux values come from the model fit to the spectrum.

ID	RA	Dec	$err_{1\sigma}$	Count rate	flux	$\log(\frac{f_X}{f_{opt}})$	HR1	HR2	HR3	HR4	Classification
	J2000	J2000	arcsec	10^{-3} s^{-1}	10^{-14} ergs cm^{-2} s^{-1}						
47	01:49:43.7	-44:26:46.4	2.1	10±1	2.4±0.8	-0.05	0.0±0.1	-0.1±0.1	0.1±0.2	-1.0±0.3	[hard]
23	01:49:54.1	-44:22:49.3	1.7	12±2	8±1		0.7±0.3	0.7±0.1	-0.2±0.1	0.6±0.1	[hard]
36	01:49:54.4	-44:25:04.0	1.7	11±1	8±1		0.4±0.2	0.1±0.1	-0.9±0.2	0.98±0.07	unclass
81	01:49:54.8	-44:32:27.9	1.6	24±2	12±2		-0.41±0.08	0.1±0.1	0.1±0.1	0.62±0.06	[hard]
91	01:50:02.1	-44:34:56.2	1.8	17±2	6±2		-0.78±0.09	0.5±0.1	0.0±0.1	0.53±0.07	[hard]
15	01:50:03.5	-44:21:23.5	1.7	5.9±0.8	0.6±0.3		0.2±0.1	0.1±0.1	-0.5±0.2	0.8±0.3	unclass
84	01:50:06.8	-44:33:20.0	1.8	11±1	1.0±0.9	-3.10	0.05±0.09	-0.6±0.1	0.1±0.3	0.3±0.3	[fgstar]
25	01:50:07.6	-44:22:54.4	1.6	24±1	3.9±0.7	-0.02	0.04±0.06	0.04±0.06	-0.32±0.08	0.1±0.1	[hard]
31	01:50:11.5	-44:23:23.2	1.5	30±1	5.3±0.7	0.18	0.11±0.05	-0.13±0.05	-0.43±0.07	0.1±0.1	[gal]
49	01:50:12.7	-44:26:58.6	1.5	33±1	11±1	-0.30	0.70±0.07	0.52±0.04	-0.32±0.04	-0.13±0.0	[hard]
33	01:50:14.9	-44:24:04.2	1.6	7.0±0.8	1.4±0.4		0.9±0.2	0.66±0.09	-0.1±0.1	-0.3±0.2	[hard]
70	01:50:15.0	-44:30:41.1	1.6	8±1	2.2±0.7		0.1±0.1	-0.1±0.2	-0.5±0.1	0.4±0.2	unclass
96	01:50:15.4	-44:35:51.4	1.5	67±2	19±2	1.13	0.23±0.04	0.15±0.04	-0.33±0.04	-0.07±0.08	[hard]
7	01:50:19.4	-44:39:56.0	1.5	58±2	13±2	-0.44	-0.17±0.04	-0.20±0.05	-0.43±0.07	-0.4±0.3	unclass
71	01:50:19.7	-44:30:47.7	1.6	19±1	3.4±0.5	0.87	0.04±0.08	0.18±0.07	-0.20±0.07	-0.4±0.1	[hard]
3	01:50:20.5	-44:17:10.6	1.7	11±1	6±1		0.1±0.2	0.4±0.1	-0.3±0.1	0.5±0.1	[hard]
42	01:50:20.7	-44:25:55.5	1.7	6.9±0.8	3.0±0.7	0.08	0.2±0.1	0.0±0.1	-0.5±0.2	0.7±0.1	unclass
4	01:50:23.8	-44:17:08.7	1.6	17±2	2.2±0.6	0.15	0.1±0.1	0.0±0.1	-0.3±0.1	0.4±0.1	[hard]
14	01:50:24.2	-44:20:49.1	1.6	6.8±0.7	0.9±0.4	-4.55	0.32±0.08	-0.61±0.09	-1.0±0.4	1.0±1.9	fgstar
39	01:50:28.1	-44:25:35.2	1.7	11.6±0.7	1.5±0.3	-0.90	0.79±0.05	-0.36±0.06	-0.5±0.1	-0.8±0.3	gal
11	01:50:28.7	-44:19:27.7	1.7	8.6±0.8	5.8±0.9		0.3±0.3	0.7±0.1	-0.3±0.1	0.3±0.1	[hard]
41	01:50:29.0	-44:25:51.7	1.6	15.3±0.8	3.0±0.4		0.40±0.06	-0.05±0.06	-0.65±0.07	0.2±0.1	[gal]
82	01:50:32.9	-44:32:32.2	1.6	9.4±0.8	1.4±0.4	0.27	0.2±0.1	0.10±0.09	-0.3±0.1	-0.6±0.3	[hard]
90	01:50:38.5	-44:34:45.5	1.5	60±2	9.2±0.8	0.27	-0.03±0.03	-0.14±0.04	-0.42±0.05	-0.3±0.1	unclass
1	01:50:39.2	-44:40:25.5	1.9	9±2	5±2		-0.2±0.2	0.3±0.2	0.0±0.2	-0.1±0.4	[hard]
35*	01:50:41.0	-44:24:32.9	1.5	18.0±0.8	1.9	-0.38	0.11±0.06	0.02±0.06	-0.17±0.06	-0.30±0.09	[AGN]
56	01:50:42.7	-44:29:04.5	1.5	22.4±0.8	2.5±0.2	-2.20	0.42±0.04	-0.38±0.04	-0.72±0.06	-0.1±0.2	fgstar
99	01:50:43.6	-44:36:13.1	1.6	12±1	2.6±0.8	-4.46	0.2±0.1	0.19±0.09	-0.5±0.1	0.1±0.2	fgstar
68	01:50:45.2	-44:30:34.7	1.6	15±1	6.3±0.7	-0.12	0.0±0.1	0.17±0.09	-0.3±0.1	0.46±0.09	[AGN]
54	01:50:45.3	-44:28:29.2	1.6	7.1±0.5	1.5±0.3	0.08	0.26±0.09	-0.16±0.09	-0.5±0.1	0.3±0.2	unclass
12	01:50:46.6	-44:20:31.6	1.7	4.4±0.5	2.0±0.5		0.4±0.2	0.0±0.1	-0.1±0.2	0.2±0.2	[hard]

ID	RA	Dec	$err_{1\sigma}$	Count rate	flux	$\log(\frac{f_X}{f_{opt}})$	HR1	HR2	HR3	HR4	Classification
	J2000	J2000	arcsec	10^{-3} s^{-1}	10^{-14} ergs cm^{-2} s^{-1}						
52*	01:50:47.2	-44:27:44.2	1.5	47±1	6.5	-0.14	0.09±0.03	0.00±0.03	-0.43±0.03	-0.34±0.06	[AGN]
61*	01:50:51.8	-44:29:38.4	1.5	20.2±0.8	3.8	0.42	0.07±0.05	0.13±0.04	-0.29±0.05	-0.7±0.1	[AGN]
100	01:50:54.5	-44:36:23.7	1.7	9.4±0.9	2.3±0.6	-0.31	-0.1±0.1	-0.1±0.1	-0.5±0.2	0.6±0.2	unclass
62	01:50:54.6	-44:29:44.7	1.7	3.4±0.4	0.9±0.3	-0.07	0.1±0.2	0.0±0.2	0.3±0.2	-0.1±0.2	[hard]
66	01:51:00.1	-44:30:19.6	1.7	13±1	1.4±0.3		0.4±0.1	0.2±0.1	-0.3±0.1	0.2±0.1	[hard]
34*	01:51:00.5	-44:24:29.7	1.6	7.3±0.5	1.2	-0.12	0.00±0.09	0.09±0.08	-0.4±0.1	0.2±0.2	[AGN]
9	01:51:02.9	-44:18:52.4	1.5	21±1	9.4±0.8		0.77±0.09	0.42±0.06	-0.21±0.06	0.08±0.07	[hard]
16	01:51:03.2	-44:21:39.3	1.8	3.5±0.4	1.0±0.3		0.3±0.2	0.2±0.1	-0.2±0.1	0.0±0.2	[hard]
58	01:51:04.3	-44:29:23.7	1.6	9.9±0.6	1.5±0.2	0.07	0.05±0.06	-0.26±0.07	-0.2±0.1	-0.1±0.1	unclass
48	01:51:04.6	-44:26:49.2	1.7	2.8±0.3	0.4±0.2	-0.61	-0.2±0.1	-0.2±0.2	-0.4±0.2	0.0±0.4	unclass
10	01:51:09.0	-44:18:56.0	1.6	20.7±0.8	4.3±0.5	0.21	-0.13±0.04	-0.09±0.05	-0.49±0.07	0.1±0.2	[gal]
21	01:51:13.7	-44:22:46.2	1.7	8.7±0.9	1.1±0.3		0.9±0.1	0.3±0.1	-0.1±0.1	-0.1±0.1	[hard]
28	01:51:13.8	-44:23:07.8	1.6	19±1	3.2±0.4	0.47	0.22±0.08	0.05±0.08	-0.16±0.08	-0.2±0.1	[hard]
38	01:51:14.9	-44:25:09.9	1.6	9.8±0.5	1.5±0.2		0.39±0.07	0.14±0.06	-0.32±0.07	-0.7±0.	[hard]
2	01:51:17.6	-44:40:14.9	1.6	9±1	2.3±0.8		0.1±0.1	-0.4±0.1	0.2±0.2	0.5±0.3	unclass
22	01:51:21.6	-44:22:43.2	1.6	16±1	1.3±0.2		0.04±0.09	0.24±0.08	-0.48±0.08	0.27±0.08	unclass
55	01:51:22.5	-44:28:39.6	1.6	7.3±0.5	1.1±0.2		0.14±0.09	0.19±0.08	-0.35±0.09	-0.7±0.2	[hard]
13	01:51:23.3	-44:20:44.0	1.6	7.1±0.6	1.7±0.3		0.9±0.1	0.39±0.07	-0.43±0.08	-0.1±0.2	[hard]
92	01:51:24.7	-44:35:09.2	1.6	21±1	10.0±0.9	-0.82	1.0±0.6	0.86±0.07	0.38±0.05	-0.27±0.0	[hard]
50	01:51:24.9	-44:27:23.9	1.6	6.8±0.6	1.6±0.3		0.2±0.1	0.0±0.1	-0.2±0.1	0.0±0.2	[hard]
72	01:51:25.9	-44:31:07.4	1.7	10±1	2.4±0.5		-0.1±0.2	-0.2±0.2	0.2±0.2	0.6±0.1	unclass
29	01:51:26.0	-44:23:11.9	1.7	4.8±0.5	1.0±0.2		0.4 ±0.1	0.1±0.1	-0.5±0.1	-0.1±0.2	unclass
20	01:51:28.6	-44:22:39.1	1.9	2.9±0.4	0.3±0.1	-0.84	1.0 ±0.2	0.1±0.1	-0.2±0.1	-0.6±0.3	[hard]
73	01:51:30.1	-44:30:54.3	1.5	23.2±0.9	5.2±0.5	0.12	0.25±0.05	0.01±0.05	-0.39±0.06	-0.1±0.1	[hard]
65	01:51:30.2	-44:29:57.0	1.6	17±2	3.0±0.5		0.4±0.1	0.19±0.09	-0.1±0.1	-0.1±0.1	[hard]
27	01:51:30.6	-44:22:54.9	1.6	9.0±0.5	1.2±0.2	-1.41	0.41±0.06	-0.48±0.06	-0.9±0.1	0.8±0.2	fgstar
74	01:51:32.1	-44:31:11.3	1.7	5.4±0.6	1.6±0.4		0.5 ±0.2	0.1±0.1	-0.9±0.1	0.9±0.1	unclass
59	01:51:37.3	-44:29:27.3	1.6	7.6±0.6	1.4±0.3		0.36±0.09	0.09±0.08	-0.4±0.1	-0.1±0.2	[hard]
63	01:51:39.7	-44:29:46.8	1.6	9.9±0.7	3.3±0.5		0.34±0.09	0.00±0.08	-0.3±0.1	0.1±0.1	[hard]
8	01:51:41.3	-44:18:27.3	1.5	35±1	7.0±0.7	-0.02	0.06±0.04	0.00±0.04	-0.25±0.05	-0.40±0.09	[hard]
6	01:51:41.4	-44:18:13.3	1.7	6.5±0.9	2.6±0.6		0.1±0.2	0.3±0.2	-0.5±0.2	0.7±0.1	unclass
67	01:51:41.8	-44:30:13.6	1.7	7.2±0.6	2.3±0.4		0.5±0.1	-0.2±0.1	0.0±0.1	0.1±0.1	unclass
85	01:51:42.0	-44:33:21.7	1.6	11.9±0.9	2.9±0.7		0.3±0.1	0.21±0.07	-0.51±0.09	0.0±0.2	unclass
45	01:51:42.7	-44:26:07.7	1.6	13.0±0.7	3.1±0.4		0.23±0.07	0.13±0.06	-0.25±0.07	-0.2±0.1	[hard]
17	01:51:43.3	-44:21:55.9	1.9	4.6±0.6	1.8±0.5		1.0±0.1	0.4±0.1	-0.1±0.1	0.2±0.2	[hard]
94	01:51:44.5	-44:35:31.1	1.7	11±1	6±1		0.6±0.1	0.2±0.1	-0.3±0.1	0.5±0.2	[hard]
18	01:51:45.6	-44:22:00.0	1.6	13.1±0.8	2.3±0.4	-0.58	-0.02±0.07	0.10±0.07	-0.28±0.08	-0.3±0.2	[hard]
101	01:51:49.9	-44:37:04.5	1.7	12±1	2.5±0.7	-0.48	-0.2±0.1	0.2±0.1	-0.1±0.1	0.0±0.2	[hard]
78	01:51:51.6	-44:32:17.5	1.8	4.1±0.6	0.6±0.4	-2.37	0.6±0.2	-0.2±0.2	-0.3±0.2	-0.4±0.4	fgstar

ID	RA	Dec	$err_{1\sigma}$	Count rate	flux	$\log(\frac{f_X}{f_{opt}})$	HR1	HR2	HR3	HR4	Classification
	J2000	J2000	arcsec	10^{-3} s^{-1}	10^{-14} ergs cm^{-2} s^{-1}						
43	01:51:52.1	-44:25:46.1	1.6	10.5±0.6	1.3±0.2		0.13±0.07	0.00±0.07	-0.32±0.09	-1.0±0.2	[AGN]
80	01:51:55.4	-44:32:22.5	1.6	15±1	4.0±0.7	0.24	0.79±0.08	0.21±0.08	-0.13±0.08	0.0±0.1	[hard]
60	01:51:56.0	-44:29:28.7	1.6	10±1	3.1±0.7	-0.56	0.7±0.1	-0.2±0.1	-0.1±0.2	0.4±0.1	[gal]
83	01:51:57.2	-44:32:55.3	1.6	16±1	3.9±0.8		0.70±0.09	0.30±0.06	-0.20±0.07	-0.3±0.2	[hard]
30	01:51:57.4	-44:23:06.1	1.6	18±1	5.7±0.7	-0.20	0.09±0.08	0.11±0.07	-0.25±0.08	0.2±0.1	[hard]
57	01:52:00.7	-44:29:14.6	1.6	8.5±0.8	4.0±0.7		1.0±0.2	0.5±0.1	0.23±0.09	-0.1±0.1	[hard]
97	01:52:00.9	-44:35:54.5	1.6	25±1	5.0±0.9		0.37±0.07	-0.10±0.06	-0.08±0.07	-0.2±0.1	[hard]
19	01:52:02.6	-44:22:08.7	1.6	12.1±0.9	3.0±0.6		0.5±0.1	0.30±0.08	-0.08±0.08	-0.2±0.1	[hard]
26	01:52:11.1	-44:22:56.2	1.7	5.0±0.6	5±1		1.0±1.9	0.96±0.07	0.2±0.1	-0.5±0.2	[hard]
5	01:52:11.3	-44:18:08.8	1.6	27±3	31±6		0.6±0.1	0.4±0.1	-0.3±0.1	0.3±0.2	[hard]
37	01:52:25.0	-44:25:16.5	1.7	9.1±0.9	11±2		0.2±0.2	0.5±0.1	-0.2±0.1	0.3±0.1	[hard]

BIBLIOGRAPHY

Anders E., Grevesse N., 1989, Geochimica et Cosmochimica Acta, 53, 197

Antoniou V., Zezas A., Hatzidimitriou D., Kalogera V., 2010, Astrophys. J. Lett., 716, L140

Arnaud K. A., 1996, in Jacoby G. H., Barnes J. (eds.), *Astronomical Data Analysis Software and Systems V*, vol. 101 of *Astronomical Society of the Pacific Conference Series*, p. 17

Arzoumanian Z., Chernoff D. F., Cordes J. M., 2002, Astrophys. J., 568, 289

Ashman K. M., Bird C. M., Zepf S. E., 1994, Astron. J., 108, 2348

Balan A., Tycner C., Zavala R. T., Benson J. A., Hutter D. J., Templeton M., 2010, Astron. J., 139, 2269

Bambynek W., Crasemann B., Fink R. W., Freund H.-U., Mark H., Swift C. D., Price R. E., Rao P. V., 1972, Reviews of Modern Physics, 44, 716

Barragán L., Wilms J., Pottschmidt K., Nowak M. A., Kreykenbohm I., Walter R., Tomsick J. A., 2009, Astron. Astrophys., 508, 1275

Barsukova E. A., Borisov N. V., Burenkov A. N., Klochkova V. G., Goranskij V. P., Metlova N. V., 2006, in Kraus M., Miroshnichenko A. S. (eds.), *Stars with the B[e] Phenomenon*, vol. 355 of *Astronomical Society of the Pacific Conference Series*, p. 305

Basko M. M., Sunyaev R. A., 1975, Astron. Astrophys., 42, 311

Basko M. M., Sunyaev R. A., 1976, Sov. Astron., 20, 537

Beardmore A. P., Coe M. J., Markwardt C., Osborne J. P., Baumgartner W. H., Tueller J., Gehrels N., 2009, The Astronomer's Telegram, 1901, 1

Belczynski K., Ziolkowski J., 2009, Astrophys. J., 707, 870

Belloni T., Dieters S., van den Ancker M. E., Fender R. P., Fox D. W., Harmon B. A., van der Klis M., Kommers J. M., Lewin W. H. G., van Paradijs J., 1999, Astrophys. J., 527, 345

Beloborodov A. M., 2002, Astrophys. J. Lett., 566, L85

Bica E., Dutra C. M., 2000, Astron. J., 119, 1214

Bildsten L., Chakrabarty D., Chiu J., Finger M. H., Koh D. T., Nelson R. W., Prince T. A., Rubin B. C., Scott D. M., Stollberg M., Vaughan B. A., Wilson C. A., Wilson R. B., 1997, Astrophys. J. Suppl. Ser., 113, 367

Bird A. J., Coe M. J., McBride V. A., Udalski A., 2012, Mon. Not. R. Astron. Soc., 423, 3663

Blaauw A., 1964, Ann. Rev. Astron. Astrophys., 2, 213

Blandford R. D., McKee C. F., 1982, Astrophys. J., 255, 419

Bodaghee A., Tomsick J. A., Rodriguez J., James J. B., 2012, Astrophys. J., 744, 108

Boirin L., Parmar A. N., Oosterbroek T., Lumb D., Orlandini M., Schartel N., 2002, Astron. Astrophys., 394, 205

Bonanos A. Z., Castro N., Macri L. M., Kudritzki R.-P., 2011, Astrophys. J. Lett., 729, L9

Bondi H., 1952, Mon. Not. R. Astron. Soc., 112, 195

Bondi H., Hoyle F., 1944, Mon. Not. R. Astron. Soc., 104, 273

Canterna R., Flower P. J., 1977, Astrophys. J. Lett., 212, L57

Chaty S., Rahoui F., 2012, Astrophys. J., 751, 150

Cheng K. S., Dai Z. G., 1997, Astrophys. J. Lett., 476, L39

Clark J. S., Miroshnichenko A. S., Larionov V. M., Lyuty V. M., Hynes R. I., Pooley G. G., Coe M. J., McCollough M., Dieters S., Efimov Y. S., Fabregat J., Goranskii V. P., Haswell C. A., Metlova N. V., Robinson E. L., Roche P., Shenavrin V. I., Welsh W. F., 2000, Astron. Astrophys., 356, 50

Clark J. S., Muno M. P., Negueruela I., Dougherty S. M., Crowther P. A., Goodwin S. P., de Grijs R., 2008, Astron. Astrophys., 477, 147

Clark J. S., Steele I. A., Fender R. P., Coe M. J., 1999, Astron. Astrophys., 348, 888

Coburn W., Heindl W. A., Gruber D. E., Rothschild R. E., Staubert R., Wilms J., Kreykenbohm I., 2001, Astrophys. J., 552, 738

Coe M. J., Corbet R. H. D., McGowan K. E., McBride V. A., Schurch M. P. E., Townsend L. J., Galache J. L., Negueruela I., Buckley D., 2009, in Van Loon J. T., Oliveira J. M. (eds.), *IAU Symposium*, vol. 256 of *IAU Symposium*, pp. 367–372

Coe M. J., Edge W. R. T., Galache J. L., McBride V. A., 2005, Mon. Not. R. Astron. Soc., 356, 502

Coe M. J., McBride V. A., Corbet R. H. D., 2010, Mon. Not. R. Astron. Soc., 401, 252

Collins II G. W., 1987, in Slettebak A., Snow T. P. (eds.), *IAU Colloq. 92: Physics of Be Stars*, pp. 3–19

Corbet R., 1985, Space Sci. Rev, 40, 409

Corbet R. H. D., 1984, Astron. Astrophys., 141, 91

Corbet R. H. D., 1986, Mon. Not. R. Astron. Soc., 220, 1047

Corbet R. H. D., Coe M. J., Galache J., Laycock S., Markwardt C. B., Marshall F. E., 2006, in Meurs E. J. A., Fabbiano G. (eds.), *Populations of High Energy Sources in Galaxies*, vol. 230 of *IAU Symposium*, pp. 170–174

Courvoisier T. J.-L., Walter R., Rodriguez J., Bouchet L., Lutovinov A. A., 2003,

IAU Circ., 8063, 3
Cox A. N., 2000, *Allen's astrophysical quantities*
de Jager C., Nieuwenhuijzen H., 1987, Astron. Astrophys., 177, 217
Diaz J., Bekki K., 2011, Mon. Not. R. Astron. Soc., 413, 2015
Dickey J. M., Lockman F. J., 1990, Ann. Rev. Astron. Astrophys., 28, 215
Dieball A., Long K. S., Knigge C., Thomson G. S., Zurek D. R., 2010, Astrophys. J., 710, 332
Dray L. M., 2006, Mon. Not. R. Astron. Soc., 370, 2079
Edgar R., 2004, New Astronomy Reviews, 48, 843
Evans C. J., Howarth I. D., Irwin M. J., Burnley A. W., Harries T. J., 2004, Mon. Not. R. Astron. Soc., 353, 601
Evans C. J., Lennon D. J., Smartt S. J., Trundle C., 2006, Astron. Astrophys., 456, 623
Filliatre P., Chaty S., 2004, Astrophys. J., 616, 469
Frank J., King A., Raine D. J., 2002, *Accretion Power in Astrophysics: Third Edition*
Frontera F., Orlandini M., Amati L., dal Fiume D., Masetti N., Orr A., Parmar A. N., Brocato E., Raimondo G., Piersimoni A., Tavani M., Remillard R. A., 1998, Astron. Astrophys., 339, L69
Fürst F., Suchy S., Kreykenbohm I., Barragán L., Wilms J., Pottschmidt K., Caballero I., Kretschmar P., Ferrigno C., Rothschild R. E., 2011, Astron. Astrophys., 535, A9
Galache J. L., Corbet R. H. D., Coe M. J., Laycock S., Schurch M. P. E., Markwardt C., Marshall F. E., Lochner J., 2008, Astrophys. J. Suppl. Ser., 177, 189
Gallart C., Martínez-Delgado D., Gómez-Flechoso M. A., Mateo M., 2001, Astron. J., 121, 2572
Gardiner L. T., Noguchi M., 1996, Mon. Not. R. Astron. Soc., 278, 191
Ghosh P., Lamb F. K., 1979, Astrophys. J., 234, 296
Gilfanov M., 2004, Mon. Not. R. Astron. Soc., 349, 146
Gilli R., Comastri A., Hasinger G., 2007, Astron. Astrophys., 463, 79
Glatt K., Grebel E. K., Koch A., 2010, Astron. Astrophys., 517, A50
Grimm H.-J., Gilfanov M., Sunyaev R., 2003, Mon. Not. R. Astron. Soc., 339, 793
Güver T., Özel F., 2009, Mon. Not. R. Astron. Soc., 400, 2050
Haberl F., Eger P., Pietsch W., 2008a, Astron. Astrophys., 489, 327
Haberl F., Eger P., Pietsch W., Corbet R. H. D., Sasaki M., 2008b, Astron. Astrophys., 485, 177
Haberl F., Sturm R., Ballet J., Bomans D. J., Buckley D. A. H., Coe M. J., Corbet R., Ehle M., Filipovic M. D., Gilfanov M., Hatzidimitriou D., La Palombara N.,

Mereghetti S., Pietsch W., Snowden S., Tiengo A., 2012a, Astron. Astrophys., 545, A128

Haberl F., Sturm R., Filipović M. D., Pietsch W., Crawford E. J., 2012b, Astron. Astrophys., 537, L1

Harris J., Zaritsky D., 2004, Astron. J., 127, 1531

Harris J., Zaritsky D., 2009, Astron. J., 138, 1243

Heindl W. A., Coburn W., Gruber D. E., Pelling M. R., Rothschild R. E., Wilms J., Pottschmidt K., Staubert R., 1999, Astrophys. J. Lett., 521, L49

Hénault-Brunet V., Oskinova L. M., Guerrero M. A., Sun W., Chu Y.-H., Evans C. J., Gallagher III J. S., Gruendl R. A., Reyes-Iturbide J., 2012, Mon. Not. R. Astron. Soc., 420, L13

Hickox R. C., Narayan R., Kallman T. R., 2004, Astrophys. J., 614, 881

Hidalgo S. L., Aparicio A., Martínez-Delgado D., Gallart C., 2009, Astrophys. J., 705, 704

Hilditch R. W., Howarth I. D., Harries T. J., 2005, Mon. Not. R. Astron. Soc., 357, 304

Hjellming R. M., Mioduszewski A. J., Ueda Y., Ishida M., Inoue H., Dotani T., Lewin W. H. G., Greiner J., 1998, IAU Circ., 6872, 1

Ho W. C. G., 2007, Mon. Not. R. Astron. Soc., 380, 71

Holtzman J. A., Smith G. H., Grillmair C., 2000, Astron. J., 120, 3060

Hong J., Schlegel E. M., Grindlay J. E., 2004, Astrophys. J., 614, 508

Horne J. H., Baliunas S. L., 1986, Astrophys. J., 302, 757

Hornschemeier A. E., Brandt W. N., Garmire G. P., Schneider D. P., Barger A. J., Broos P. S., Cowie L. L., Townsley L. K., Bautz M. W., Burrows D. N., Chartas G., Feigelson E. D., Griffiths R. E., Lumb D., Nousek J. A., Ramsey L. W., Sargent W. L. W., 2001, Astrophys. J., 554, 742

Hynes R. I., Clark J. S., Barsukova E. A., Callanan P. J., Charles P. A., Collier Cameron A., Fabrika S. N., Garcia M. R., Haswell C. A., Horne K., Miroshnichenko A., Negueruela I., Reig P., Welsh W. F., Witherick D. K., 2002, Astron. Astrophys., 392, 991

Illarionov A. F., Sunyaev R. A., 1975, Astron. Astrophys., 39, 185

Inam S. Ç., Baykal A., Beklen E., 2010, Mon. Not. R. Astron. Soc., 403, 378

Irwin M., Tolstoy E., 2002, Mon. Not. R. Astron. Soc., 336, 643

Irwin M. J., Demers S., Kunkel W. E., 1990, Astron. J., 99, 191

Ishida M., Morio K., Ueda Y., 2004, Astrophys. J., 601, 1088

Kaastra J. S., Mewe R., 1993, Astron. Astrophys. Suppl. Ser, 97, 443

Kahabka P., Haberl F., Payne J. L., Filipović M. D., 2006, Astron. Astrophys., 458,

285

Kahabka P., Hilker M., 2005, Astron. Astrophys., 435, 9

Kastner J. H., Buchanan C., Sahai R., Forrest W. J., Sargent B. A., 2010, Astron. J., 139, 1993

Kato S., 1983, Publ. Astron. Soc. Jpn., 35, 249

Klus H., Bartlett E. S., Bird A. J., Coe M., Corbet R. H. D., Udalski A., 2013, Mon. Not. R. Astron. Soc., 428, 3607

Knigge C., Coe M. J., Podsiadlowski P., 2011, Nature, 479, 372

Kong A. K. H., McClintock J. E., Garcia M. R., Murray S. S., Barret D., 2002, Astrophys. J., 570, 277

La Palombara N., Mereghetti S., 2006, Astron. Astrophys., 455, 283

La Palombara N., Mereghetti S., 2007, Astron. Astrophys., 474, 137

La Palombara N., Sidoli L., Esposito P., Tiengo A., Mereghetti S., 2009, Astron. Astrophys., 505, 947

La Palombara N., Sidoli L., Esposito P., Tiengo A., Mereghetti S., 2012, Astron. Astrophys., 539, A82

Lamers H. J. G. L. M., Waters L. B. F. M., 1987, Astron. Astrophys., 182, 80

Laycock S., Zezas A., Hong J., Drake J. J., Antoniou V., 2010, Astrophys. J., 716, 1217

Leahy D. A., 1987, Astron. Astrophys., 180, 275

Lennon D. J., 1997, Astron. Astrophys., 317, 871

Lewin W. H. G., van der Klis M., 2006, *Compact Stellar X-ray Sources*

Lewin W. H. G., van Paradijs J., van den Heuvel E. P. J., 1997, *X-ray Binaries*

Li K. L., Kong A. K. H., Charles P. A., Lu T.-N., Bartlett E. S., Coe M. J., McBride V., Rajoelimanana A., Udalski A., Masetti N., Franzen T., 2012, Astrophys. J., 761, 99

Liu Q. Z., van Paradijs J., van den Heuvel E. P. J., 2005, Astron. Astrophys., 442, 1135

Liu Q. Z., van Paradijs J., van den Heuvel E. P. J., 2006, Astron. Astrophys., 455, 1165

Lucy L. B., Solomon P. M., 1970, Astrophys. J., 159, 879

Lutovinov A., Revnivtsev M., Gilfanov M., Shtykovskiy P., Molkov S., Sunyaev R., 2005, Astron. Astrophys., 444, 821

Lutovinov A., Tsygankov S., 2008, in Axelsson M. (ed.), *American Institute of Physics Conference Series*, vol. 1054 of *American Institute of Physics Conference Series*, pp. 191–202

Maccacaro T., Gioia I. M., Wolter A., Zamorani G., Stocke J. T., 1988, Astrophys.

J., 326, 680
Maccarone T. J., 2003, Astron. Astrophys., 409, 697
Maeder A., Grebel E. K., Mermilliod J.-C., 1999, Astron. Astrophys., 346, 459
Maggi P., Haberl F., Sturm R., Pietsch W., Rau A., Greiner J., Udalski A., Sasaki M., 2013, ArXiv e-prints
Maraschi L., Treves A., van den Heuvel E. P. J., 1976, Nature, 259, 292
Martínez-Delgado D., Gallart C., Aparicio A., 1999, Astron. J., 118, 862
Mason A. B., Clark J. S., Norton A. J., Crowther P. A., Tauris T. M., Langer N., Negueruela I., Roche P., 2012, Mon. Not. R. Astron. Soc., 422, 199
Massey P., 2002, Astrophys. J. Suppl. Ser., 141, 81
Massey P., Olsen K. A. G., Hodge P. W., Jacoby G. H., McNeill R. T., Smith R. C., Strong S. B., 2007, Astron. J., 133, 2393
Mateo M. L., 1998, Ann. Rev. Astron. Astrophys., 36, 435
Mathewson D. S., Cleary M. N., Murray J. D., 1974, Astrophys. J., 190, 291
Matt G., Guainazzi M., 2003, Mon. Not. R. Astron. Soc., 341, L13
McBride V. A., Bird A. J., Coe M. J., Townsend L. J., Corbet R. H. D., Haberl F., 2010, Mon. Not. R. Astron. Soc., 403, 709
McBride V. A., Coe M. J., Negueruela I., Schurch M. P. E., McGowan K. E., 2008, Mon. Not. R. Astron. Soc., 388, 1198
McGowan K. E., Coe M. J., Schurch M. P. E., McBride V. A., Galache J. L., Edge W. R. T., Corbet R. H. D., Laycock S., Buckley D. A. H., 2008, Mon. Not. R. Astron. Soc., 383, 330
McLaughlin D. B., 1961, Astrophys. J., 134, 1015
McSwain M. V., Gies D. R., 2005, Astrophys. J. Suppl. Ser., 161, 118
Menzies J., Feast M., Whitelock P., Olivier E., Matsunaga N., da Costa G., 2008, Mon. Not. R. Astron. Soc., 385, 1045
Mioduszewski A. J., Rupen M. P., 2004, Astrophys. J., 615, 432
Miroshnichenko A. S., Klochkova V. G., Bjorkman K. S., Panchuk V. E., 2002, Astron. Astrophys., 390, 627
Monet D. G., Levine S. E., Canzian B., Ables H. D., Bird A. R., Dahn C. C., Guetter H. H., Harris H. C., Henden A. A., Leggett S. K., Levison H. F., Luginbuhl C. B., Martini J., Monet A. K. B., Munn J. A., Pier J. R., Rhodes A. R., Riepe B., Sell S., Stone R. C., Vrba F. J., Walker R. L., Westerhout G., Brucato R. J., Reid I. N., Schoening W., Hartley M., Read M. A., Tritton S. B., 2003, Astron. J., 125, 984
Moon D.-S., Kaplan D. L., Reach W. T., Harrison F. A., Lee J.-E., Martin P. G., 2007, Astrophys. J. Lett., 671, L53
Morgan W. W., Keenan P. C., Kellman E., 1943, *An atlas of stellar spectra, with an*

outline of spectral classification
Murakami H., Dotani T., Wijnands R., 2003, IAU Circ., 8070, 3
Negueruela I., 1998, Astron. Astrophys., 338, 505
Negueruela I., Okazaki A. T., 2001, Astron. Astrophys., 369, 108
Nomoto K., 1984, Astrophys. J., 277, 791
North P., Zahn J.-P., 2003, Astron. Astrophys., 405, 677
Nowak M. A., 1995, Publ. Astron. Soc. Pac., 107, 1207
Okazaki A. T., 1991, Publ. Astron. Soc. Jpn., 43, 75
Okazaki A. T., 1996, Publ. Astron. Soc. Jpn., 48, 305
Okazaki A. T., Negueruela I., 2001, Astron. Astrophys., 377, 161
Papaloizou J. C., Savonije G. J., Henrichs H. F., 1992, Astron. Astrophys., 265, L45
Parmar A. N., Belloni T., Orlandini M., Dal Fiume D., Orr A., Masetti N., 2000, Astron. Astrophys., 360, L31
Parmar A. N., White N. E., Stella L., 1989, Astrophys. J., 338, 373
Paturel G., Dubois P., Petit C., Woelfel F., 2002, LEDA, 0 (2002), p. 0
Pechenick K. R., Ftaclas C., Cohen J. M., 1983, Astrophys. J., 274, 846
Peterson B. M., 1993, Publ. Astron. Soc. Pac., 105, 247
Peterson B. M., Wanders I., Horne K., Collier S., Alexander T., Kaspi S., Maoz D., 1998, Publ. Astron. Soc. Pac., 110, 660
Pfahl E., Rappaport S., Podsiadlowski P., Spruit H., 2002, Astrophys. J., 574, 364
Pickles A. J., 1998, Publ. Astron. Soc. Pac., 110, 863
Pietsch W., Misanovic Z., Haberl F., Hatzidimitriou D., Ehle M., Trinchieri G., 2004, Astron. Astrophys., 426, 11
Popov S. B., Turolla R., 2012, Mon. Not. R. Astron. Soc., 421, L127
Porquet D., Reeves J. N., Uttley P., Turner T. J., 2004, Astron. Astrophys., 427, 101
Portegies Zwart S. F., 1995, Astron. Astrophys., 296, 691
Porter J. M., Rivinius T., 2003, Publ. Astron. Soc. Pac., 115, 1153
Protassov R., van Dyk D. A., Connors A., Kashyap V. L., Siemiginowska A., 2002, Astrophys. J., 571, 545
Putman M. E., Gibson B. K., Staveley-Smith L., Banks G., Barnes D. G., Bhatal R., Disney M. J., Ekers R. D., Freeman K. C., Haynes R. F., Henning P., Jerjen H., Kilborn V., Koribalski B., Knezek P., Malin D. F., Mould J. R., Oosterloo T., Price R. M., Ryder S. D., Sadler E. M., Stewart I., Stootman F., Vaile R. A., Webster R. L., Wright A. E., 1998, Nature, 394, 752
Raguzova N. V., 2001, Astron. Astrophys., 367, 848
Rajoelimanana A. F., Charles P. A., Udalski A., 2011, Mon. Not. R. Astron. Soc., 413, 1600

Rappaport S., Ma C. P., Joss P. C., Nelson L. A., 1987, Astrophys. J., 322, 842
Reig P., 2011, ApSS, 332, 1
Reig P., Fabregat J., Coe M. J., 1997, Astron. Astrophys., 322, 193
Reig P., Negueruela I., Coe M. J., Fabregat J., Tarasov A. E., Zamanov R. K., 2000, Mon. Not. R. Astron. Soc., 317, 205
Reig P., Torrejón J. M., Blay P., 2012, Mon. Not. R. Astron. Soc., 425, 595
Reynolds C. S., Nowak M. A., 2003, Phys. Rep., 377, 389
Rieke G. H., Lebofsky M. J., 1985, Astrophys. J., 288, 618
Robinson E. L., Ivans I. I., Welsh W. F., 2002, Astrophys. J., 565, 1169
Russell S. C., Dopita M. A., 1992, Astrophys. J., 384, 508
Sana H., de Mink S. E., de Koter A., Langer N., Evans C. J., Gieles M., Gosset E., Izzard R. G., Le Bouquin J.-B., Schneider F. R. N., 2012, Science, 337, 444
Sasaki M., Klochkov D., Kraus U., Caballero I., Santangelo A., 2010, Astron. Astrophys., 517, A8
Schönherr G., Wilms J., Kretschmar P., Kreykenbohm I., Santangelo A., Rothschild R. E., Coburn W., Staubert R., 2007, Astron. Astrophys., 472, 353
Schuster H.-E., West R. M., 1976, Astron. Astrophys., 49, 129
Shakura N., Postnov K., Kochetkova A., Hjalmarsdotter L., 2012, Mon. Not. R. Astron. Soc., 420, 216
Shore S. N., Sanduleak N., Allen D. A., 1987, Astron. Astrophys., 176, 59
Shtykovskiy P., Gilfanov M., 2005, Mon. Not. R. Astron. Soc., 362, 879
Skinner S. L., Simmons A. E., Zhekov S. A., Teodoro M., Damineli A., Palla F., 2006, Astrophys. J. Lett., 639, L35
Slettebak A., 1982, Astrophys. J. Suppl. Ser., 50, 55
Smith D., Remillard R., Swank J., Takeshima T., Smith E., 1998, IAU Circ., 6855, 1
Stanimirovic S., Staveley-Smith L., Dickey J. M., Sault R. J., Snowden S. L., 1999, Mon. Not. R. Astron. Soc., 302, 417
Stella L., White N. E., Rosner R., 1986, Astrophys. J., 308, 669
Strüder L., Briel U., Dennerl K., Hartmann R., Kendziorra E., Meidinger N., Pfeffermann E., Reppin C., Aschenbach B., Bornemann W., Bräuninger H., Burkert W., Elender M., Freyberg M., Haberl F., Hartner G., Heuschmann F., Hippmann H., Kastelic E., Kemmer S., Kettenring G., Kink W., Krause N., Müller S., Oppitz A., Pietsch W., Popp M., Predehl P., Read A., Stephan K. H., Stötter D., Trümper J., Holl P., Kemmer J., Soltau H., Stötter R., Weber U., Weichert U., von Zanthier C., Carathanassis D., Lutz G., Richter R. H., Solc P., Böttcher H., Kuster M., Staubert R., Abbey A., Holland A., Turner M., Balasini M., Bignami G. F., La

Palombara N., Villa G., Buttler W., Gianini F., Lainé R., Lumb D., Dhez P., 2001, Astron. Astrophys., 365, L18

Sturm R., Haberl F., Pietsch W., Coe M. J., Mereghetti S., La Palombara N., Owen R. A., Udalski A., 2012a, Astron. Astrophys., 537, A76

Sturm R., Haberl F., Rau A., Bartlett E. S., Zhang X.-L., Schady P., Pietsch W., Greiner J., Coe M. J., Udalski A., 2012b, Astron. Astrophys., 542, A109

Thureau N. D., Monnier J. D., Traub W. A., Millan-Gabet R., Pedretti E., Berger J.-P., Garcia M. R., Schloerb F. P., Tannirkulam A.-K., 2009, Mon. Not. R. Astron. Soc., 398, 1309

Timmer J., Koenig M., 1995, Astron. Astrophys., 300, 707

Torrejón J. M., Schulz N. S., Nowak M. A., Kallman T. R., 2010, Astrophys. J., 715, 947

Townsend L. J., 2012, *An X-Ray, Optical and Infra-red study of High-Mass X-Ray Binaries in the Small Magellanic Cloud*, Ph.D. thesis, School of Physics and Astronomy, University of Southampton, UK

Townsend L. J., Coe M. J., Corbet R. H. D., McBride V. A., Hill A. B., Bird A. J., Schurch M. P. E., Haberl F., Sturm R., Pathak D., van Soelen B., Bartlett E. S., Drave S. P., Udalski A., 2011, Mon. Not. R. Astron. Soc., 410, 1813

Townsend R. H. D., Owocki S. P., Howarth I. D., 2004, Mon. Not. R. Astron. Soc., 350, 189

Treister E., Urry C. M., 2006, Astrophys. J. Lett., 652, L79

Trümper J., Pietsch W., Reppin C., Voges W., Staubert R., Kendziorra E., 1978, Astrophys. J. Lett., 219, L105

Turner M. J. L., Abbey A., Arnaud M., Balasini M., Barbera M., Belsole E., Bennie P. J., Bernard J. P., Bignami G. F., Boer M., Briel U., Butler I., Cara C., Chabaud C., Cole R., Collura A., Conte M., Cros A., Denby M., Dhez P., Di Coco G., Dowson J., Ferrando P., Ghizzardi S., Gianotti F., Goodall C. V., Gretton L., Griffiths R. G., Hainaut O., Hochedez J. F., Holland A. D., Jourdain E., Kendziorra E., Lagostina A., Laine R., La Palombara N., Lortholary M., Lumb D., Marty P., Molendi S., Pigot C., Poindron E., Pounds K. A., Reeves J. N., Reppin C., Rothenflug R., Salvetat P., Sauvageot J. L., Schmitt D., Sembay S., Short A. D. T., Spragg J., Stephen J., Strüder L., Tiengo A., Trifoglio M., Trümper J., Vercellone S., Vigroux L., Villa G., Ward M. J., Whitehead S., Zonca E., 2001, Astron. Astrophys., 365, L27

Tycner C., Lester J. B., Hajian A. R., Armstrong J. T., Benson J. A., Gilbreath G. C., Hutter D. J., Pauls T. A., White N. M., 2005, Astrophys. J., 624, 359

Uttley P., Edelson R., McHardy I. M., Peterson B. M., Markowitz A., 2003, Astro-

phys. J. Lett., 584, L53

van de Rydt F., Demers S., Kunkel W. E., 1991, Astron. J., 102, 130

van Loon J. T., Smith K. T., McDonald I., Sarre P. J., Fossey S. J., Sharp R. G., 2009, Mon. Not. R. Astron. Soc., 399, 195

van Wassenhove S., Volonteri M., Walker M. G., Gair J. R., 2010, Mon. Not. R. Astron. Soc., 408, 1139

Vaughan S., Edelson R., Warwick R. S., Uttley P., 2003, Mon. Not. R. Astron. Soc., 345, 1271

Walborn N. R., Fitzpatrick E. L., 1990, Publ. Astron. Soc. Pac., 102, 379

Walborn N. R., Parker J. W., Nichols J. S., 1995, NASA Reference Publication, 1363

Watson M. G., Schröder A. C., Fyfe D., Page C. G., Lamer G., Mateos S., Pye J., Sakano M., Rosen S., Ballet J., Barcons X., Barret D., Boller T., Brunner H., Brusa M., Caccianiga A., Carrera F. J., Ceballos M., Della Ceca R., Denby M., Denkinson G., Dupuy S., Farrell S., Fraschetti F., Freyberg M. J., Guillout P., Hambaryan V., Maccacaro T., Mathiesen B., McMahon R., Michel L., Motch C., Osborne J. P., Page M., Pakull M. W., Pietsch W., Saxton R., Schwope A., Severgnini P., Simpson M., Sironi G., Stewart G., Stewart I. M., Stobbart A.-M., Tedds J., Warwick R., Webb N., West R., Worrall D., Yuan W., 2009, Astron. Astrophys., 493, 339

Wegner W., 2006, Mon. Not. R. Astron. Soc., 371, 185

Wilms J., Allen A., McCray R., 2000, Astrophys. J., 542, 914

Yokogawa J., Imanishi K., Tsujimoto M., Nishiuchi M., Koyama K., Nagase F., Corbet R. H. D., 2000, Astrophys. J. Suppl. Ser., 128, 491

Young L. M., Lo K. Y., 1997, Astrophys. J., 490, 710

Young L. M., Skillman E. D., Weisz D. R., Dolphin A. E., 2007, Astrophys. J., 659, 331

Zacharias N., Monet D. G., Levine S. E., Urban S. E., Gaume R., Wycoff G. L., 2004, in *American Astronomical Society Meeting Abstracts*, vol. 36 of *Bulletin of the American Astronomical Society*, p. 1418

Zamanov R. K., Reig P., Martí J., Coe M. J., Fabregat J., Tomov N. A., Valchev T., 2001, 367, 884

Zaritsky D., Harris J., Thompson I. B., Grebel E. K., 2004, Astron. J., 128, 1606

Zhang Y. H., 2002, Mon. Not. R. Astron. Soc., 337, 609

Zickgraf F.-J., 2003, Astron. Astrophys., 408, 257

Zickgraf F.-J., 2006, in Kraus M., Miroshnichenko A. S. (eds.), *Stars with the B[e] Phenomenon*, vol. 355 of *Astronomical Society of the Pacific Conference Series*,

p. 135

Zickgraf F.-J., Wolf B., Leitherer C., Appenzeller I., Stahl O., 1986, Astron. Astrophys., 163, 119

Zickgraf F.-J., Wolf B., Stahl O., Humphreys R. M., 1989, Astron. Astrophys., 220, 206

Zickgraf F.-J., Wolf B., Stahl O., Leitherer C., Klare G., 1985, Astron. Astrophys., 143, 421

Zorec J., Briot D., 1997, Astron. Astrophys., 318, 443